Computers in Biology and Medicine 151 (2022) 106214

Contents lists available at ScienceDirect

Computers in Biology and Medicine

journal homepage: www.elsevier.com/locate/compbiomed

A novel minimum generalized cross entropy-based multilevel segmentation technique for the brain MRI/dermoscopic images

Bibekananda Jena [a], Manoj Kumar Naik [b,**], Rutuparna Panda [c,*], Ajith Abraham [d]

[a] Dept. of Electronics and Communication Engineering, Anil Neerukonda Institute of Technology & Science, Sangivalasa, Visakhapatnam, Andhra Pradesh, 531162, India
[b] Faculty of Engineering and Technology, Siksha O Anusandhan, Bhubaneswar, Odisha, 751030, India
[c] Dept of Electronics and Telecommunication Engineering, Veer Surendra Sai University of Technology, Burla, Odisha, 768018, India
[d] Machine Intelligence Research Labs, Scientific Network for Innovation and Research Excellence, WA, 98071-2259, USA

ARTICLE INFO

Keywords:
Biomedical engineering
Machine learning
Multilevel thresholding
Generalized cross-entropy
Optimization algorithm

ABSTRACT

Background: One of the challenging and the primary stages of medical image examination is the identification of the source of any disease, which may be the aberrant damage or change in tissue or organ caused by infections, injury, and a variety of other factors. Any such condition related to skin or brain sometimes advances in cancer and becomes a life-threatening disease. So, an efficient automatic image segmentation approach is required at the initial stage of medical image analysis.
Purpose: To make a segmentation process efficient and reliable, it is essential to use an appropriate objective function and an efficient optimization algorithm to produce optimal results.
Method: The above problem is resolved in this paper by introducing a new minimum generalized cross entropy (MGCE) as an objective function, with the inclusion of the degree of divergence. Another key contribution is the development of a new optimizer called opposition African vulture optimization algorithm (OAVOA). The proposed optimizer boosted the exploration, skill by inheriting the opposition-based learning.
The results: The experimental work in this study starts with a performance evaluation of the optimizer over a set of standards (23 numbers) and IEEE CEC14 (8 numbers) Benchmark functions. The comparative analysis of test results shows that the OAVOA outperforms different state-of-the-art optimizers. The suggested OAVOA-MGCE based multilevel thresholding approach is carried out on two different types of medical images – Brain MRI Images (AANLIB dataset), and dermoscopic images (ISIC 2016 dataset) and found superior than other entropy-based thresholding methods.

1. Introduction

In the field of medical science, computers are being used extensively to perform different tasks [1–10]. Image segmentation is a fascinating and challenging problem in computer vision, especially in the medical imaging applications. In general, the majority of the region of the biomedical image is devoid of useful information. In this case, segmentation techniques are useful to separate an image region into non-overlapping parts. Radiologists use medical image segmentation to visualize and study the anatomy of human body structures [11], mimic biological processes [12], localize diseases [13], follow illness development, and determine the necessity for radiotherapy or surgery. As a result, automated and computerized methods for analyzing biomedical images are becoming more popular. These methods have the ability to accurately process large numbers of image samples in an allotted time. Further, automated systems can help to eliminate some of the inherent inaccuracies that come with manual inquiries. However, noisy, poor correlation, unclear regions, weak edges, overlapping, and a variety of other difficulties plague medical images and significantly alter the final segmentation outcomes.

During diagnosis, hard tissue evaluations are conducted using computer tomography and magnetic resonance imaging. In this paper, the proposed thresholding method is applied to brain magnetic resonance imagining (MRI) images and skin images. Brain MRI images are used by

* Corresponding author.
** Corresponding author.
E-mail addresses: bibekananda.jena@gmail.com (B. Jena), naik.manoj.kumar@gmail.com (M.K. Naik), r_ppanda@yahoo.co.in (R. Panda), ajith.abraham@ieee.org (A. Abraham).

https://doi.org/10.1016/j.compbiomed.2022.106214
Received 3 August 2022; Received in revised form 20 September 2022; Accepted 15 October 2022
Available online 21 October 2022

Table 1
Abbreviation/Symbols with their description.

Abbreviations/ Symbols	Description	Abbreviations/ Symbols	Description
MRI	Magnetic resonance imaging	CEC	Congress on evolutionary computation
ISIC	International Skin Imaging Collaboration	ANN	Artificial Neural Network
OF	Objective function	KNN	K-nearest neighbours
AVOA	African vulture optimization algorithm	ANOVA	Analysis of variance
OAVOA	Opposition African vulture optimization algorithm	PSNR	Peak signal-to-noise ratio
MCE	Minimum cross entropy	SSIM	Structural similarity index measure
MGCE	Minimum generalized cross entropy	FSIM	Feature Similarity Index measure
EO	Equilibrium Optimizer	PSO-IW	Particle swarm optimization with linearly varying inertia weight
HHO	Harris Hawk Optimization	HKSVM	Hybrid kernel-based support vector machine
TLBO	Teaching learning-based optimization	$M \times N$	Size of the input image
GSA	Gravitational search algorithm	L	No. of graylevel
DE	Differential algorithm	k	No. of thresholds
ABC	Artificial bee colony algorithm	R_j	j^{th} segmented region
WOA	Whale Optimization Algorithm	v	Pixel intensity
KH	Krill herd optimization	th_k	k^{th} threshold
PSO	Particle swarm optimization	h_i	Normalized histogram
OBL	Opposition-based learning	P_i	Region probability (i^{th} region)
MBO	Monarch butterfly optimization	α	Reniys Entropy order
SMA	Slime mould algorithm	r	Masi entropy parameter
HGS	Hunger Games Search	q	Tsallis parameter
MSA	Moth search algorithm	ξ and η	Random variables
RUN	Runge Kutta optimizer	φ and ψ	Probability distribution
CPA	Colony predation algorithm	p	degree of divergence index.
INFO	weIghted meaN oF vectOrs	G	Population matrix of the optimization algorithm
HSMA-WOA	Hybrid novel Slime mould algorithm with whale optimization algorithm	ub and lb	Upper and lower bound of the search space
IGWO	Improved grey wolf optimizer	N	No. of population
BLPSO	Biogeography-based learning particle swarm optimization	dim	Dimension of the problem
ESA	hybrid Emperor penguin and Salp swarm Algorithm	L_1 and L_2	Random numbers in the range $[0, 1]$
IGOA	Improved grasshopper optimization algorithm	V^t	Best Vulture at t^{th} iteration
CLSGMFO	Chaotic local search and Gaussian mutation-enhanced Moth-flame optimization	pr_i^t	Probability of selection among best two vultures
IMEHO	Improved elephant herding optimization	F^t	Hunger degree
EHO	elephant herding optimization	T	Maximum no. of iteration
HGWOP	Hybrid particle Swarm and grey wolf optimizer	r_1 to r_8	Random numbers generated uniformly in the interval [0, 1].
FFA	Firefly algorithm	p_1	likelihood of selection of updating mechanism in exploration phase
SVM	Support vector machine	p_2 and p_3	likelihood of selection of updating mechanism in exploitation phase
OCE-NGC	Optimal Estimation of clustering using a neutrosophic graph-cut	G_j^{opp}	Opposite solution of Gj
TAVOA	Time-varying mechanism based African vulture optimization algorithm	ω	a factor that impacts how much the exploration and exploitation stages are disrupted

the physician to diagnose different types of brain related diseases like Cerebrovascular Diseaseh Neoplastic Disease, Degenerative Disease, Inflammatory, Infectious Disease [13], etc. Dermoscopic is currently the most prevalent imaging tool used to assist dermatologists to extract meaningful information. It enables the detection of the region of diseased skin [14] that can't be seen with the naked eye. The most challenging job in skin image segmentation is to identify the desired region in the presence of some unpredictable factors like skin hair, unclear edges, and borders, lines on the skin surface, ruler marks, etc.

Thresholding is a prominent method of image segmentation. It divides an image into constituent parts, depending on specific threshold values. To segment an image using intensity as a criterion, global thresholding techniques are commonly employed. Some of the popular and widely used thresholding-based image segmentation methods are – Kapur's [15], Reniy's [16], Tsallis [17], Otsu's inter-class variance [18], Masi [19], cross-entropy [20], Kaniadakis [21], Shannon [21], and other entropy-based objective functions, which needs to be maximized or minimized for obtaining optimal threshold values. Among the different entropy-based methods, the minimum cross-entropy based method is founded popular. However, the maximum entropy and minimum cross entropy yield the same results while the prior distribution is uniform [22]. This happens due to the reason that, in some instances, the higher values of the entropy correspond to the lower values of the cross entropy. This may not also be efficient, when the prior distribution is not uniform. Further, the minimum cross entropy ignores the degree of divergence between the original and segmented images. This leads to a lower segmentation accuracy. This has motivated the authors to introduce a new minimum generalized cross entropy (MGCE) objective function. It warrants us to include the degree of divergence. Nevertheless, multilevel image thresholding requires a thorough search for the ideal threshold values as well as higher computation costs due to the growing number of thresholds. By structuring this as an optimization

Table 2
Objective function (OF) used for different entropy-based thresholding.

OF	Expression	Reference
Minimum Cross entropy (MCE)	$OF_{MCE}=\sum_{i=1}^{k+1} S^i$ where $S^i = \sum_{i=th_{i-1}}^{th_i} \left(i.h_i.log\left(i/\mu_i\right)\right)$ and $\mu_i = \sum_{i=th_{i-1}}^{th_i} i.h_i \Big/ \sum_{i=th_{i-1}}^{th_i} h_i$	[20]
Kaniadakis entropy	$OF_{Kaniadakis} = S_\kappa^{R_1} K^{R_1'} + S_\kappa^{R_2} K^{R_2'} + \ldots S_\kappa^{R_{k+1}} K^{R_{k+1}'}$ where $S_\kappa^{R_k} = -\frac{1}{2\kappa}\left\{\sum_{i=th_{k-1}}^{th_k-1}\left(\left(\frac{H_i}{\eta_{R_k}}\right)^{1+\kappa} - \left(\frac{H_i}{\eta_{R_k}}\right)^{1-\kappa}\right)\right\}$ $K^{R_k'} = \frac{1}{2}\left\{\sum_{i=0}^{(th_{k-1})-1}\left(\left(\frac{H_i}{\eta_{R_k'}}\right)^{1+\kappa} + \left(\frac{H_i}{\eta_{R_k'}}\right)^{1-\kappa}\right)\right\} + \frac{1}{2}\left\{\sum_{i=k}^{255}\left(\left(\frac{H_i}{\eta_{R_k'}}\right)^{1+\kappa} + \left(\frac{H_i}{\eta_{R_k'}}\right)^{1-\kappa}\right)\right\}$ where, $\eta_{R_k'} = \sum_{i=0}^{(th_{k-1})-1} H_i + \sum_{l=th_k}^{255} {}^{i}_{H}$ and $H_i = \left(\frac{Pr_{(i)}}{P_i}\right)$	[21]
Masi Entropy	$OF_{Masi} = \sum_{i=1}^{k+1} S_r(R_i)$ where $S_r(R_i) = \frac{1}{r-1}(\log(1 - (1-r)\sum_{i=th_{i-1}}^{th_i}(H_i).ln(H_i)))$	[19]
Tsallis Entropy	$OF_{Tsallis} = \sum_{i=1}^{k+1} S_q^{R^i} + (1-q)\prod_{i=0}^{k+1} S_q^{R^i}$ where, $S_q^{R_i} = \frac{1-\sum_{i=th_{i-1}}^{th_k}(H_i)^q}{q-1}$ and q is the Tsallis parameter indicates degree of non-extensivity of the system	[17]
Reniys Entropy	$OF_{Reniys} = \sum_{i=1}^{k+1} Rn_\alpha^i$ where, $Rn_\alpha^i = \frac{1}{1-\alpha}\, ln \sum_{i=th_{i-1}}^{th_i}(H_i)^\alpha$	[16]
Kapurs Entropy	$OF_{Kapur} = -\sum_{i=1}^{k+1} H_i \ln H_i$	[15]
Shannon Entropy	$OF_{Shannon} = -\sum_{i=1}^{k+1} Pr_{(i)}.ln(Pr_{(i)})$	[21]

problem, one can overcome the difficulties in choosing the best threshold values. Some of the Nature-inspired optimization algorithms which are successfully applied to multilevel thresholding in the past few years by are – Particle swarm optimization (PSO) [23], Differential algorithm (DE) [24], Teaching learning based optimization (TLBO) [25], Whale optimization algorithm (WOA) [26], Harris Hawk Optimization (HHO) [27], Equilibrium Optimizer (EO) [28].

In this study, we have examined a new recently developed African vulture optimization algorithm (AVOA) [29]. The AVOA is inspired by the navigation and foraging behaviour of African vultures. It offers a more extensive exploration and exploitation mechanism compared to other standard metaheuristic algorithms. Its adopted random strategy (during the search for optimal values) makes it efficient. It is also suitable to solve various real-world optimization based engineering problems [30,31]. The effective foraging technique of AVOA together with its capacity to resolve challenging technical issues drive us to thoroughly examine the algorithm. It encourages us to apply it to the image segmentation problem. Despite the fact that its design takes into account the balance of exploration and exploitation capabilities, it exhibits two flaws. Firstly, in the exploration stage, it only uses the best two solutions of the population selected using the Roulette Wheel selection method. This affects the exploration capability to some extent. Secondly, the tactic of using an exploitation mechanism early in the exploration (to boost the convergence rate) is also a constraint on exposing the maximum solution space. Taking above flaws into consideration, Fan et al. [32] introduced an improved tent chaotic mapping and time-varying mechanism based African vulture optimization algorithm (TAVOA). In this algorithm, a tent chaotic map is first created for population initialization. Secondly, the person's previous ideal position is noted and taken into account when updating their location. Thirdly, a time-varying method is created to balance the capacity for exploration and exploitation. Although TAVOA is a powerful optimizer, the chaotic map used may affect its performances. For a specific application that called for expertise or experimentation, the selective chaotic map is always necessary. To resolve the shortfall of AVOA, an opposition African vulture optimization algorithm (OAVOA) is proposed in this paper by integrating the opposition-based learning (OBL) [33] with the AVOA algorithm. The use of the OBL is an effort to boost the exploration skill by providing the required diversity and escaping strategy which ensures a better exploration mechanism. In order to make the paper more readable, the abbreviations and symbols used here are listed in Table 1.

In summary, the key contributions of the proposed work are:

i. A generalized cross-entropy (MGCE) based multilevel thresholding methodology is proposed for the first time by considering the degree of divergence during thresholding.
ii. By incorporating opposition-based learning into the current African vulture optimization algorithm (AVOA), an opposition African vulture optimization algorithm (OAVOA) is proposed. Before using it to solve the multilevel thresholding problem, OAVOA's performance is assessed using the standard benchmark functions. For a collection of 31 benchmark functions, including 23 classical test functions and 8 composite modern test functions from the CEC 2014 test suit, the OAVOA exhibits enhanced convergence with good optimizing performance as compared to the state-of-the-art methods.
iii. The MGCE based multilevel thresholding using OAVOA is validated by applying it to two different types of medical image datasets. The method provides superior segmented outputs when compared with other popular entropy-based methods.

The remainder of this work is as follows: A brief review of the related works is discussed in Section 2. An overview of the multilevel thresholding, entropy-based multilevel thresholding, generalized cross-entropy, African vulture optimization algorithm (AVOA), and opposition-based learning is presented in Section 3. Section 4 deals with the proposed methodology related to develop a new multilevel thresholding approach. Section 5 discussed experimental finding of the proposed method. At last, the paper ended with concluding comments in Section 6.

2. Related works

As the multilevel thresholding task is considered as an optimization problem, the thresholding accuracy is significantly influenced by the capability of the chosen optimization method to optimize a given entropy-based objective function. Therefore, the primary objective of any entropy-based multilevel thresholding process is selecting an appropriate algorithm for optimization. The literature has reported a number of recently developed nature-inspired algorithms and various segmentation methods for brain MRI and dermoscopic images.

In the past few years, a number of highly efficient Nature-inspired metaheuristic algorithms have been developed by many researchers. Artificial bee colony (ABC) [34]optimization which is based on how a colony of honey bees searches for food sources in the nature is a popular algorithm and applied to many optimization problems including multilevel thresholding. Due to improper trade-off between exploration

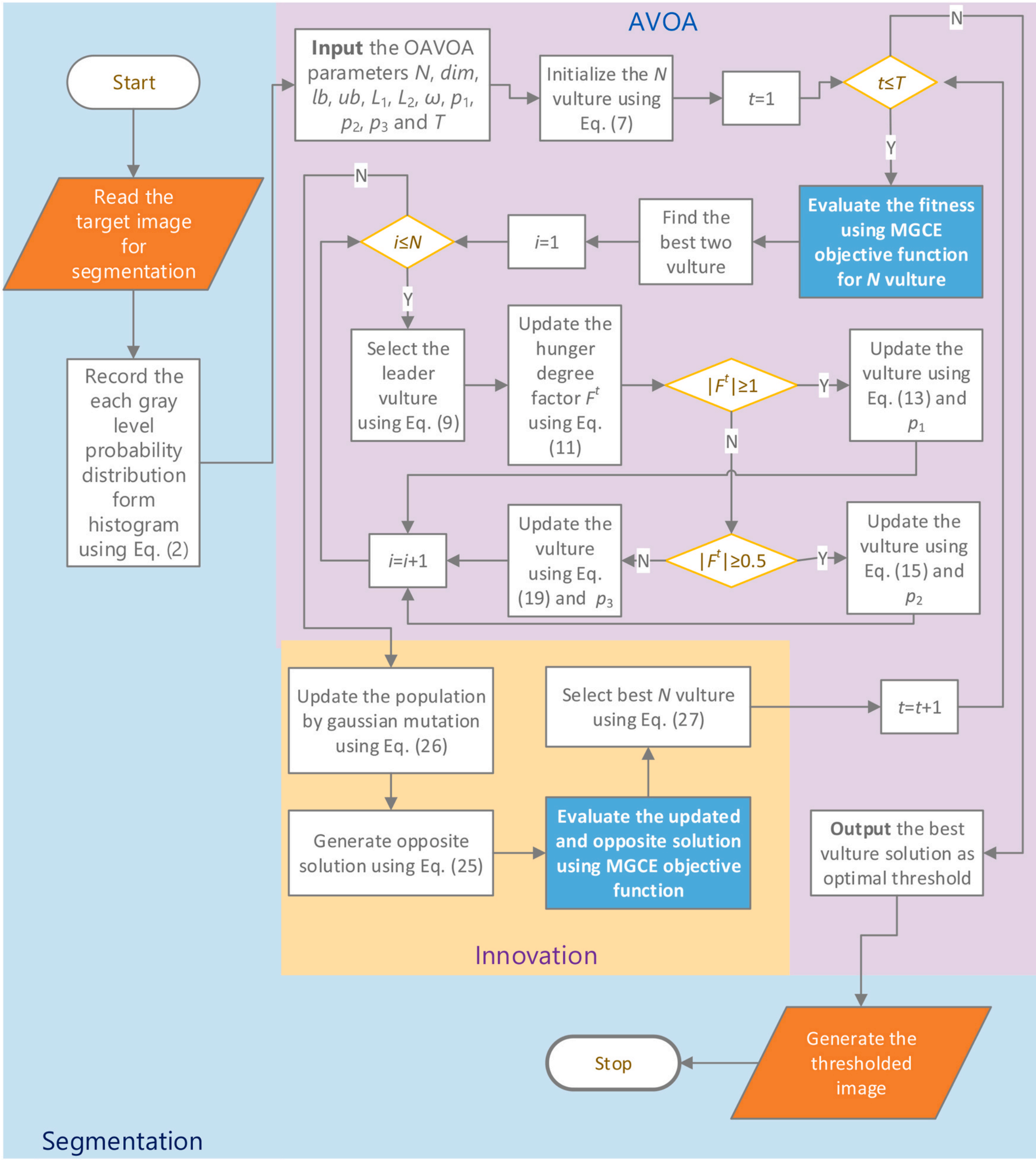

Fig. 1. Flow chart of the proposed OAVOA-MGCE based multilevel thresholding.

Table 3
Parameter settings.

Algorithm	Parameters
OAVOA	$L_1 = 0.8, L_2 = 0.2, w = 2.5, p_1 = 0.6, p_2 = 0.4, p_3 = 0.6$
AVOA	$L_1 = 0.8, L_2 = 0.2, w = 2.5, p_1 = 0.6, p_2 = 0.4, p_3 = 0.6$
EO	Constant $[a_1, a_2] = [2, 1]$ and Generation probability $(GP) = 0.5$
HHO	Scale factor $(\beta) = 1.5$
GSA	Alpha $= 20$, Rnorm $= 2$, Rpower $= 1$ and $G_0 = 100$
TLBO	Teaching factor $= [1, 2]$
DE	Crossover probability $= 0.5$ and Scaling factor $= 0.5$
TAVOA	$L_1 = 0.8, L_2 = 0.2, w = 2.5, p_1 = 0.6, p_2 = 0.4, p_3 = 0.6$
IGWO	
BLPSO	$c = 1, I = 1, E = 1$, and $\omega = 0.9–0.2$ (linearly decrease)
HGWOP	$a_{max} = 2$, $a_{min} = 0$, $Cr_{max} = 1$ and $Cr_{min} = 0$

and exploitation search behavior the convergence speed is affected by change of the population and sometimes trapped in local minima. Gandomi et al. [35] developed a Krill herd optimizer (KH) algorithm inspired by using a simulation of krill herding behaviour. Even though KH is a powerful algorithm for local search, it occasionally becomes stuck in some local optima and cannot effectively execute global search. One of the popular physics based algorithm is a Gravitational search algorithm (GSA) [36]. The algorithm uses the laws of motion and gravity of masses to describe how the agents interact. Because the fitness function depends on the masses of the agents, it has the drawback of being a sluggish process. As a result, the masses become heavier with each cycle, which limits their ability to move. Inspired from the elephants' herding behaviour, an algorithm Elephant herding optimization (EHO) [37] was also developed. Though the algorithm is well suited for some algorithm, but suffers from premature convergence, which degrade its performance.

To overcome problems in above mentioned standard algorithm, a number of advanced algorithms are introduced. One of them is

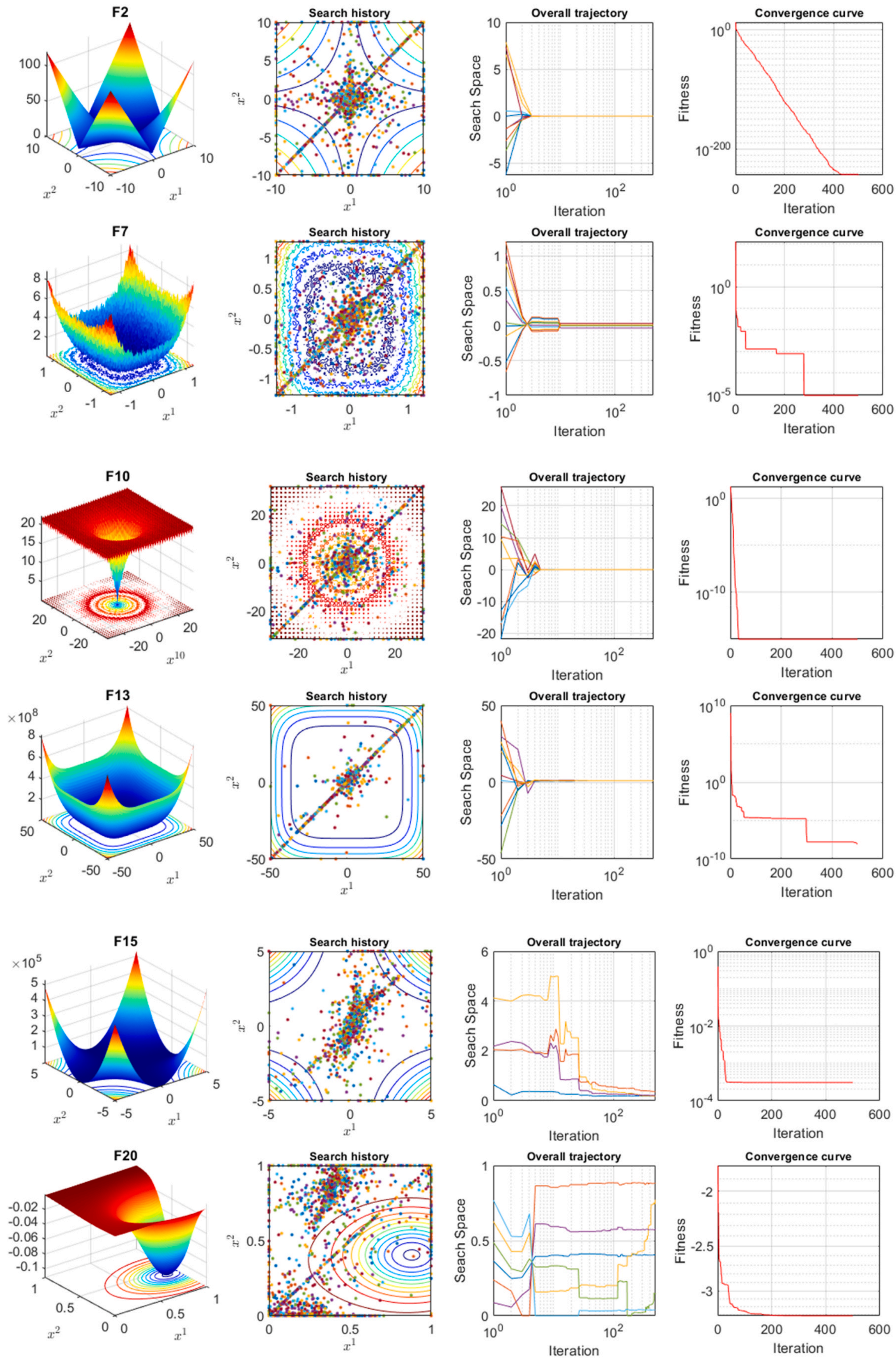

Fig. 2. Qualitative result of unimodal and multimodal test functions(F1, F7, F10, F13, F15 and F20).

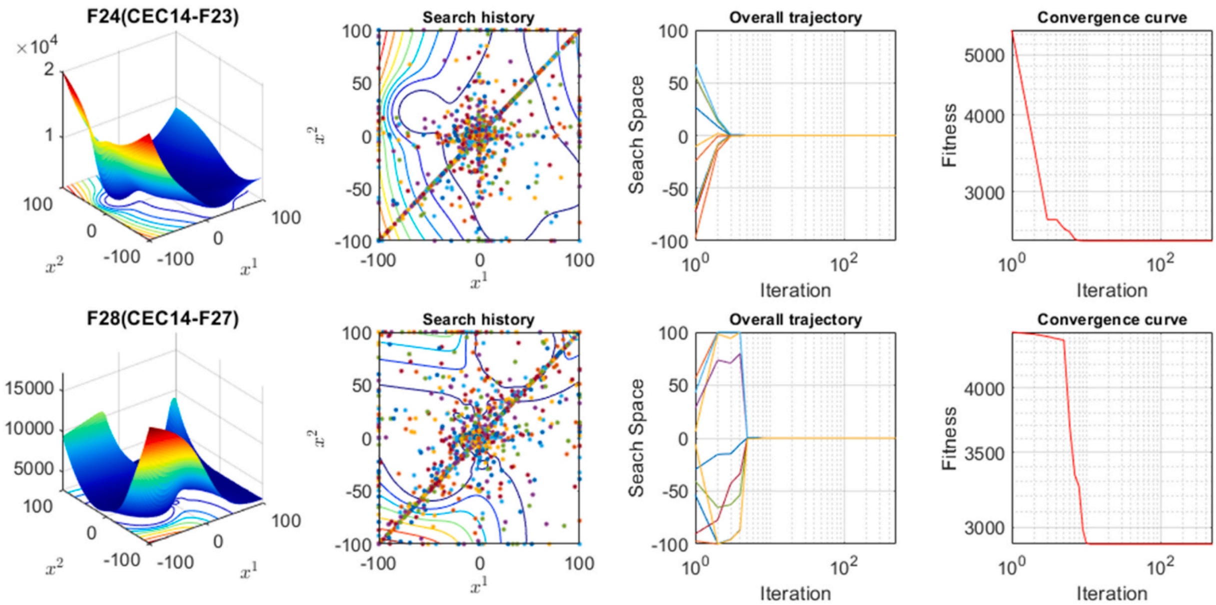

Fig. 3. Qualitative result of composite test functions F2 and F27 taken from CEC2014 testsuit.

Earthworm optimizer [38], which is inspired from the unique reproduction system of earthworm was also proposed by the researchers along with its different variants. In Monarch butterfly optimization (MBO) [39], the authors introduced a new optimization algorithm by mathematically modelling the migration behaviour of monarch butterflies. The algorithm compared with some of standard algorithms and found superior in optimizing both low as well as high dimensional problems. Another recently developed algorithm has been Slime mould algorithm (SMA) [40]. This optimization approach is motivated by the spreading and foraging behaviour of slime mould. With a number of novel features and a special mathematical model that simulates the production of positive and negative feedback of the slime mould propagation wave based on bio-oscillator, the SMA is able to find the best route to connect food source. Gai-Ge Wang et al. [41] developed a Moth search algorithm (MSA) where the two primary stages of the algorithm: exploitation (intensification) and exploration, were modelled using phototaxis and Levy flights from moths in nature. Based on how animals behave and what drives them when they are hungry, a new population-based optimization algorithm, Hunger Games Search (HGS) [42] is developed. To replicate the impact of hunger on each search step in this algorithm, an adaptive weight based on the idea of hunger is devised and used in the algorithm. The key advantages of this approach over existing optimization techniques are its dynamic nature, straightforward structure, excellent performance in terms of convergence, and acceptable quality of solutions.

Runge Kutta optimizer (RUN) [43] is a recently presented searching mechanism and used the concept of slope variations calculated using the Runge Kutta method of mathematics to reach optimal solution. Jiaze Tu et al. [44] presented the Colony predation algorithm (CPA), inspired from colony predation performed by animals to keep away from predators and improve their chances of success when hunting. The CPA method was evaluated against both traditional and CEC 2014 benchmark functions to demonstrate its superiority to other well-known algorithms. Based on weighted mean of vectors, Ahmadianfar et al. [45] designed a new Innovative optimizer named weighted mean of vectors (INFO). It is a modified weight mean approach that updates the positions of the vectors through three key procedures: an updating rule, vector combining, and a local search. Though the above algorithms have addressed the issues of a mechanism for boosting diversity with proper balance between exploration and exploitation process is still required. Additionally, it has been noted that some algorithms are modified or combined with other algorithms by researchers to enhance their utility than their initial forms.

Some of these algorithms which well-known and developed in last few years are Hybrid novel Slime mould algorithm with whale optimization algorithm (HSMA-WOA) [46], Improved grey wolf optimizer (IGWO) [47], Biogeography-based learning particle swarm optimization (BLPSO) [48], Hybrid emperor penguin and Salp swarm algorithm (ESA) [49], Improved grasshopper optimization algorithm (IGOA) [50], chaotic local search and Gaussian mutation-enhanced Moth-flame optimization (CLSGMFO) [51]. Integrating a learning-based intelligent strategy [52,53] with an evolution algorithm is one of the effective ways to improve its optimization behaviour. Gai-GeWang et al. recently developed an Improved elephant herding optimization (IMEHO) [54] that uses a novel learning mechanism and a global velocity approach to update the individuals' position and velocity in the elephant herding optimization (EHO) [37]. Inspired from the search mechanism of particle swarm optimization (PSO) and grey wolf optimizer (GWO), Zhang et al. [55] presented a Hybrid particle Swarm and grey wolf optimizer (HGWOP). The HGWOP is formed by combining a Simplified GWO with differential perturbation algorithm with mean example learning PSO. The algorithm was tested on a set of complex function taken from CEC 2013 and CEC 2015 test suit to prove its efficacy. Crisscross artificial bee colony algorithm (CCABC) [56] is another recently proposed algorithm which used horizontal and vertical search mechanism to improve the searching capability of ABC algorithm. The algorithm then employed to perform multilevel thresholding on COVID-19×-ray images by optimizing an objective function.

Segmentation methods differ greatly depending on the application, imaging modality, and other aspects. Brain tissue segmentation, for example, differs from skin cancer segmentation in terms of requirements. Noise, partial volume effects, and motion are all common image aberrations that can have a big impact on the segmentation algorithm's effectiveness. In addition, each imaging modality has its quirks to deal with. However, by taking into account existing information, approaches that are customized to specific applications can typically achieve superior performance. As a result, deciding on a suitable method for a segmentation challenge might be a tough decision. The challenges are more in the medical image segmentation. Therefore, the incorrect results can lead to ineffective therapies, which can raise mortality rates. Many segmentation techniques are developed and documented in the literature over the years to make the automatic

Table 4
Statistical results and comparison of OAVOA with another optimization algorithm such as AVOA, EO, HHO, TLBO, GSA, DE, TAVOA, IGWO, BLPSO and HGWOP on unimodal functions (G1).

Function		OAVOA	AVOA	EO	HHO	TLBO	GSA	DE	TAVOA	IGWO	BLPSO	HGWOP
F1	Average	**0**	9.046E-217	6.492E-41	3.329E-99	3.986E-89	3.048E-16	8.334E+00	**0**	2.395E-28	1.381E-04	2.062E-02
	Best	**0**	2.796E-306	2.059E-43	2.121E-116	5.490E-91	7.529E-17	1.439E-04	**0**	1.290E-30	2.147E-05	1.316E-03
	Median	**0**	4.085E-257	4.631E-42	2.032E-103	1.529E-89	2.844E-16	9.145E-02	**0**	5.257E-29	6.736E-05	1.105E-02
	Worst	**0**	2.804E-215	1.201E-39	5.502E-98	2.364E-88	9.716E-16	1.762E+02	**0**	3.698E-27	1.898E-03	9.088E-02
	Std. Dev.	**0**	0	2.276E-40	1.187E-98	5.931E-89	1.765E-16	3.229E+01	**0**	6.652E-28	3.299E-04	2.136E-02
F2	Average	1.161E-217	1.092E-133	4.976E-24	4.161E-50	3.651E-45	1.873E-01	1.274E-01	**4.281E-259**	7.704E-18	9.116E-04	3.783E-02
	Best	2.273E-244	1.476E-161	6.304E-25	5.275E-59	4.136E-46	5.087E-08	2.853E-04	**8.544E-301**	1.224E-18	4.750E-04	9.260E-03
	Median	7.112E-230	3.311E-146	3.005E-24	1.056E-53	2.508E-45	8.344E-08	6.273E-03	**2.927E-278**	6.161E-18	7.457E-04	3.361E-02
	Worst	3.598E-216	2.418E-132	2.627E-23	9.556E-49	1.973E-44	1.653E+00	1.588E+00	**1.324E-257**	2.147E-17	1.911E-03	1.278E-01
	Std. Dev.	**0**	4.416E-133	5.530E-24	1.748E-49	4.014E-45	4.602E-01	3.535E-01	**0**	5.063E-18	3.461E-04	2.464E-02
F3	Average	**0**	2.806E-175	8.275E-10	2.139E-64	2.046E-18	1.027E+03	6.309E+02	**0**	1.255E-03	2.784E+03	2.555E+02
	Best	**0**	1.034E-268	1.820E-14	1.652E-99	3.637E-20	3.931E+02	1.370E+02	**0**	2.564E-06	1.718E+03	6.504E+01
	Median	**0**	5.821E-216	2.401E-11	4.375E-86	6.832E-19	9.703E+02	5.865E+02	**0**	4.141E-04	2.758E+03	2.490E+02
	Worst	**0**	8.700E-174	1.200E-08	6.630E-63	1.523E-17	1.808E+03	1.884E+03	**0**	9.866E-03	3.978E+03	6.144E+02
	Std. Dev.	**0**	0	2.366E-09	1.191E-63	3.387E-18	3.233E+02	3.781E+02	**0**	1.967E-03	6.418E+02	1.163E+02
F4	Average	1.407E-196	9.536E-117	5.588E-10	1.855E-47	1.109E-36	7.293E+00	2.506E+01	**9.293E-250**	1.588E-05	5.266E+00	6.619E-01
	Best	1.445E-237	9.361E-148	1.160E-11	1.612E-57	2.378E-37	4.389E+00	1.435E+01	**1.702E-289**	3.198E-06	2.893E+00	2.763E-01
	Median	2.250E-218	9.590E-133	1.322E-10	2.465E-52	9.775E-37	7.262E+00	2.372E+01	**4.633E-268**	1.035E-05	5.297E+00	6.040E-01
	Worst	4.362E-195	2.956E-115	4.599E-09	5.730E-46	2.633E-36	1.065E+01	4.477E+01	**2.881E-248**	5.351E-05	9.499E+00	1.322E+00
	Std. Dev.	**0**	5.309E-116	9.499E-10	1.029E-46	6.575E-37	1.445E+00	7.619E+00	**0**	1.394E-05	1.531E+00	3.029E-01
F5	Average	**6.863E-04**	1.989E-03	2.547E+01	6.925E-03	2.518E+01	4.868E+01	3.222E+03	5.451E-03	2.421E+01	5.892E+01	5.351E+01
	Best	**4.597E-06**	3.917E-05	2.503E+01	1.260E-05	2.390E+01	2.530E+01	3.863E+01	3.560E-05	2.316E+01	2.291E+01	2.503E+01
	Median	**3.465E-04**	1.389E-03	2.546E+01	4.476E-03	2.520E+01	2.913E+01	5.419E+02	3.148E-03	2.422E+01	5.131E+01	3.017E+01
	Worst	**3.398E-03**	1.120E-02	2.603E+01	3.338E-02	2.647E+01	1.256E+02	4.305E+04	1.849E-02	2.505E+01	2.080E+02	2.579E+02
	Std. Dev.	**9.400E-04**	2.167E-03	2.420E-01	7.948E-03	5.375E-01	3.189E+01	8.384E+03	5.359E-03	4.052E-01	3.840E+01	5.155E+01
F6	Average	**1.460E-06**	7.716E-06	9.112E-06	9.605E-05	1.570E-05	4.079E-03	3.587E+00	5.778E-06	2.879E-02	1.239E-04	4.181E-02
	Best	1.171E-08	2.321E-07	1.324E-06	6.291E-08	2.211E-07	**8.700E-17**	1.952E-04	1.269E-07	2.605E-05	1.575E-05	4.343E-03
	Median	3.293E-07	5.162E-06	6.425E-06	4.822E-05	4.060E-06	**2.195E-16**	1.784E-01	4.695E-06	8.148E-05	9.997E-05	3.308E-02
	Worst	**1.216E-05**	2.688E-05	4.072E-05	6.683E-04	2.340E-04	1.265E-01	7.132E+01	2.800E-05	2.463E-01	4.195E-04	1.263E-01
	Std. Dev.	**2.806E-06**	6.386E-06	8.548E-06	1.471E-04	4.555E-05	2.271E-02	1.296E+01	5.639E-06	7.573E-02	8.931E-05	3.432E-02
F7	Average	**2.159E-04**	3.796E-04	1.249E-03	1.788E-04	1.031E-03	8.280E-02	6.278E-02	2.315E-04	2.630E-03	2.894E-02	8.730E-03
	Best	9.020E-06	**5.027E-06**	1.798E-04	3.248E-06	4.213E-04	2.865E-02	3.612E-02	1.181E-05	6.049E-04	1.389E-02	2.056E-03
	Median	**1.345E-04**	2.534E-04	1.195E-03	1.665E-04	1.074E-03	7.749E-02	5.969E-02	9.279E-05	2.503E-03	2.502E-02	7.701E-03
	Worst	1.611E-03	2.075E-03	2.792E-03	9.091E-04	1.708E-03	1.880E-01	1.098E-01	**4.251E-04**	6.147E-03	5.628E-02	2.073E-02
	Std. Dev.	2.994E-04	4.120E-04	6.643E-04	1.771E-04	3.257E-04	3.628E-02	1.851E-02	**2.103E-04**	1.200E-03	1.082E-02	3.981E-03

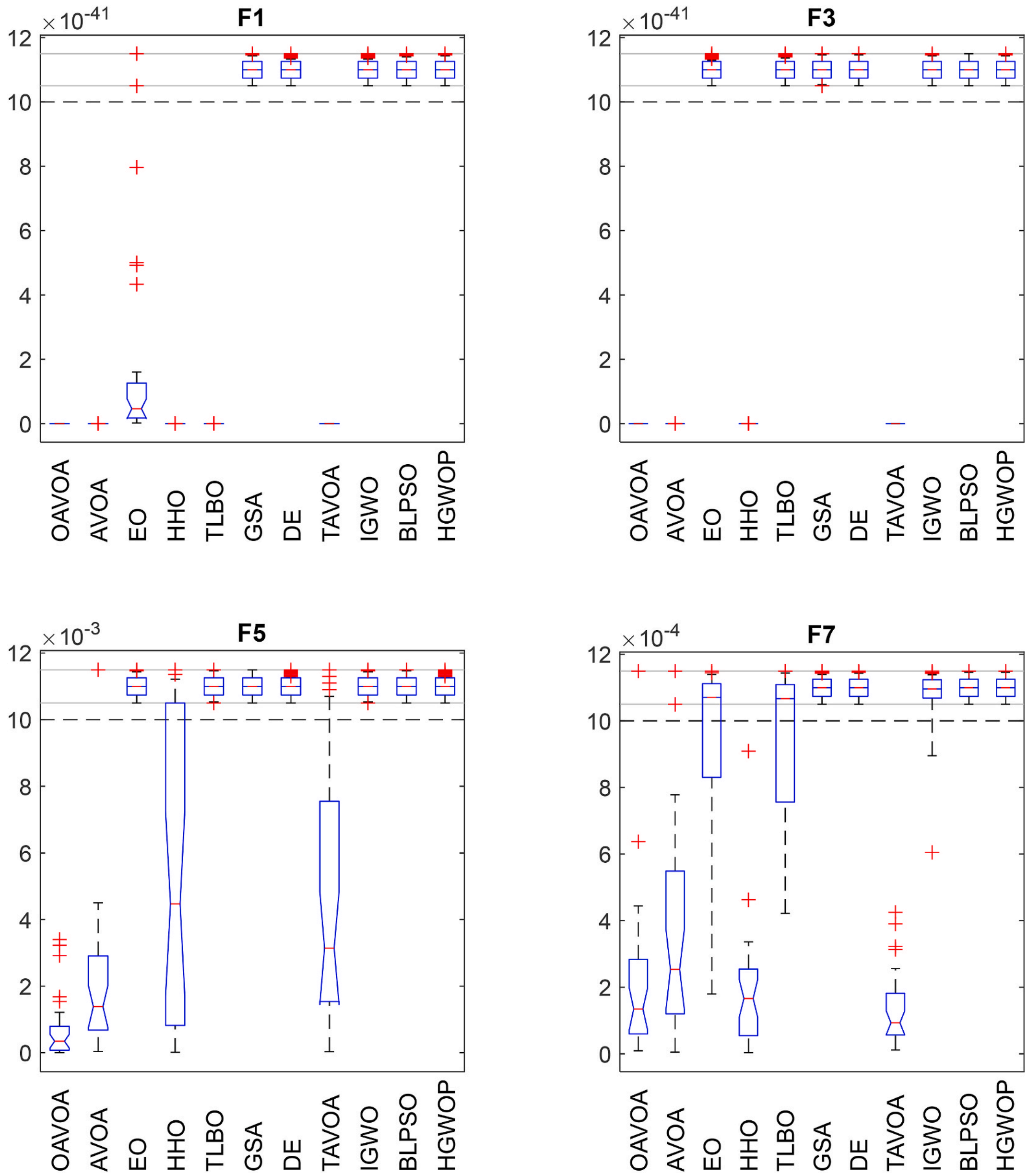

Fig. 4. Box plot of four unimodal functions.

detection of disease more operative and reliable. Most of the common approaches are based on soft computing and machine learning techniques.

Currently, MRI is the most widely used clinical diagnostic tool for identifying any type of brain problem, because it is a completely non-invasive treatment. Further, the sensitivity of MR techniques over different neurological tissues is helpful in the diagnosis of various types of neurological diseases. The MR image segmentation process makes the diagnosis procedure much easier by separating out various brain structures, including cerebrospinal fluid, and grey matter, white matter. Maitra et al. [57] proposed Kapur's entropy-based multilevel thresholding method using Bacteria foraging Optimization (BFO) for brain MR image segmentation. The method is tested over nine axial, T2 weighted MRI images. The authors claimed that the suggested BFO based approach outperformed the Particle swarm optimization with linearly varying inertia weight (PSO-IW) based thresholding. An adaptive Bacteria foraging(ABF) based brain MR image segmentation is proposed in [58]. The authors compared Kapur's entropy-based approach with Otsu between class variance-based method with three different optimization algorithms. They found that Otsu-ABF is the best and most cost-effective one. Bhuvaneswari et al. [59] suggested a brain MR image segmentation as well as classification using the firefly algorithm (FFA) and Hybrid kernel-based support vector machine (HKSVM). The segmentation process comprises three phases: a dynamic region growing step for threshold selection, generation of texture features, and region merging. The thresholds in the modified region growing are optimized by the firefly method. After locating the aberrant tissues, hybrid kernel-based SVM has been used to classify the data. Social Group Optimization based multilevel thresholding [60] is another soft computing approach for brain tumor segmentation, where the Kapur's entropy based thresholded image is further processed by Watershed algorithm to extract the desired region from the scene.

Ganesh et al. [61], introduced an enhanced adaptive fuzzy K-means clustering method to distinguish different regions in Brain MR images. In this case, the result of the k-mean clustering algorithm is subjected to the morphological opening-by-reconstruction procedure to enhance the clustering performance. Researchers also investigated 2D/3D histogram-based multilevel thresholding to further improve the

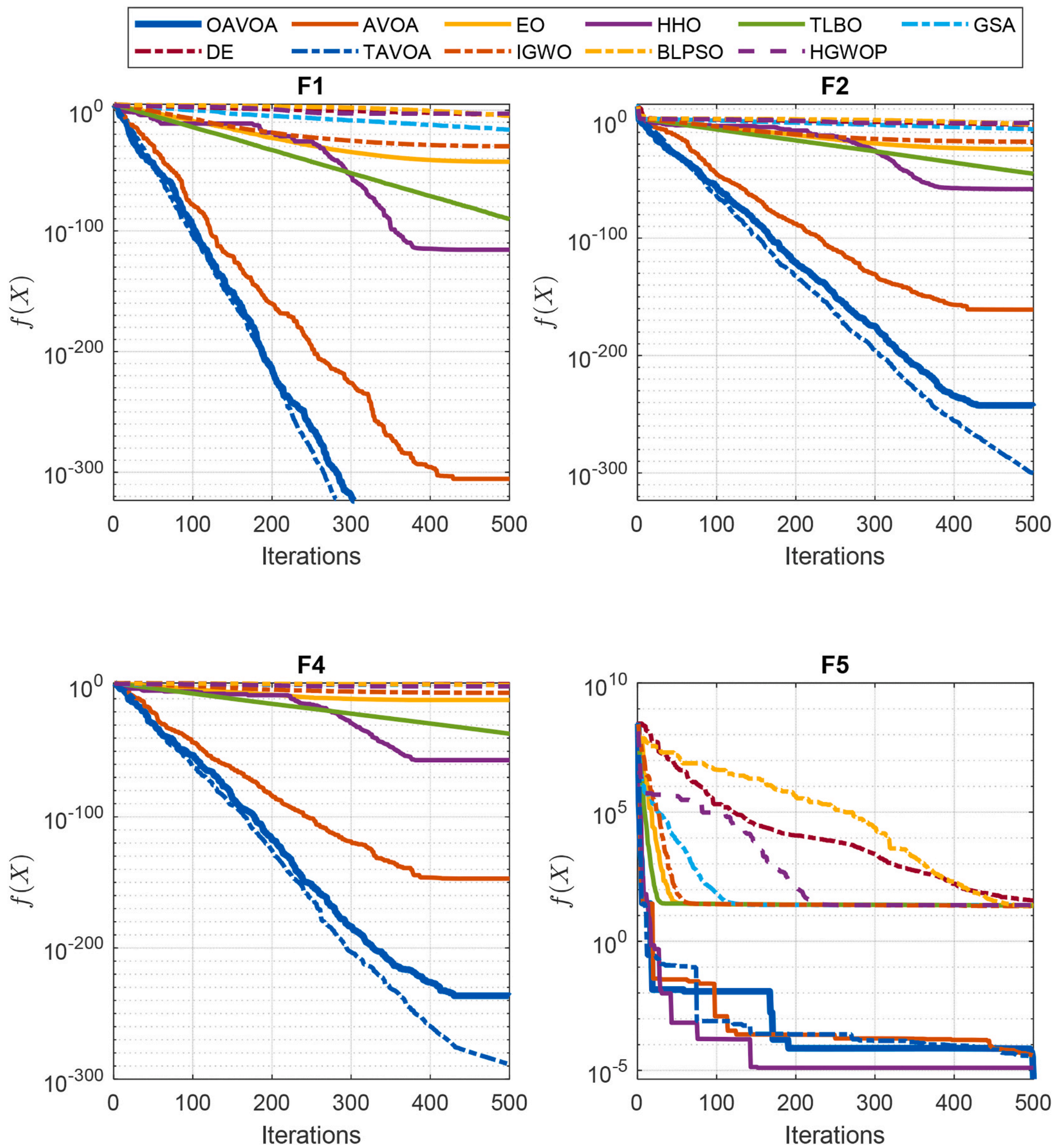

Fig. 5. Convergence plot of four unimodal function.

performance of segmentation by including spatial correlation among pixels into consideration. Sarkar et al. [62]proposed a new objective function by deriving Tsallis entropy from the 2D histogram of the image. The objective function is maximized by Differential Evolution (DE) algorithm and tested with the Berkeley dataset [63]. Feng et al. [64] investigated the Brain MRI images using a multi-scale 3D Otsu-based multilevel thresholding approach. It is an iterative approach where the image is segmented using the effective 3D Otsu, and it is then smoothed using a quick local Laplacian filter. This smoothed image is then used as the input for the following iteration. To deal with the difficult problem of separating skin lesions of healthy skin, many image segmentation techniques have been proposed by researchers.

Sumithra Attia et al. [14] suggested removing undesired hair from the lesion before running the segmentation method. Following that, colour and texture features were used to extract features. Both support vector machines (SVM) and K-nearest neighbour (KNN) were employed to classify the data. Similarly, Attia et al. [65] used convolutional and recurrent layers to create a hybrid context for hair segmentation. For hair delineation, they used deep encoded characteristics. Those were used to inscribe the spatial relationships between the incoherent image patches using recurrent layers. For skin lesion segmentation, Hawas et al. [66] suggested an Optimal Estimation of clustering using a neutrosophic graph-cut (OCE-NGC) technique. They used a meta-heuristic algorithm to improve the Clustering method based on histograms and find the best centroid/threshold values. They then used the resulting threshold value to group the pixels using the neutrosophic c-means technique. For detecting melanoma from dermoscopic pictures, Barata et al. [67] used a local-global technique. Local methods were used to extract features from bag-of-words, whereas global methods were investigated for skin lesion classification. Greater sensitivity and specificity were attained with promising outcomes.

Chatterjee et al. [68]suggested a cross-correlation-based feature extraction technique with a skin lesion categorization application. Using the cross-correlation approach, the authors looked at both spatial and spectral aspects of the lesion site. Following that, kernel patches are selected based on the types of skin diseases, which are further categorized using the recommended multi-label ensemble multi-class classifier. Khan et al. [69]provided a strategy for classifying skin lesions using probabilistic distributions, using an entropy-based method for feature selection. Based on the properties of retinal blood vessels. Tang et al. [4] introduced a back-propagation (BP) neural network-based retinal vascular segmentation technique for colour fundus images. A study on

Table 5
Statistical results and comparison of OAVOA with other optimization algorithms such as AVOA, EO, HHO, TLBO, GSA, DE, TAVOA, IGWO, BLPSO and HGWOP on multimodal functions with variable dimensions (G2).

Function		OAVOA	AVOA	EO	HHO	TLBO	GSA	DE	TAVOA	IGWO	BLPSO	HGWOP
F8	Average	−12539.868	−12242.614	−8829.986	**−12568.888**	−7710.452	−2622.178	−7455.230	−12230.642	−8707.205	−7326.038	−7210.915
	Best	**−12569.487**	−12569.487	−10243.659	**−12569.487**	−9190.530	−3702.389	−9998.600	−12569.486	−10898.353	−8374.227	−8772.956
	Median	**−12569.487**	−12553.590	−8823.352	−12569.153	−7701.897	−2524.089	−7584.527	−12568.286	−9292.033	−7336.147	−7140.444
	Worst	−12331.093	−9364.979	−7349.286	**−12564.514**	−6378.881	−1766.697	−4771.236	−9532.471	−5548.661	−6620.522	−5877.319
	Std. Dev.	71.923	676.996	612.860	**0.921**	854.938	439.884	1272.013	639.225	1463.874	456.685	915.649
F9	Average	**0**	**0**	**0**	**0**	1.274E+01	2.760E+01	1.509E+02	**0**	1.933E+01	7.063E+01	2.645E+01
	Best	**0**	**0**	**0**	**0**	**0**	1.691E+01	4.704E+01	**0**	6.068E+00	5.837E+01	8.003E+00
	Median	**0**	**0**	**0**	**0**	1.293E+01	2.487E+01	1.582E+02	**0**	1.756E+01	6.813E+01	2.500E+01
	Worst	**0**	**0**	**0**	**0**	2.518E+01	4.676E+01	2.092E+02	**0**	3.441E+01	9.067E+01	4.380E+01
	Std. Dev.	**0**	**0**	**0**	**0**	6.516E+00	6.699E+00	3.775E+01	**0**	7.900E+00	8.650E+00	8.765E+00
F10	Average	**8.882E-16**	**8.882E-16**	8.452E-15	**8.882E-16**	6.160E-15	1.225E-08	1.711E+00	**8.882E-16**	6.071E-14	2.443E-03	4.728E-02
	Best	**8.882E-16**	**8.882E-16**	7.994E-15	**8.882E-16**	4.441E-15	6.565E-09	2.758E-03	**8.882E-16**	3.997E-14	1.449E-03	1.184E-02
	Median	**8.882E-16**	**8.882E-16**	7.994E-15	**8.882E-16**	4.441E-15	1.131E-08	1.641E+00	**8.882E-16**	5.773E-14	2.330E-03	3.685E-02
	Worst	**8.882E-16**	**8.882E-16**	1.510E-14	**8.882E-16**	7.994E-15	2.706E-08	5.029E+00	**8.882E-16**	8.615E-14	5.056E-03	1.911E-01
	Std. Dev.	**0**	**0**	1.774E-15	**0**	1.805E-15	3.859E-09	1.122E+00	**0**	1.268E-14	7.931E-04	3.537E-02
F11	Average	**0**	**0**	3.180E-04	**0**	**0**	2.788E+01	2.467E-01	**0**	3.676E-03	1.154E-03	4.997E-02
	Best	**0**	**0**	**0**	**0**	**0**	1.722E+01	5.419E-03	**0**	0	2.439E-05	5.275E-03
	Median	**0**	**0**	**0**	**0**	**0**	2.742E+01	9.100E-02	**0**	0	2.780E-04	3.496E-02
	Worst	**0**	**0**	9.858E-03	**0**	**0**	4.171E+01	1.303E+00	**0**	3.258E-02	1.180E-02	1.888E-01
	Std. Dev.	**0**	**0**	1.770E-03	**0**	**0**	5.758E+00	3.426E-01	**0**	8.231E-03	2.868E-03	4.530E-02
F12	Average	**8.034E-08**	1.359E-07	5.872E-07	1.127E-05	8.674E-07	1.959E+00	1.673E+04	3.625E-07	7.020E-04	2.760E-05	1.355E-04
	Best	**3.831E-10**	2.015E-08	1.204E-08	3.547E-09	1.623E-09	3.593E-01	4.267E-01	6.123E-08	4.503E-06	2.995E-06	7.627E-06
	Median	**3.825E-08**	1.081E-07	3.737E-07	6.088E-06	1.424E-07	1.503E+00	7.063E+00	2.622E-07	7.463E-06	1.986E-05	8.381E-05
	Worst	4.121E-07	**3.502E-07**	2.925E-06	5.932E-05	6.119E-06	5.330E+00	4.556E+05	1.042E-06	6.554E-03	1.418E-04	7.883E-04
	Std. Dev.	1.038E-07	**8.335E-08**	6.118E-07	1.340E-05	1.823E-06	1.135E+00	8.173E+04	2.824E-07	1.864E-03	2.724E-05	1.628E-04
F13	Average	**9.642E-07**	8.297E-06	3.386E-02	1.250E-04	5.114E-02	1.099E+01	8.307E+04	3.743E-04	1.025E-01	7.866E-04	7.402E-03
	Best	**9.202E-09**	7.099E-07	7.143E-07	4.142E-07	2.412E-06	1.099E-02	6.778E-01	1.201E-06	8.112E-05	6.892E-05	2.079E-04
	Median	**6.706E-07**	6.994E-06	1.100E-02	4.568E-05	2.105E-02	1.087E+01	7.217E+03	1.505E-05	9.719E-02	2.001E-04	2.293E-03
	Worst	**3.414E-06**	3.603E-05	1.963E-01	6.346E-04	1.524E-01	3.425E+01	8.028E+05	1.102E-02	3.607E-01	1.233E-02	5.584E-02
	Std. Dev.	**9.988E-07**	7.751E-06	5.197E-02	1.504E-04	5.339E-02	8.315E+00	2.050E+05	1.976E-03	1.004E-01	2.215E-03	1.164E-02

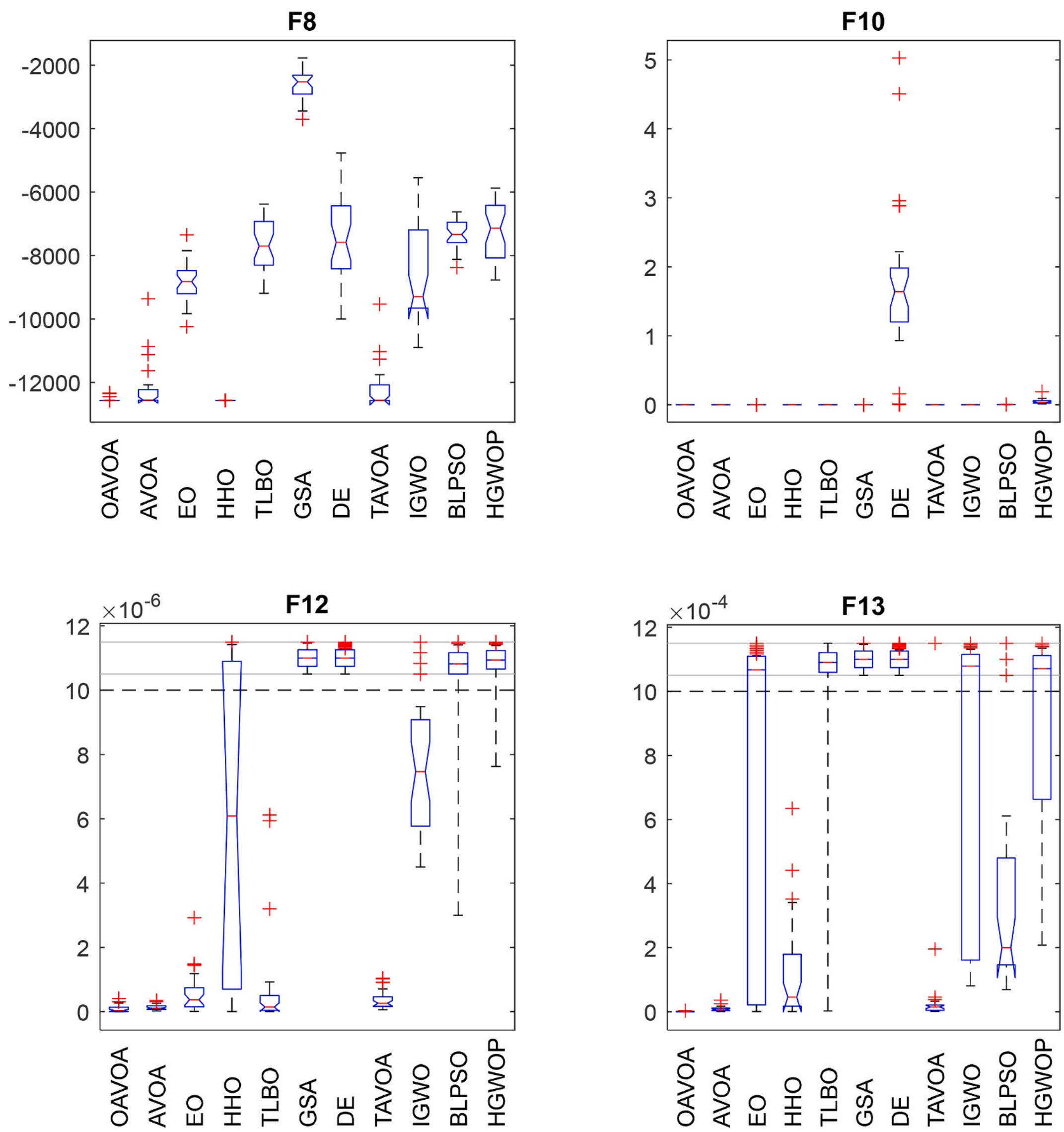

Fig. 6. Boxplot of four multimodal functions with variable dimensions.

the colour fundus image libraries DRIVE and STARE demonstrates that this technique is capable of obtaining connected vessel stems and terminals as well as a thorough segmentation of the retinal blood vessels. He et al. [3]presented a lung cancer recognition model using an Artificial Neural Network (ANN). In this method, the image segmentation algorithm was utilized to display the lung cancer lesion region individually after identifying the lung cancer lesion area. Using a short-coupled saliency detection network with neutrosophic enhancement, Hu et al. [10] introduces NeutSS-PLP, a novel technique for polyp region extraction in colonoscopy images. Results from experiments using two publicly available colorectal polyp datasets show that, for polyp extraction, the method performs better than a number of state-of-the-art saliency networks and semantic segmentation networks. However, developing a segmentation approach that is suitable for many categories of medical images, regardless of the distribution of intensities, is always a tough task for researchers.

3. Preliminaries

3.1. Description of the multilevel segmentation method

Multilevel thresholding is a simple and effective approach to the image segmentation. It divides an image into multiple sections using multiple threshold values. These values are determined by optimizing an appropriate objective function.

Let's Consider an image of size $M \times N$ with L intensity levels of $0, 1, 2 \ldots L-1$, separated into $k+1$ distinct regions. To generate $k+1$ different regions, k threshold values are needed, which can be demonstrated using a simple thresholding rule as given below in Eq (1). The pixel intensity is represented by ν, while the j^{th} the thresholded region is represented by R_j for $j \in \{1, 2, \cdots, k+1\}$. The set $[th_1, th_2, th_2 \ldots th_k]$ indicates the list of selected thresholds used for producing the thresholded image.

$$
\begin{cases}
R_1 \leftarrow \nu, \, if \ 0 \le \nu < th_1 \\
R_2 \leftarrow \nu, \, if \ th_1 \le \nu < th_2 \\
R_3 \leftarrow \nu, \, if \ th_2 \le \nu < th_3 \\
\quad \cdot \\
\quad \cdot \\
\quad \cdot \\
R_k \leftarrow \nu, \, if \ th_{k-1} \le \nu < th_k \\
R_{k+1} \leftarrow \nu, \, if \ th_k \le \nu < L-1
\end{cases}
\tag{1}
$$

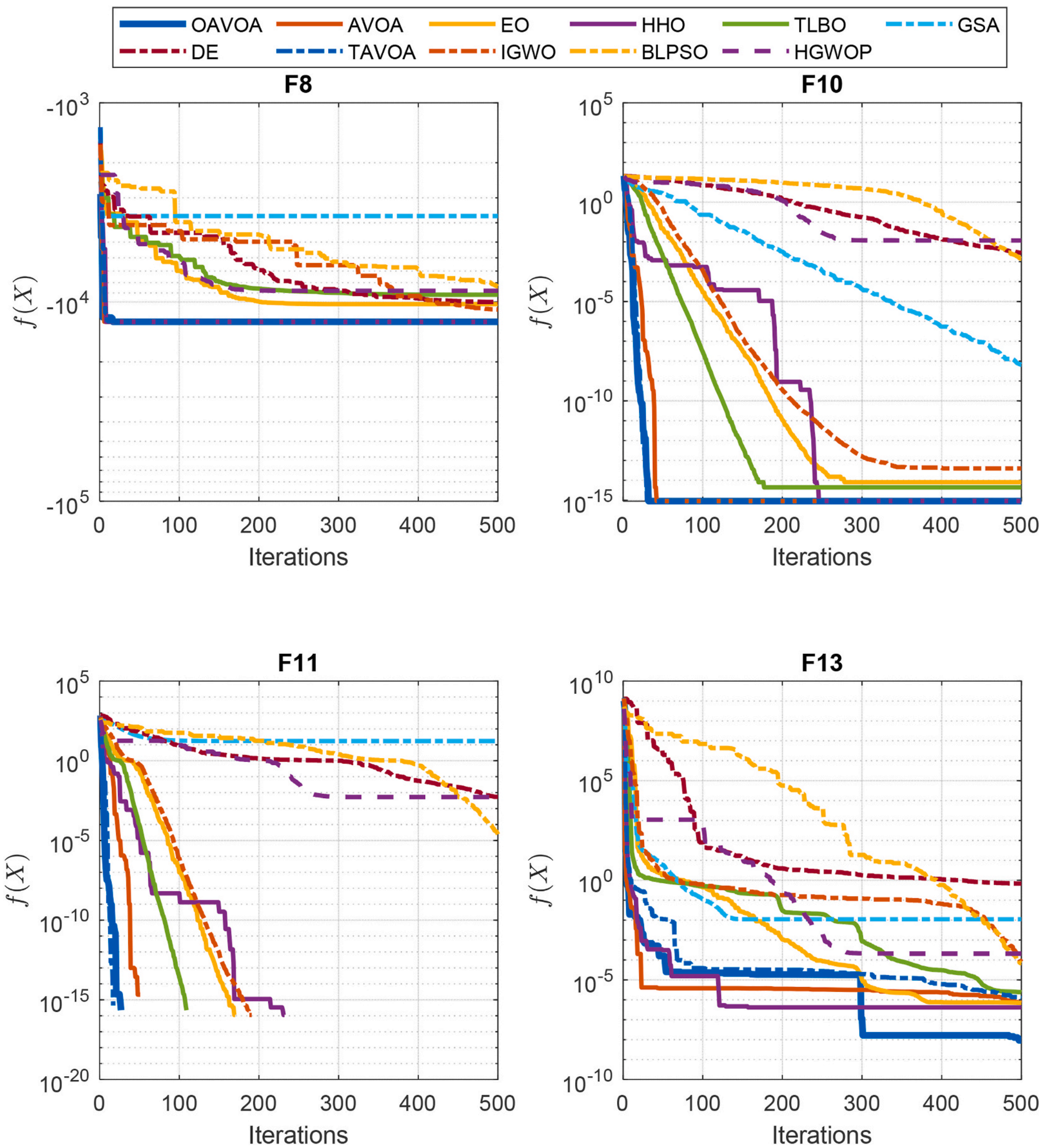

Fig. 7. Convergence plot of four multimodal functions with variable dimensions.

where $L-1$ is the maximum intensity level.

3.1.1. Entropy-based multilevel segmentation

Entropy-based multilevel thresholding is one of the convenient and effective ways of the non-parametric thresholding approach. The entropy function which is the measure of information contained in an image is used as the objective function, needs to be maximized by some meta-heuristic algorithm. Some of the popular entropy functions are Kaniadakis entropy, Masi entropy, Tsallis Entropy, Reniys entropy, Kapur's entropy, and Shannon entropy. Relative entropy is another form of entropy function which measures the informational gap between two information sources. The popular relative entropy which has been used for multilevel thresholding is the minimum cross entropy (MCE). The entropy function is derived from the probabilistic distribution of the pixel values in the image, which can be obtained from the image normalized histogram and Region probability. The normalized histogram of an image I having size $M \times N$ is defined as:

$$h_i = Pr_{(i)} = \frac{n_i}{M \times N}, i = 1, 2, 3 \dots L-1 \tag{2}$$

where n_i is the number of pixels in the image having an intensity value 'i' and $Pr_{(i)}$ is the corresponding probability.

The Region probability is expressed as:

$$P_i = \sum_{i=th_{i-1}}^{th_i} Pr_{(i)} \tag{3}$$

The optimal threshold values $[th_1^*, th_2^*, th_3^* \dots th_k^*]$ are obtained by maximizing or minimizing the objective function (OF) , derived from the entropy as given below:

$$[th_1^*, th_2^*, th_3^* \dots th_k^*] = \underset{th_1 < th_2 < th_2 \dots < th_k}{\text{argmax}/\,min} \; (OF) \tag{4}$$

Table 2 shows a brief description of the objective function (OF) derived from different entropies.

3.1.2. Generalized cross-entropy

Measuring the disparity between two probability distributions using cross-entropy fails to assess the degree of divergence associated with unknown variables. This problem is addressed by [70] to introduce a new definition of cross-entropy referred to as generalized cross-entropy.

Table 6
Statistical results and comparison of OAVOA with other optimization algorithms such as AVOA, EO, HHO, TLBO, GSA, DE, TAVOA, IGWO, BLPSO and HGWOP on multimodal functions with fixed dimensions (G3).

Function		OAVOA	AVOA	EO	HHO	TLBO	GSA	DE	TAVOA	IGWO	BLPSO	HGWOP
F14	Average	1.030	1.189	**0.998**	1.603	**0.998**	5.668	1.030	1.190	0.998	0.998	1.572
	Best	**0.998**	**0.998**	**0.998**	**0.998**	**0.998**	**0.998**	**0.998**	**0.998**	**0.998**	**0.998**	**0.998**
	Median	**0.998**	**0.998**	**0.998**	**0.998**	**0.998**	4.954	**0.998**	**0.998**	**0.998**	**0.998**	**0.998**
	Worst	1.992	5.929	**0.998**	5.929	**0.998**	13.772	1.992	2.982	**0.998**	**0.998**	5.929
	Std. Dev.	1.785E-01	8.976E-01	2.107E-16	1.478E+00	0.000E+00	3.463E+00	1.785E-01	5.963E-01	1.944E-16	**0**	1.294E+00
F15	Average	3.261E-04	3.737E-04	4.224E-03	3.763E-04	1.020E-03	4.732E-03	1.943E-03	5.001E-04	**3.075E-04**	7.035E-04	1.923E-03
	Best	**3.075E-04**	**3.075E-04**	**3.075E-04**	3.089E-04	**3.075E-04**	1.013E-03	**3.075E-04**	**3.075E-04**	**3.075E-04**	6.025E-04	3.075E-04
	Median	3.101E-04	3.118E-04	3.138E-04	3.304E-04	**3.075E-04**	3.675E-03	4.698E-04	3.809E-04	**3.075E-04**	6.919E-04	4.938E-04
	Worst	7.690E-04	1.223E-03	2.036E-02	1.536E-03	2.036E-02	1.101E-02	2.036E-02	1.223E-03	**3.075E-04**	1.404E-03	2.036E-02
	Std. Dev.	8.234E-05	1.814E-04	8.039E-03	2.174E-04	3.594E-03	2.753E-03	4.944E-03	2.647E-04	**2.434E-09**	1.341E-04	4.939E-03
F16	Average	**−1.032**	**−1.032**	**−1.032**	**−1.032**	**−1.032**	**−1.032**	**−1.032**	**−1.032**	**−1.032**	**−1.032**	**−1.032**
	Best	**−1.032**	**−1.032**	**−1.032**	**−1.032**	**−1.032**	**−1.032**	**−1.032**	**−1.032**	**−1.032**	**−1.032**	**−1.032**
	Median	**−1.032**	**−1.032**	**−1.032**	**−1.032**	**−1.032**	**−1.032**	**−1.032**	**−1.032**	**−1.032**	**−1.032**	**−1.032**
	Worst	**−1.032**	**−1.032**	**−1.032**	**−1.032**	**−1.032**	**−1.032**	**−1.032**	**−1.032**	**−1.032**	**−1.032**	**−1.032**
	Std. Dev.	5.091E-11	2.109E-14	6.135E-16	5.677E-09	6.710E-16	4.780E-16	6.771E-16	**4.328E-16**	6.332E-16	3.292E-06	6.771E-16
F17	Average	**0.398**	**0.398**	**0.398**	**0.398**	**0.398**	**0.398**	**0.398**	**0.398**	**0.398**	**0.398**	**1.866**
	Best	**0.398**	**0.398**	**0.398**	**0.398**	**0.398**	**0.398**	**0.398**	**0.398**	**0.398**	**0.398**	**0.496**
	Median	**0.398**	**0.398**	**0.398**	**0.398**	**0.398**	**0.398**	**0.398**	**0.398**	**0.398**	**0.398**	**1.714**
	Worst	**0.398**	**0.398**	**0.398**	**0.398**	**0.398**	**0.398**	**0.398**	**0.398**	**0.398**	**0.398**	**3.963**
	Std. Dev.	1.878E-09	3.362E-14	**0**	3.717E-05	**0**	**0**	**0**	4.988E-14	**0**	**0**	8.813E-01
F18	Average	**3**	**3**	**3**	3.000	**3**	**3**	**3**	3.000	**3**	**3**	2.337E+02
	Best	**3**	**3**	**3**	**3**	**3**	**3**	**3**	**3**	**3**	**3**	3.047E+00
	Median	**3**	**3**	**3**	**3**	**3**	**3**	**3**	3.000	**3**	**3**	2.032E+02
	Worst	**3**	**3**	**3**	3.000	**3**	**3**	**3**	3.000	**3**	**3**	5.296E+02
	Std. Dev.	8.021E-09	1.826E-12	**1.219E-15**	1.898E-07	1.860E-15	4.351E-15	2.334E-15	6.042E-06	1.748E-15	1.253E-15	1.584E+02
F19	Average	**−3.863**	**−3.863**	**−3.863**	**−3.860**	**−3.863**	**−3.863**	**−3.863**	**−3.863**	**−3.863**	**−3.863**	−2.911
	Best	**−3.863**	**−3.863**	**−3.863**	**−3.863**	**−3.863**	**−3.863**	**−3.863**	**−3.863**	**−3.863**	**−3.863**	−3.669
	Median	**−3.863**	**−3.863**	**−3.863**	**−3.861**	**−3.863**	**−3.863**	**−3.863**	**−3.863**	**−3.863**	**−3.863**	−2.991
	Worst	**−3.863**	**−3.863**	**−3.863**	**−3.853**	**−3.863**	**−3.863**	**−3.863**	**−3.863**	**−3.863**	**−3.863**	−2.087
	Std. Dev.	1.445E-07	3.549E-11	2.500E-15	2.705E-03	2.709E-15	**2.257E-15**	2.709E-15	4.259E-09	2.529E-15	2.695E-15	4.699E-01
F20	Average	−3.303	−3.284	−3.269	−3.101	−3.294	**−3.318**	−3.245	−3.283	−3.313	−3.299	−1.171
	Best	**−3.322**	**−3.322**	**−3.322**	−3.271	**−3.322**	**−3.322**	**−3.322**	**−3.322**	**−3.322**	**−3.322**	−2.042
	Median	**−3.322**	**−3.322**	**−3.322**	−3.130	**−3.322**	**−3.322**	**−3.203**	**−3.322**	**−3.322**	**−3.322**	−1.055
	Worst	**−3.203**	**−3.203**	−3.133	−2.810	**−3.203**	**−3.203**	**−3.203**	−3.198	−3.203	−3.203	−0.553
	Std. Dev.	4.448E-02	5.650E-02	6.965E-02	1.118E-01	5.002E-02	**2.139E-02**	5.784E-02	5.677E-02	2.920E-02	4.775E-02	4.160E-01
F21	Average	**−10.153**	**−10.153**	−8.026	−5.053	−9.826	−5.876	−9.342	**−10.153**	−10.129	−9.523	−0.404
	Best	**−10.153**	**−10.153**	**−10.153**	−5.055	**−10.153**	**−10.153**	**−10.153**	**−10.153**	**−10.153**	**−10.153**	−1.327
	Median	**−10.153**	**−10.153**	**−10.153**	−5.054	**−10.153**	−2.973	**−10.153**	**−10.153**	**−10.153**	**−10.153**	−0.372
	Worst	**−10.153**	**−10.153**	−2.630	−5.043	−5.055	−2.630	−2.683	**−10.153**	−9.432	−2.683	−0.261
	Std. Dev.	7.920E-08	2.384E-10	2.780E+00	3.030E-03	1.267E+00	3.700E+00	2.185E+00	**1.503E-10**	1.295E-01	1.928E+00	1.918E-01
F22	Average	**−10.403**	**−10.403**	−9.567	−5.230	−10.016	−9.876	−9.941	**−10.403**	**−10.403**	**−10.403**	−0.491
	Best	**−10.403**	**−10.403**	**−10.403**	−9.652	**−10.403**	**−10.403**	**−10.403**	**−10.403**	**−10.403**	**−10.403**	−0.748
	Median	**−10.403**	**−10.403**	**−10.403**	−5.085	**−10.403**	**−10.403**	**−10.403**	**−10.403**	**−10.403**	**−10.403**	−0.459
	Worst	**−10.403**	**−10.403**	−2.766	−5.066	−3.724	−3.906	−2.752	**−10.403**	**−10.403**	**−10.403**	−0.302
	Std. Dev.	1.254E-07	4.204E-11	2.247E+00	8.206E-01	1.507E+00	1.541E+00	1.794E+00	2.193E-10	3.181E-08	**2.270E-15**	1.166E-01
F23	Average	**−10.536**	**−10.536**	−10.362	−5.415	−10.358	**−10.536**	−10.320	**−10.536**	**−10.536**	**−10.536**	−0.635
	Best	**−10.536**	**−10.536**	**−10.536**	−9.754	**−10.536**	**−10.536**	**−10.536**	**−10.536**	**−10.536**	**−10.536**	−0.971
	Median	**−10.536**	**−10.536**	**−10.536**	−5.126	**−10.536**	**−10.536**	**−10.536**	**−10.536**	**−10.536**	**−10.536**	−0.602
	Worst	**−10.536**	**−10.536**	−5.128	−5.071	−5.006	**−10.536**	−3.835	**−10.536**	**−10.536**	**−10.536**	−0.416
	Std. Dev.	1.701E-07	2.385E-11	9.713E-01	1.132E+00	9.933E-01	4.799E-15	1.204E+00	1.623E-10	5.603E-09	**2.270E-15**	1.554E-01

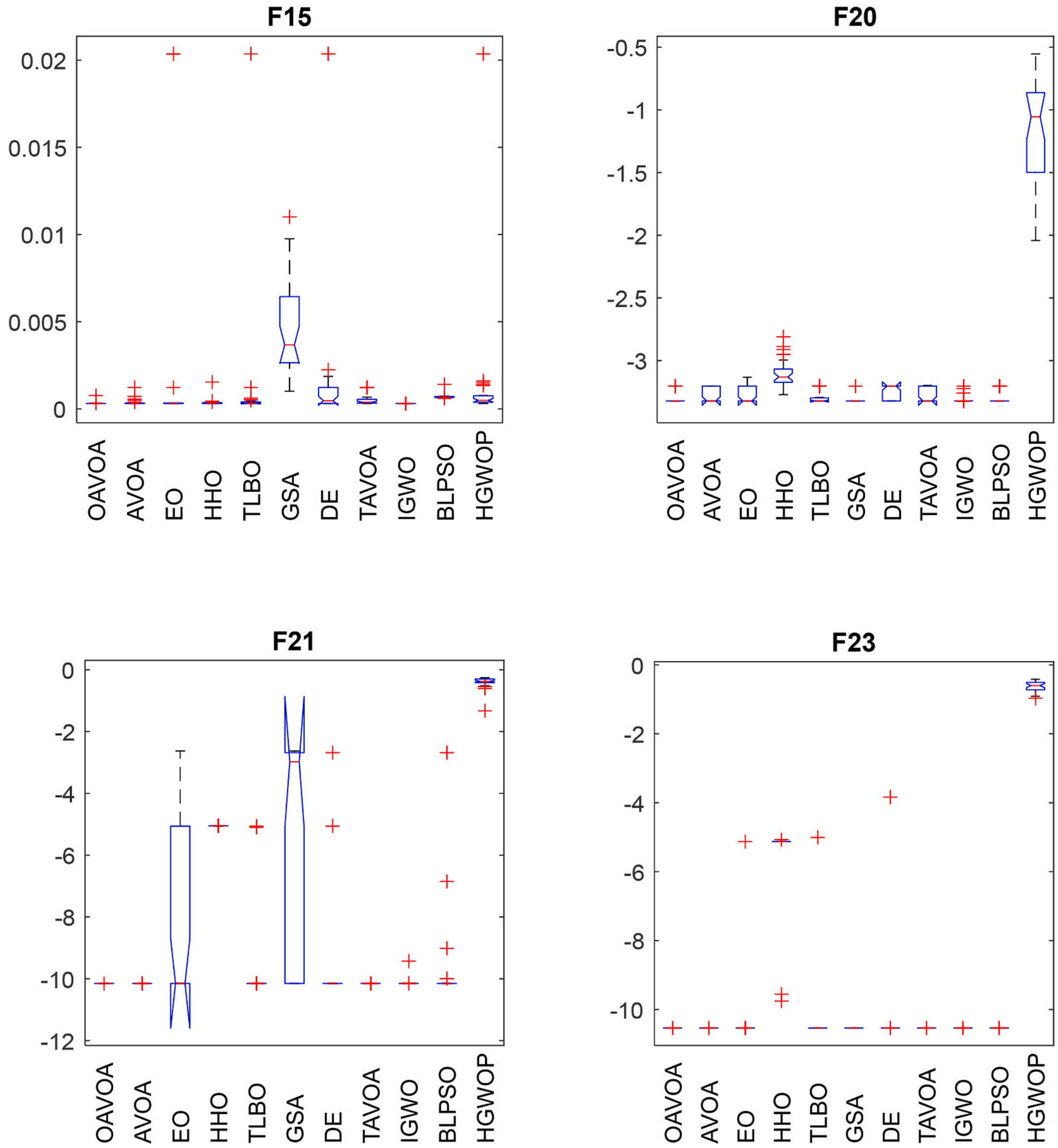

Fig. 8. Boxplot of four multimodal functions with fixed dimensions.

Let ξ and η be two unknown variables, each with its probability distribution φ and ψ respectively. The generalized cross-entropy is thus defined as follows:

$$GCE[\xi,\eta] = \left(\int_{-\infty}^{\infty} |\varphi(x) - \psi(x)|^p \, dx \right)^{\frac{1}{p}} \tag{5}$$

where the parameter p indicates the degree of divergence index.

3.2. African vulture optimization algorithm (AVOA)

African vultures optimization algorithm (AVOA) [29] imitates the foraging and navigation behaviors of African vultures for searching for the optimal solution. In Africa, there are a variety of vultures, the majority of which have a similar lifestyle and hunt for food, frequently colliding and fighting over food. Vultures' proclivity for eating and searching for food causes them not only to reach the optimal food source but also to flee the hunger trap. This concept in the foraging strategy is used by the authors in the paper to develop a novel optimization algorithm.

The AVOA algorithm undergoes 4 different phases such as: identifying the best vulture in the population, vulture hunger rates, exploration, and exploitation. The mathematical formulations of different phases of the AVOA algorithm are discussed below.

The AVOA algorithm starts with an initial population matrix (G) of size $N \times dim$ to solve a given optimization problem.

$$G = \begin{bmatrix} G_1 \\ G_2 \\ \vdots \\ G_N \end{bmatrix} = \begin{bmatrix} g_{1,1} & g_{1,2} & \cdots & g_{1,dim} \\ g_{2,1} & g_{2,2} & \cdots & g_{2,dim} \\ \vdots & \vdots & \vdots & \vdots \\ g_{N,1} & g_{N,2} & \cdots & g_{N,dim} \end{bmatrix} \tag{6}$$

where N and dim represent the number of vultures referred to as solution vectors in the population matrix and dimension of the problem respectively. At the starting phase, each solution G_i in the population matrix G need to be initialized as:

$$G_i = lb + rand(1, dim) \times (ub - lb) \tag{7}$$

where lb and ub denote the lower and upper bound of the search space, $rand(1, dim)$ generates a sequence of a random number in the range $[0, 1]$ of length dim.

Following the initialization of the population, the fitness-related to

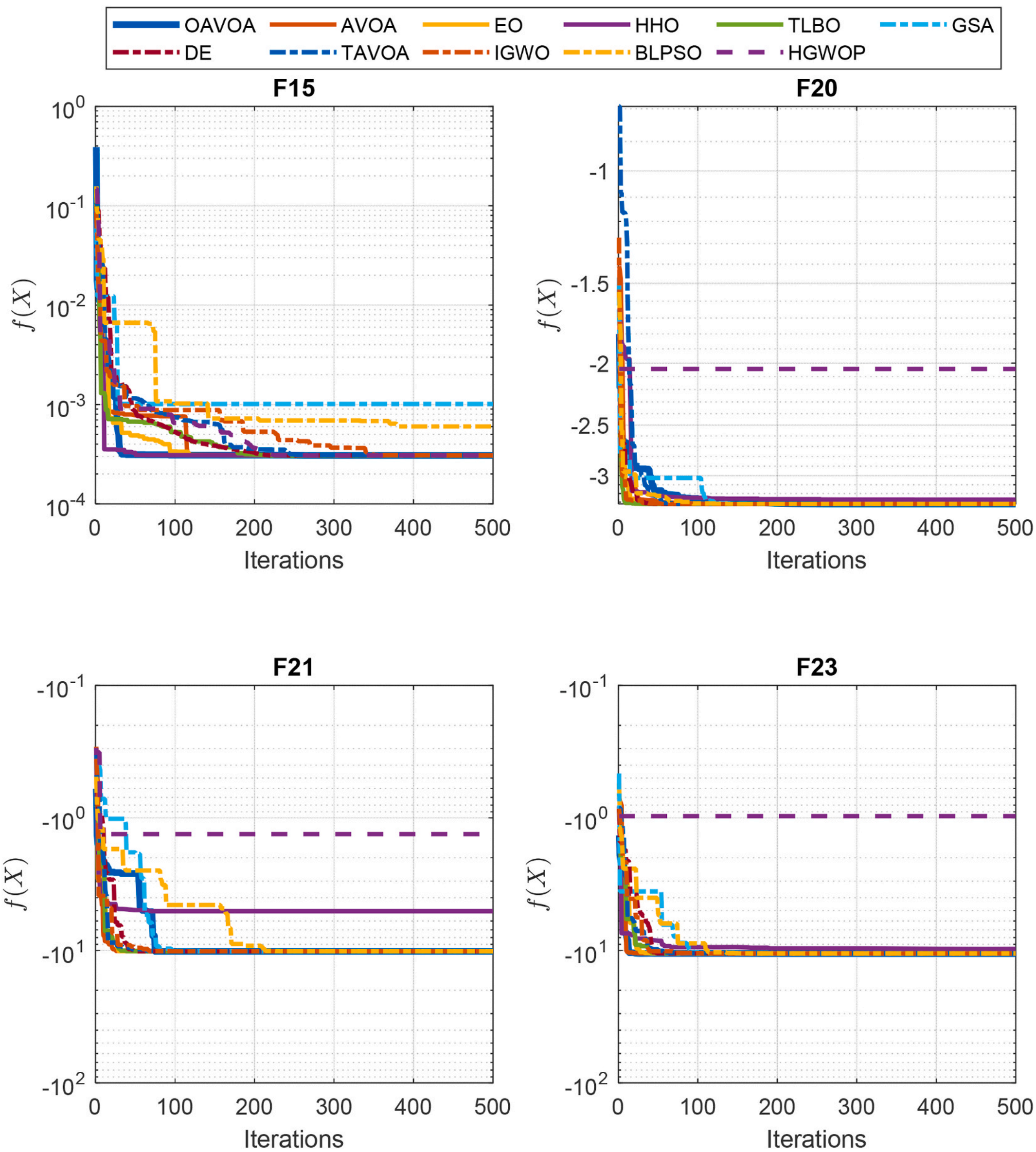

Fig. 9. Convergence plot of four multimodal functions with fixed dimensions.

each vulture is computed by evaluating the objective function and represented in the form of a fitness matrix as:

$$fitness = \begin{bmatrix} fitness(G_1) \\ fitness(G_2) \\ \vdots \\ fitness(G_N) \end{bmatrix} \tag{8}$$

(a) Phase-1: Finding the best vulture in the population

According to the fitness values, the two best vultures are selected which then guide the remaining solutions by dividing them into two groups randomly. The selection of best vulture's process modelled mathematically as:

$$V^t = \begin{cases} Best\ Vulture^t, if\ pr_i^t = L_1 \\ Second\ bestVulture^t, if\ pr_i^t = L_2 \end{cases} \tag{9}$$

where L_1 and L_2 are the random number defined at the beginning of the process in the range $[0, 1]$ such that $L_1 + L_2 = 1$. The Roulette wheel method is adopted to determine the probability of selection pr_i^t among the two best vultures at iteration 't' for the i^{th} vulture in the population as formulated below:

$$pr_i^t = \frac{fitness(G_i)}{\sum_{l=1}^{N} fitness(G_i)} \tag{10}$$

(b) Vulture hunger rates

The level of hunger in vultures is used to provide a transition from the exploration to the exploitation stage. The following equation can be used to compute the vulture's hunger degree F^t at the t^{th} iteration.

$$F^t = (2a + 1) \times b \times \left(1 - \frac{t}{T}\right) + \vartheta^t \tag{11}$$

where a and b are random numbers defined in the range $[0, 1]$ and $[-1, 1]$ respectively. T denotes the maximum number of iterations. The factor ϑ^t is determined as:

Table 7
Statistical results and comparison of OAVOA with other optimization algorithms such as AVOA, EO, HHO, TLBO, GSA, DE, TAVOA, IGWO, BLPSO and HGWOP on composition functions (G4) form CEC 2014 test suite.

Function		OAVOA	AVOA	EO	HHO	TLBO	GSA	DE	TAVOA	IGWO	BLPSO	HGWOP
F24 (CEC14-F23)	Average	**2500**	**2500**	2615.313	**2500**	2615.434	2654.990	2616.145	**2500**	2616.200	2615.301	3667.400
	Best	**2500**	**2500**	2615.246	**2500**	2615.244	**2500**	2615.246	**2500**	2615.572	2615.245	3303.888
	Median	**2500**	**2500**	2615.282	**2500**	2615.263	2698.088	2615.591	**2500**	2616.019	2615.268	3646.067
	Worst	**2500**	**2500**	2615.588	**2500**	2619.754	2842.507	2620.635	**2500**	2618.694	2615.626	4205.578
	Std. Dev.	**0**	**0**	7.918E-02	**0**	8.106E-01	1.027E+02	1.375E+00	**0**	6.514E-01	9.478E-02	2.452E+02
F25 (CEC14-F24)	Average	**2600**	**2600**	2600.020	**2600**	2600.036	2624.903	2640.442	**2600**	2600.866	2626.286	2883.614
	Best	**2600**	**2600**	2600.010	**2600**	2600.023	2614.130	2627.024	**2600**	2600.055	2624.277	2792.542
	Median	**2600**	**2600**	2600.019	**2600**	2600.035	2625.167	2641.313	**2600**	2600.096	2626.102	2891.895
	Worst	**2600**	**2600**	2600.035	2600.003	2600.054	2636.111	2650.559	**2600**	2623.848	2628.981	2937.274
	Std. Dev.	**0**	1.510E-10	8.019E-03	4.877E-04	7.789E-03	5.203E+00	5.567E+00	**0**	4.265E+00	1.111E+00	3.645E+01
F26 (CEC14-F25)	Average	**2700**	**2700**	2701.622	**2700**	2700.334	2708.610	2706.092	**2700**	2706.358	2714.530	2809.397
	Best	**2700**	**2700**	**2700**	**2700**	**2700**	2701.946	2703.949	**2700**	2700.000	2711.642	2748.136
	Median	**2700**	**2700**	**2700**	**2700**	**2700**	2708.442	2705.695	**2700**	2706.538	2714.446	2807.410
	Worst	**2700**	**2700**	2712.510	**2700**	2709.654	2713.980	2711.390	**2700**	2708.548	2717.993	2889.775
	Std. Dev.	**0**	**0**	3.845E+00	**0**	1.734E+00	2.409E+00	1.485E+00	**0**	1.594E+00	1.629E+00	3.218E+01
F27 (CEC14-F26)	Average	**2700.508**	2700.509	2729.979	2777.542	2735.835	2793.524	2710.789	2755.088	2717.708	2745.105	2782.239
	Best	2700.279	2700.227	**2700.194**	2700.346	2700.346	2711.552	2700.373	2700.414	2700.282	2700.366	2707.287
	Median	2700.500	2700.501	**2700.399**	2800.000	2700.668	2800.125	2700.533	2800	2700.498	2702.576	2711.387
	Worst	**2700.820**	2700.915	2920.794	2800.000	2800.097	2800.332	2917.313	2800	2800.344	2801.757	3014.300
	Std. Dev.	**1.304E-01**	1.668E-01	5.504E+01	4.227E+01	4.839E+01	1.980E+01	4.230E+01	5.031E+01	3.733E+01	4.987E+01	1.253E+02
F28 (CEC14-F27)	Average	**2900**	**2900**	3285.769	**2900**	3334.604	4767.069	3239.448	**2900**	3180.862	3062.079	4135.982
	Best	**2900**	**2900**	3109.692	**2900**	3103.223	3694.090	3102.792	**2900**	3090.475	3021.385	3726.376
	Median	**2900**	**2900**	3286.278	**2900**	3282.315	4715.652	3248.254	**2900**	3155.574	3035.744	4153.706
	Worst	**2900**	**2900**	3451.682	**2900**	3613.073	5433.479	3408.669	**2900**	3417.996	3257.085	4288.827
	Std. Dev.	**0**	**0**	9.075E+01	**0**	2.056E+02	3.750E+02	9.065E+01	**0**	8.197E+01	5.994E+01	1.173E+02
F29 (CEC14-F28)	Average	**3000**	**3000**	3822.171	**3000**	4057.028	6390.381	3918.293	**3000**	3785.436	3874.189	5833.184
	Best	**3000**	**3000**	3610.634	**3000**	3734.977	4187.656	3666.856	**3000**	3621.340	3794.760	4437.236
	Median	**3000**	**3000**	3758.529	**3000**	3943.677	6395.614	3798.095	**3000**	3736.348	3879.250	5811.569
	Worst	**3000**	**3000**	4558.489	**3000**	4670.084	8549.415	4778.105	**3000**	4106.263	3979.374	7422.564
	Std. Dev.	**0**	**0**	2.056E+02	**0**	2.699E+02	8.943E+02	2.630E+02	**0**	1.276E+02	3.906E+01	5.825E+02
F30 (CEC14-F29)	Average	**3100**	2.626E+05	3.128E+06	7.469E+05	1.719E+06	2.307E+08	2.707E+06	2.432E+06	2.181E+04	2.095E+04	2.057E+07
	Best	**3100**	**3100**	4.123E+03	**3100**	3.935E+03	3.100E+03	4.314E+03	**3100**	1.079E+04	9.209E+03	6.461E+06
	Median	**3100**	**3100**	5.808E+03	**3100**	5.428E+03	1.640E+08	7.163E+03	**3100**	2.236E+04	2.094E+04	1.710E+07
	Worst	**3100**	7.888E+06	1.249E+07	2.306E+07	1.750E+07	6.576E+08	2.376E+07	1.218E+07	3.341E+04	3.668E+04	8.487E+07
	Std. Dev.	**0**	1.415E+06	4.652E+06	4.141E+06	4.665E+06	1.975E+08	5.728E+06	4.144E+06	5.102E+03	5.729E+03	1.389E+07
F31 (CEC14-F30)	Average	**8.644E+03**	2.557E+04	9.689E+03	1.507E+05	1.197E+04	2.042E+06	1.173E+04	2.946E+04	1.009E+04	1.168E+04	5.498E+05
	Best	**3200**	**3200**	5.194E+03	3200	4.877E+03	9.235E+05	4.683E+03	**3200**	5.473E+03	7.653E+03	2.795E+05
	Median	**3200**	2.139E+04	8.017E+03	3200	7.888E+03	1.897E+06	6.835E+03	2.300E+04	9.479E+03	1.088E+04	5.233E+05
	Worst	1.018E+05	9.242E+04	**2.384E+04**	9.044E+05	6.208E+04	3.819E+06	8.678E+04	1.085E+05	2.452E+04	2.240E+04	1.235E+06
	Std. Dev.	1.898E+04	2.314E+04	**4.774E+03**	2.700E+05	1.174E+04	6.177E+05	1.506E+04	2.562E+04	4.053E+03	2.893E+03	2.163E+05

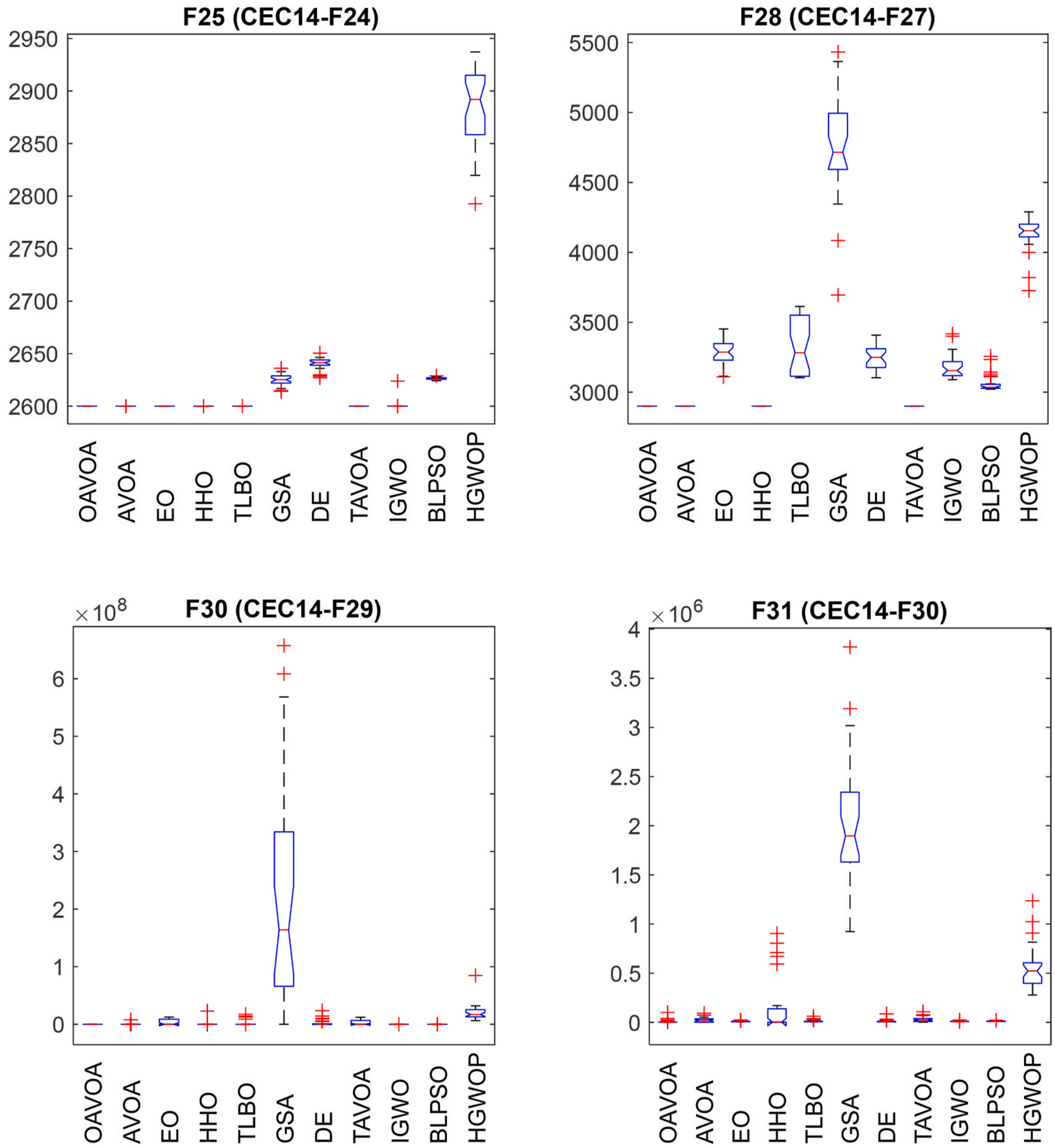

Fig. 10. Boxplot of four composition functions from CEC2014 test suit.

$$\vartheta^t = \gamma^t \times \left(sin^{\omega}\left(\frac{\pi}{2}\times\frac{t}{T}\right) + cos\left(\frac{\pi}{2}\times\frac{t}{T}\right) - 1\right) \tag{12}$$

where γ^t denotes a random number taken in between -2 and 2, and ω is a pre-optimization parameter with a fixed value, which denotes the likelihood of the vulture carrying out the exploitation stage. When the value ω is high, the chance of reaching the exploration phase increases while dealing with the final phase. However, reducing the value ω reduces the likelihood of entering the exploratory phase. According to the design concept, F^t is steadily drop with progress in iterations and the range of falling becomes more for each iteration. When $F^t \geq 1$, they enter the exploration stage and search for new food in various locations. When F^t is smaller than 1, vultures enter the exploitation stage, looking for better food in the immediate vicinity.

(c) Exploration

In the AVOA algorithm, two different exploration mechanisms are performed in a random manner. The mathematical representation of the exploration stage is expressed in Eq. (13).

$$G_i^{t+1} = \begin{cases} V^t - D_i^t \times F^t, if\ p_1 \geq r_1 \\ V^t - F_i^t + r_2 \times ((ub - lb) \times r_3 + lb), if\ p_1 < r_1 \end{cases} \tag{13}$$

The parameter p_1 represent the likelihood of selecting an exploration mechanism and is set to a value within the range [0, 1] at the beginning of the search process. G_i^{t+1} is the updated position for the next $(t+1)^{th}$ iteration. r_1, r_2 and r_3 are uniformly distributed random numbers in the range $[0,1]$. The random distance from the best vulture D_i^t in the above equation can be calculated as

$$D_i^t = |Y \times V_i^t - G_i^t| \tag{14}$$

where Y is random in nature and distributed uniformly within the range $[0,2]$ and G_i^t is i^{th} vulture's location in t^{th} iteration.

(c) Exploitation

If the value of $|F^t|$ is less than one, the algorithm is ready to initiate the exploitation process, which is divided into two phases, each having two possible methods. Two factors p_2 and p_3 signify the degree to which

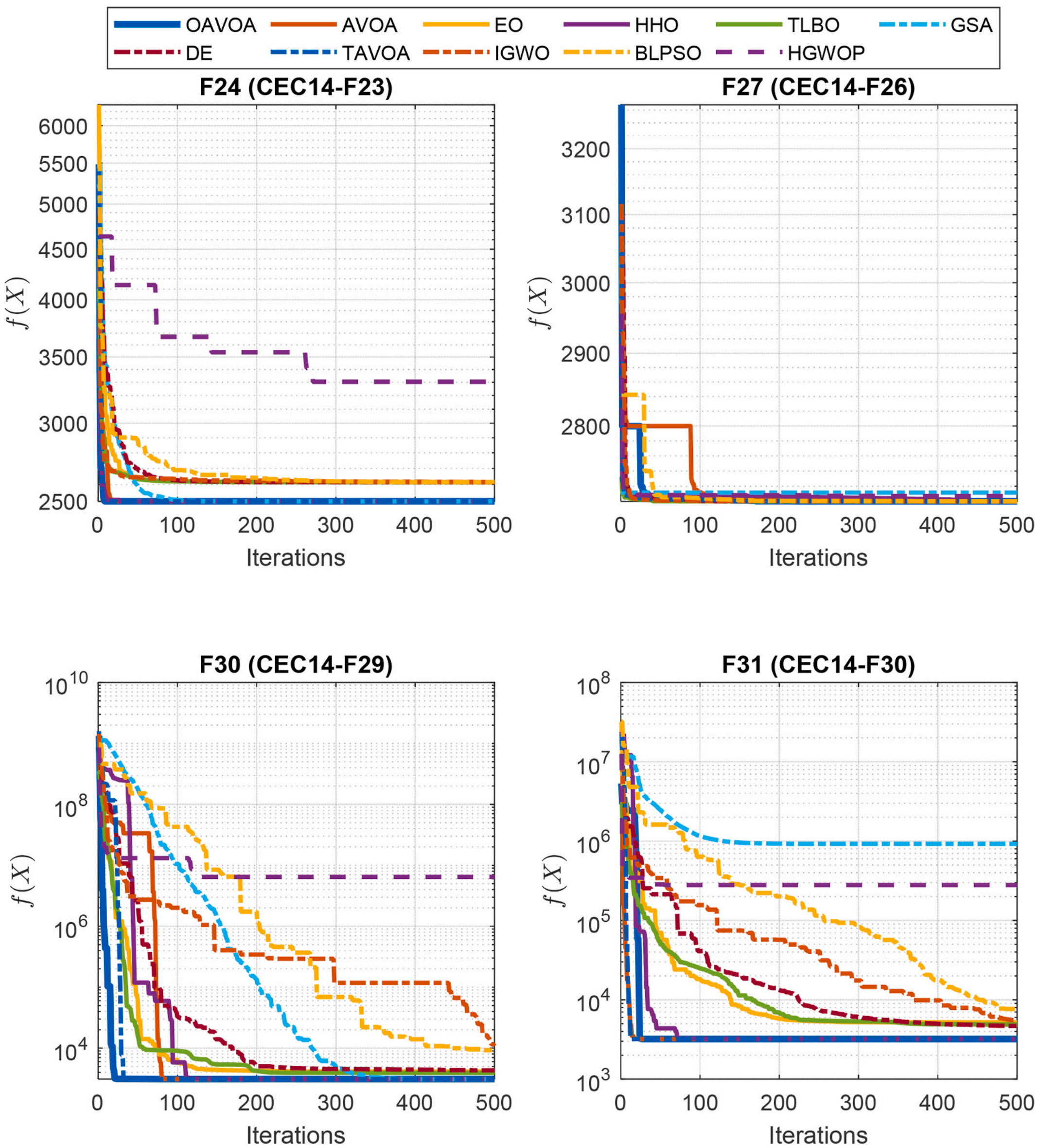

Fig. 11. Convergence plot of four composition functions from CEC2014 test suit.

each method is chosen in each phase of exploration introduced in this stage. Before executing the search, both parameters must be assigned with a value within the range [0, 1].

(i) Exploitation phase 1

When the value $|F^t|$ is between 1 and 0.5, the vultures are somewhat satisfied and have sufficient energy. In this phase, AVOA performs food competitions or rotating flight operations randomly. Therefore, a random number r_4 lies between 0 and 1, is generated at the beginning of this phase to control this process. The above operation is expressed mathematically as given below:

$$G_i^{t+1} = \begin{cases} \text{Food competition}, & r_4 \geq p_2 \\ \text{Rotational flight}, & r_4 < p_2 \end{cases} = \begin{cases} D_i^t \times (F^t + r_5) - d_i^t, & r_4 \geq p_2 \\ V_i^t - (Q_{i1}^t + Q_{i2}^t), & r_4 < p_2 \end{cases} \tag{15}$$

where r_5 is random in nature and its value is within 0 and 1. d_i^t, Q_{i1}^t and Q_{i2}^t are calculated by the following expression

$$d_i^t = V^t - G_i^t \tag{16}$$

$$Q_{i1}^t = V^t \times \left(\frac{r_6 - G_i^t}{2\pi}\right) \times \cos\left(G_i^t\right) \tag{17}$$

and

$$Q_{i2}^t = V^t \times \left(\frac{r_7 - G_i^t}{2\pi}\right) \times \sin\left(G_i^t\right) \tag{18}$$

where r_6 and r_7 denote random numbers generated uniformly in the interval [0, 1].

(ii) Exploitation phase 2

When $|F^t|$ is fallen below 0.5, the second phase of exploitation begins. In this case, the best two vultures' movements aggregate multiple types of vultures around the same food source. Later, the vultures start attacking the food. The above activities are regulated by a random number r_8 in the range [0, 1] defined at the initiation of this phase. The second phase of exploitation can be implemented in the algorithm with following expression:

Table 8
p-value of OAVOA vs. another algorithm using Wilcoxon rank-sum test with 95% significance.

Function	AVOA	EO	HHO	TLBO	GSA	DE	TAVOA	IGWO	BLPSO	HGWOP
F1	5.960E-08	5.960E-08	5.960E-08	5.960E-08	5.960E-08	5.960E-08	**1**	5.960E-08	5.960E-08	5.960E-08
F2	5.960E-08	5.960E-08	5.960E-08	5.960E-08	5.960E-08	5.960E-08	5.960E-08	5.960E-08	5.960E-08	5.960E-08
F3	5.960E-08	5.960E-08	5.960E-08	5.960E-08	5.960E-08	5.960E-08	**1**	5.960E-08	5.960E-08	5.960E-08
F4	5.960E-08	5.960E-08	5.960E-08	5.960E-08	5.960E-08	5.960E-08	5.960E-08	5.960E-08	5.960E-08	5.960E-08
F5	4.329E-02	5.960E-08	4.077E-03	5.960E-08	5.960E-08	5.960E-08	9.105E-04	5.960E-08	5.960E-08	5.960E-08
F6	1.943E-05	1.943E-05	4.077E-03	9.105E-04	5.960E-08	5.960E-08	1.565E-04	5.960E-08	5.960E-08	5.960E-08
F7	4.077E-03	1.550E-06	**6.900E-01**	5.960E-08	5.960E-08	5.960E-08	**1**	5.960E-08	5.960E-08	5.960E-08
F8	1.943E-05	5.960E-08	4.077E-03	5.960E-08	5.960E-08	5.960E-08	1.565E-04	5.960E-08	5.960E-08	5.960E-08
F9	**1**	**1**	**1**	1.192E-07	5.960E-08	5.960E-08	**1**	5.960E-08	5.960E-08	5.960E-08
F10	**1**	5.960E-08	**1**	5.960E-08	5.960E-08	5.960E-08	**1**	5.960E-08	5.960E-08	5.960E-08
F11	**1**	**1**	**1**	**1**	5.960E-08	5.960E-08	**1**	**3.125E-02**	5.960E-08	5.960E-08
F12	**4.244E-01**	1.565E-04	1.550E-06	4.329E-02	5.960E-08	5.960E-08	9.105E-04	5.960E-08	5.960E-08	5.960E-08
F13	9.105E-04	1.550E-06	5.960E-08	5.960E-08	5.960E-08	5.960E-08	1.550E-06	5.960E-08	5.960E-08	5.960E-08
F14	4.025E-04	9.537E-07	5.960E-08	5.960E-08	5.960E-08	1.550E-06	**3.516E-02**	1.192E-07	5.960E-08	**1.078E-01**
F15	**4.244E-01**	**1.078E-01**	5.960E-08	**2.295E-01**	5.960E-08	**1.078E-01**	1.550E-06	5.960E-08	5.960E-08	1.943E-05
F16	5.960E-08	5.960E-08	**0.690038**	5.960E-08	5.960E-08	5.960E-08	5.960E-08	5.960E-08	1.565E-04	5.960E-08
F17	5.960E-08	5.960E-08	1.943E-05	5.960E-08	5.960E-08	5.960E-08	1.550E-06	5.960E-08	5.960E-08	5.960E-08
F18	5.960E-08	5.960E-08	**1.078E-01**	5.960E-08	5.960E-08	5.960E-08	1.550E-06	5.960E-08	5.960E-08	5.960E-08
F19	5.960E-08	5.960E-08	5.960E-08	5.960E-08	5.960E-08	5.960E-08	1.550E-06	5.960E-08	5.960E-08	5.960E-08
F20	4.329E-02	**6.900E-01**	1.550E-06	**1.078E-01**	1.550E-06	**6.900E-01**	**1.078E-01**	9.105E-04	4.077E-03	5.960E-08
F21	5.960E-08	**6.900E-01**	5.960E-08	1.565E-04	**2.295E-01**	1.565E-04	5.960E-08	**4.329E-02**	4.077E-03	5.960E-08
F22	5.960E-08	1.565E-04	5.960E-08	1.943E-05	1.565E-04	1.943E-05	5.960E-08	1.565E-04	5.960E-08	5.960E-08
F23	5.960E-08	1.550E-06	5.960E-08	1.550E-06	5.960E-08	1.550E-06	5.960E-08	1.550E-06	5.960E-08	5.960E-08
F24(CEC14-F23)	**1**	5.960E-08	**1**	5.960E-08	5.960E-08	5.960E-08	**1**	5.960E-08	5.960E-08	5.960E-08
F25(CEC14-F24)	**5.000E-01**	5.960E-08	7.629E-06	5.960E-08	5.960E-08	5.960E-08	**1**	5.960E-08	5.960E-08	5.960E-08
F26(CEC14-F25)	**1**	5.960E-08	**1**	5.960E-08	5.960E-08	5.960E-08	**1**	5.960E-08	5.960E-08	5.960E-08
F27(CEC14-F26)	**0.690038**	**1.078E-01**	1.565E-04	4.329E-02	5.960E-08	**1.078E-01**	4.077E-03	**1**	**1.078E-01**	5.960E-08
F28(CEC14-F27)	**1**	5.960E-08	**1**	5.960E-08	5.960E-08	5.960E-08	**1**	5.960E-08	5.960E-08	5.960E-08
F29(CEC14-F28)	**1**	5.960E-08	**1**	5.960E-08	5.960E-08	5.960E-08	**1**	5.960E-08	5.960E-08	5.960E-08
F30(CEC14-F29)	1.563E-02	5.960E-08	**2.500E-01**	5.960E-08	5.960E-08	5.960E-08	4.883E-04	5.960E-08	5.960E-08	5.960E-08
F31(CEC14-F30)	7.286E-04	9.105E-04	4.181E-03	9.105E-04	5.960E-08	9.105E-04	2.213E-04	9.105E-04	1.565E-04	5.960E-08

Table 9
Friedman's mean rank.

	OAVOA	AVOA	EO	HHO	TLBO	GSA	DE	TAVOA	IGWO	BLPSO	HGWOP
Friedman's mean rank	**4.133**	4.299	5.241	5.522	4.914	8.274	7.224	4.160	6.188	6.688	9.355
Rank	**1**	3	5	6	4	10	9	2	7	8	11

$$G_i^{t+1} = \begin{cases} Aggregation\,behavior, & r_8 \geq p_3 \\ Attack\,Behaviour, & r_8 < p_3 \end{cases} = \begin{cases} \dfrac{\left(S_{i1}^t + S_{i2}^t\right)}{2}, & r_8 \geq p_3 \\ V^t - \left|d_i^t\right| \times F_i^t \times Levy(dim), & r_8 < p_3 \end{cases} \tag{19}$$

where S_{i1}^t, S_{i2}^t and $Levy(dim)$ are defined as given below

$$S_{i1}^t = Best\ Vulture^t - \frac{Best\ Vulture^t \times G_i^t}{Best\ Vulture^t - \left(G_i^t\right)^2} \times F^t \tag{20}$$

$$S_{i2}^t = Second\ best\ Vulture^t - \frac{Second\ best\ Vulture^t \times G_i^t}{Second\ best\ Vulture^t - \left(G_i^t\right)^2} \times F^t \tag{21}$$

$$Levy(dim) = 0.01 \times \frac{r_9 \times \sigma}{|r_{10}|^{\frac{1}{\beta}}} \tag{22}$$

where r_9 and r_{10} are random numbers generated uniformly in the range [0, 1], β is a constant quantity, usually taken as 1.5. The term σ is calculated from the formula given in Eq. (23).

$$\sigma = \left(\frac{\Gamma(1+\beta) \times sin\left(\frac{\pi\beta}{2}\right)}{\Gamma\left(\frac{1+\beta}{2}\right) \times \beta \times 2^{\left(\frac{\beta-1}{2}\right)}} \right)^{\frac{1}{\beta}}, \text{where } \Gamma(x) = (x-1)! \tag{23}$$

3.3. Opposition based learning

In the past few years, opposition-based learning (OBL) [33] is being integrated with most of machine intelligence algorithms to enhance its performance [71]. The opposition concept is based on the fact that a combined search of random direction with its opposite at the same time offers a higher chance of reaching the optimal point in the search space. One of the common problems in optimization algorithms is falling in local optima after getting exhausted, when the space containing the optimal solutions is far apart from the random one. In such cases, the inclusion of opposite solutions G^{opp} calculated in the reverse direction of current solutions G in the population can overcome the complication in the algorithm.

Let's consider a point X in dim-dimensional search given below

$$G = \left[g_1, g_2, g_3, \dots g_{dim}\right] \tag{24}$$

where g_j is a real number bounded in between the lower bound lb_j and upper bound ub_j for $j \in \{1, 2, 3 \dots dim\}$.The opposition number for the above point G in j^{th} dimension is defined as

$$G_j^{opp} = lb_j + ub_j - G_j \tag{25}$$

where $j \in \{1, 2, 3 \dots dim\}$.

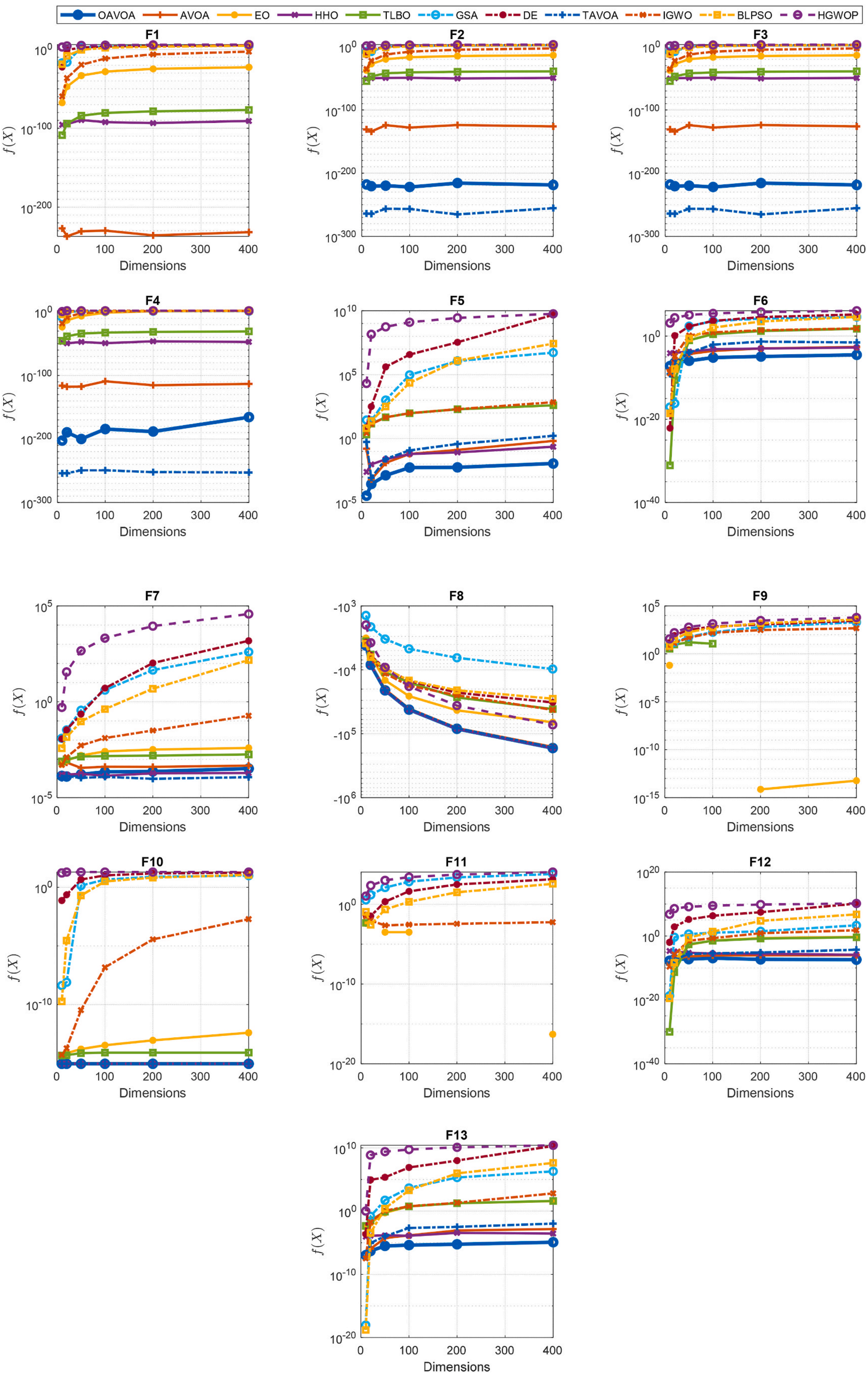

Fig. 12. Scalability plot of scalable functions $f_1 - f_{13}$

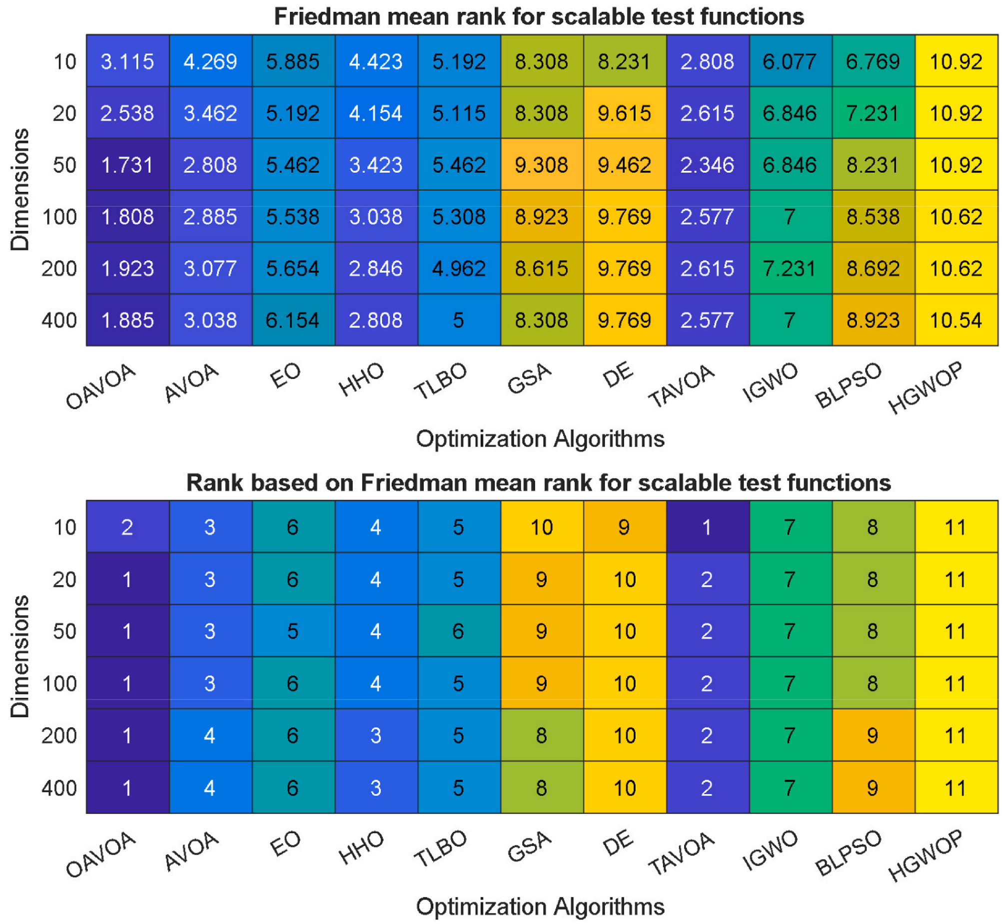

Fig. 13. Friedman's mean rank based on the scalability results obtained from performance comparisons on scalable unimodal and multimodal benchmark functions F1–F13.

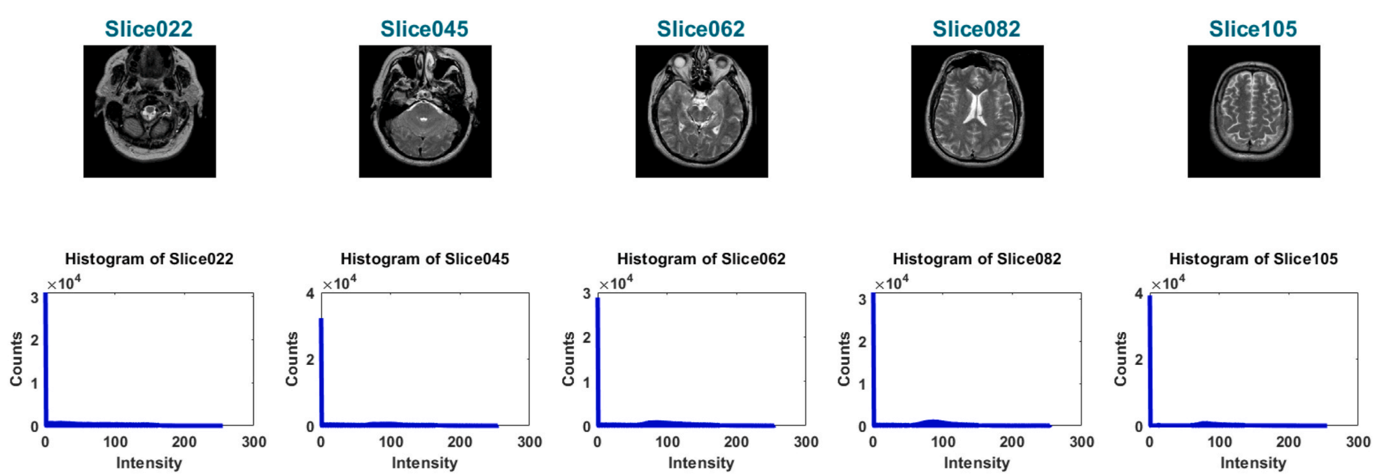

Fig. 14. The sample Brain MR images and their corresponding histograms.

4. The proposed methodology

4.1. *The proposed opposition african vulture optimization algorithm (OAVOA)*

The African vulture optimization algorithm's (AVOA) design has three shortcomings, even though it considers the balancing of exploration and exploitation skills. Firstly, while exploitation has been incorporated as a specific technique to accelerate the rate of convergence in the initial exploration process, it has an impact on the individual's global search in the solution space. Therefore, the AVOA eventually traps into a locally optimal solution without a more extensive global search. Secondly, during the exploration step, the AVOA only considers the population's best two individual pieces of information, disregarding any current knowledge about the individuals. As a result, AVOA's early convergence speed becomes poor. Thirdly, in the later stages of AVOA's exploitation, it is assumed that the first- and second-best solutions have the same impact on other people. However, this assumption fails to account for AVOA's exploration and considered abilities, resulting in a lack of exploration and exploitation in the latter stages.

No algorithm is perfect and there is always the possibility of improving the search performance. This is stated by the "no free lunch" (NFL) [72] principle. In this context, the authors propose an Opposition African Vulture Optimization Algorithm (OAVOA). The principle of additional reconstruction to progress the search process is handled differently in our algorithm.

4.1.1. The pseudocode of OAVOA

Specify the number of vultures N, the problem's dimension dim, the boundary limits are $[lb, ub]$, the random parameters $(L_1, L_2, \omega, p_1, p_2 \ and \ p_3)$ and the maximum allowable iteration T to reach the optimal position

Algorithm-1. : OAVOA pseudocode

```
Algorithm-1: OAVOA pseudocode

Input: The population Matrix G containing N vultures G_i, i ∈ {1, 2, ... N}, and each having dimension dim
Output: The optimal location of the vulture and its fitness value
Initialization: Initialize the population matrix G and set the iteration t = 1
while (t ≤ T)
Calculate the fitness value of each vulture in G_i
Obtain the best and second-best vulture according to the fitness value
for (i = 1: N)
        Select the leader V^t among the two best using Eq. (9)
        Update the hunger degree factor F^t using Eq. (11)
   if (|F^t| ≥ 1) then
                Update the Vulture location with help of p_1 using Eq. (13)
   else
        if (|F^t| ≥ 0.5) then
                Update the Vulture location with help of p_2 using Eq. (15)
        else
                Update the Vulture location with help of p_3 using Eq. (19)
        end if
   end if
 end for
Update the solutions using gaussian mutation Eq. (26)
Apply Eq. (25) to generate the opposite-solution vectors G^opp
Evaluate the fitness of the population G and G^opp
Select best solutions for the next iteration using Eq. (27)
t = t + 1,
end while
Return the best Vulture
```

Before the application of the opposition strategy, the proposed algorithm used a gaussian mutation strategy which helps the population to escape from the local optima. In this stage, a vulture in the population is randomly selected and moved to a new location with a chance of 30% using Eq. (26).

$$G_i^{t+1} = \begin{cases} G_i^{t+1}.(\mu + \sigma_s.randn(0,1)), for \ r_{11} \le 0.3 \\ G_i^{t+1}, for \ r_{11} > 0.3 \end{cases} \tag{26}$$

Here in Eq. (26), the r_{11} is random in nature which varies within $[0,1]$. Note that $randn(0,1)$ denotes the random number taken from the standard normal distribution having mean zero and standard deviation of unity. Here, μ and σ_s are the normal distribution's mean and standard deviation, respectively.

Further, to explore maximum regions in the search space and reach an optimal solution in a considerable time, an opposition-based strategy is adopted. Here, it never misses out the reverse searching process. This is applied to the solution available in the population after the completion of the Gaussian mutation. Lastly, the OAVOA selection-based updating rule is stated as follows:

$$G_i^{t+1} = \begin{cases} G_i^{t+1,opp}, for \quad fitness\left(G_i^{t+1,opp}\right) \le f\left(G_i^{t+1}\right) \\ G_i^{t+1}, for \quad fitness\left(G_i^{t+1,opp}\right) > f\left(G_i^{t+1}\right) \end{cases} \tag{27}$$

where $fitness(\bullet)$ represents the fitness value for a solution $(\bullet)$, $G_i^{t+1,opp}$ is the solution obtained using an opposition-based learning strategy as discussed in Section 3.3.

4.2. Proposed multilevel image segmentation model based on the OAVOA

In the proposed image segmentation methodology, a new multilevel thresholding approach is adopted which used a new minimum generalized cross-entropy (MGCE) to evaluate the similarity between original and segmented image. A detail description of the MGCE based multilevel thresholding and role of Opposition African Vulture Optimization Algorithm (OAVOA) algorithm to obtained optimal thresholds are discussed in following sub-sections.

4.2.1. Minimum generalized cross-entropy (MGCE) based thresholding

In this section, our key contribution idea is discussed. The idea of Cross Entropy (CE) was first introduced by Kullback [73] to estimate the conceptual information gap between two distributions. In both the object and background sections, minimization of the cross entropy compels the overall intensity in the thresholded image, to be like that of the actual input image. The lesser the cross entropy, the more alike the distributions of two variables are, and vice versa. Kullback-Leibler number, discrimination information, directed divergence, and relative entropy are all terms, alternatively used to describe cross-entropy. In the article [74,75], the authors used the minimum cross entropy (MCE) thresholding to generate the segmented image by minimizing the divergence between the input and output segmented images. The cross-entropy calculated in this case is the sum of the divergence between the foreground and background probability distributions of the input and output image pixels. Though the MCE based thresholding is a popular and efficient method of segmentation, it performs poorly in

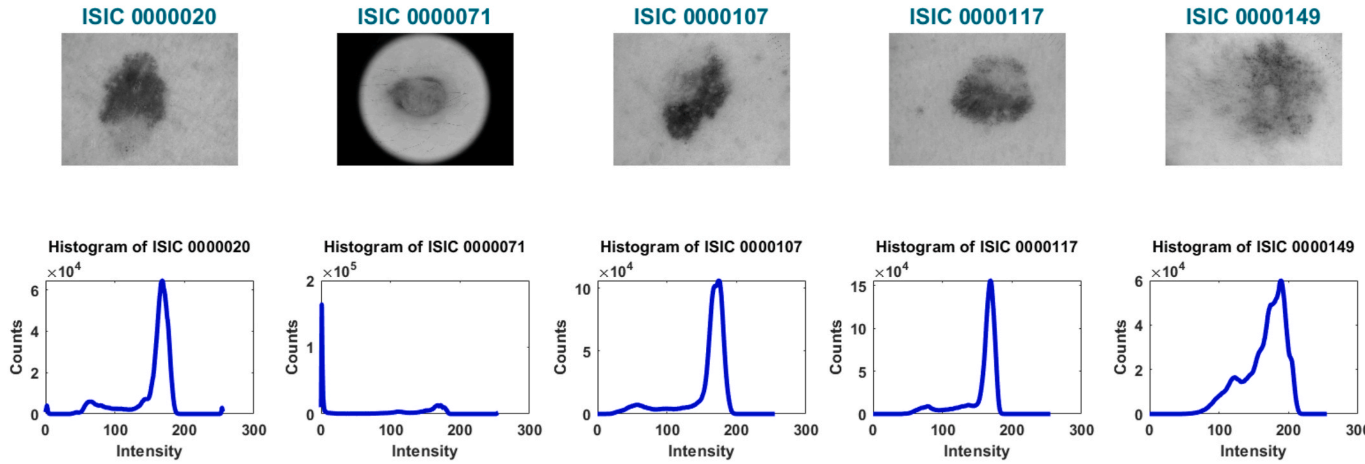

Fig. 15. The sample dermoscopic skin lesion image and their corresponding histograms.

some cases, because of ignoring the degree of divergence. Further, the maximum entropy and minimum cross entropy yield the same result while dealing with uniform distribution of pixel intensities.

To overcome this issue, the authors of this paper incorporate the degree of divergence as discussed earlier to present a better approach for computing the cross entropy, referred to as minimum generalized cross-entropy (MGCE) for multilevel thresholding application. The optimal thresholds are computed by minimizing the MGCE between the original input image and constructed thresholded output images.

Let $\{th_1, th_2, th_3 \ldots th_k\}$ are set of threshold values for splitting the input image to $k+1$ distinct regions $\{Rg_1, Rg_2, \ldots Rg_{k+1}\}$. The objective function (OF) derived from the minimum generalized cross-entropy is now expressed as

$$OF_{MGCE}(th_1, th_2, th_3 \ldots th_k) = \left[\sum_{i=0}^{th_1}\left(i.h_i.log\left({}^{i}/_{\mu_1}\right)\right)^p\right]^{\frac{1}{p}} + \left[\sum_{i=th_1}^{th_2}\left(i.h_i.log\left({}^{i}/_{\mu_2}\right)\right)^p\right]^{\frac{1}{p}} + \ldots + \left[\sum_{i=th_k}^{L-1}\left(i.h_i.log\left({}^{i}/_{\mu_{k+1}}\right)\right)^p\right]^{\frac{1}{p}} \tag{28}$$

where the degree of divergence p is defined in the range $0 \leq p \leq \infty$ and

$$\mu_i = \sum_{i=th_{i-1}}^{th_i} i.h_i \Big/ \sum_{i=th_{i-1}}^{th_i} h_i \tag{29}$$

To obtain the optimal thresholds, the above entropy function needs to be minimized, i.e.,

$$\left(th_1^*, th_2^*, th_3^* \ldots th_k^*\right) = \underset{th_1 < th_2 < th_3 \ldots < th_k}{arg\ min} \left[OF_{MGCE}(th_1, th_2, th_3 \ldots th_k)\right] \tag{30}$$

where $th_1^*, th_2^*, th_3^* \ldots th_k^*$ denote optimal threshold values.

The entropy-based multilevel thresholding algorithm's computation cost rises exponentially with an increase in threshold values. To address the issue, meta-heuristic optimization, and searching methods have been utilized by many researchers to obtain the best solutions in image multilevel thresholding. In this paper, an opposition African vulture optimization algorithm (OAVOA) is used to accelerate the searching process of optimal threshold selections.

4.2.2. OAVOA-MGCE based optimal multilevel thresholding for medical image segmentation

Here, a Minimum generalized cross-entropy (MGCE) based multilevel threshold selection using the newly introduced opposition African vulture optimization algorithm (OAVOA) is discussed. An effort is made to provide the desired multilevel thresholded medical images which will be helpful for proper diagnosis. To perform multilevel thresholding, we have used the MGCE as the objective function which needs to be minimized for obtaining the optimal thresholds. As minimization of MGCE is an optimization problem, we have used the OAVOA algorithm, because of its excellent optimization ability discussed in the preceding sections. The looking for the best threshold vector begins with a random generation of the OAVOA algorithm's initial African vulture population. A feasible solution to a threshold vector is represented by each vulture G_i in the population. Each vulture ascertains their location utilizing the place appraises rule outlined in the preliminary part of this paper. During each iteration, the current fitness value is compared to that of the best location achieved so far. Accordingly, the current best is updated, provided this value is less than the previous one. This process is continued till the stopping criteria are met. Once the stopping criteria are satisfied, the optimum threshold vectors corresponding to the best vulture are obtained. These are further applied to the image for generating a thresholded image. For the creation of the output thresholded images, the following construction rule is used. In the case of three-level thresholding having a threshold vector $[th_1, th_2]$, pixel intensities (less than or equal to th_1) are substituted by the average intensity value of all pixels. In the same way, pixel values in the ranges $[th_1, th_2]$ and $[th_2, L-1]$ are set to a value equal to the average pixel intensities in the respective range, where $L-1$ is the maximum possible intensity value.

Once the thresholded image of the test image is available, the desired region can be analyzed by the physician separately for diagnosis. The framework of the proposed multilevel thresholding method is depicted in Fig. 1 as a flowchart.

5. Experimental results and discussion

The suggested MGCE based multilevel segmentation technique using OAVOA has been evaluated using MRI and dermoscopic images. The primary task for any non-parametric multilevel thresholding approach is the selection of a suitable optimization algorithm. To investigate the

Table 10
Average PSNR, SSIM, and FSIM values obtained by different entropy-based thresholding for Brain MRI images.

	k	OAVOA-MGCE			OAVOA-MCE			OAVOA-Kaniadakis			OAVOA-Masi		
		PSNR	SSIM	FSIM	PSNR	SSIM	FSIM	PSNR	SSIM	FSIM	PSNR	SSIM	FSIM
Slice022	2	24.7596	0.7449	0.6941	24.0792	0.4702	0.6852	19.7751	0.2691	0.5583	19.1232	0.2509	0.5627
	3	27.5596	0.8567	0.8017	27.0298	0.6436	0.7741	23.5536	0.3957	0.6744	23.2171	0.3844	0.6680
	4	29.4057	0.9023	0.8656	29.0161	0.7573	0.8428	25.9696	0.4837	0.7667	25.1207	0.4507	0.7448
	5	30.9039	0.9273	0.9025	30.5311	0.8760	0.8859	26.6377	0.5046	0.7835	25.7323	0.4703	0.7650
Slice045	2	24.1058	0.6743	0.7482	23.3876	0.5117	0.7429	16.8287	0.2655	0.5950	16.8927	0.2674	0.5962
	3	26.1053	0.8690	0.8226	25.6662	0.6409	0.8079	19.4539	0.3333	0.6796	18.1416	0.3036	0.6558
	4	27.9098	0.9027	0.8632	27.4173	0.8055	0.8546	27.2367	0.6412	0.8406	21.2739	0.3856	0.7301
	5	29.8519	0.9231	0.8984	28.8719	0.8716	0.8934	29.0148	0.7475	0.8827	28.2484	0.6590	0.8603
Slice062	2	23.5642	0.7368	0.6803	22.7117	0.5286	0.6707	16.1878	0.2879	0.5540	16.2394	0.2897	0.5564
	3	25.7445	0.8066	0.7721	25.1478	0.6729	0.7777	17.8890	0.3486	0.6426	17.9072	0.3486	0.6424
	4	27.3938	0.8839	0.8305	26.8700	0.7459	0.8142	19.1733	0.3837	0.6898	19.2785	0.3851	0.6905
	5	29.1939	0.9159	0.8681	28.4661	0.8608	0.8664	28.0626	0.8079	0.8402	28.2410	0.7434	0.8372
Slice082	2	23.6651	0.7493	0.7131	22.7508	0.5696	0.6902	16.4910	0.2798	0.5883	16.5755	0.2813	0.5898
	3	25.9230	0.8198	0.7713	24.4538	0.7053	0.7668	17.2868	0.3048	0.6431	17.3631	0.3060	0.6447
	4	27.9684	0.8856	0.8319	27.0335	0.8405	0.8119	18.5900	0.3568	0.6794	18.1355	0.3239	0.6754
	5	29.8130	0.9182	0.8739	29.5321	0.9088	0.8613	27.7940	0.8142	0.8190	28.9143	0.8322	0.8262
Slice105	2	25.6857	0.8546	0.8219	24.4461	0.6582	0.7990	17.4865	0.2070	0.7547	17.1341	0.1972	0.7460
	3	27.8836	0.8934	0.8779	26.7389	0.8365	0.8441	19.0681	0.2451	0.7945	18.6109	0.2353	0.7851
	4	29.8494	0.9280	0.9138	29.3938	0.8574	0.8961	26.8863	0.7438	0.8596	19.4102	0.2537	0.8053
	5	31.7299	0.9480	0.9415	31.0563	0.9516	0.9293	30.4114	0.9124	0.9119	30.9522	0.9391	0.9229
		OAVOA-Tsallis			**OAVOA-Reniys**			**OAVOA-Kapurs**			**OAVOA-Shannon**		
		PSNR	**SSIM**	**FSIM**	**PSNR**	**SSIM**	**FSIM**	**PSNR**	**SSIM**	**FSIM**	**PSNR**	**SSIM**	**FSIM**
Slice022	2	20.4489	0.2897	0.5665	20.4379	0.2894	0.5664	19.7620	0.2687	0.5581	19.8372	0.2710	0.5580
	3	23.6779	0.3992	0.6771	23.6760	0.3991	0.6773	23.8507	0.4063	0.6799	23.7837	0.4041	0.6782
	4	25.3544	0.4617	0.7492	25.4758	0.4667	0.7525	26.1032	0.4902	0.7702	25.8354	0.4850	0.7629
	5	26.9647	0.5188	0.7946	26.9808	0.5218	0.7969	26.6325	0.5108	0.7846	26.3620	0.4979	0.7787
Slice045	2	19.3537	0.3224	0.6249	19.3848	0.3233	0.6252	16.9565	0.2693	0.5948	16.8890	0.2671	0.5942
	3	24.1409	0.4583	0.7500	24.0697	0.4552	0.7480	20.6356	0.3626	0.6998	19.5302	0.3359	0.6798
	4	26.0972	0.5391	0.8123	26.0302	0.5349	0.8111	27.3509	0.6679	0.8439	26.6706	0.6134	0.8282
	5	27.6235	0.5985	0.8478	27.6569	0.6069	0.8475	29.2329	0.7698	0.8880	28.8280	0.7428	0.8782
Slice062	2	18.7901	0.3401	0.5872	18.7926	0.3402	0.5875	16.1578	0.2870	0.5531	16.0914	0.2855	0.5531
	3	23.4449	0.4525	0.6934	23.3249	0.4480	0.6913	18.1040	0.3533	0.6479	17.7756	0.3457	0.6388
	4	26.1546	0.5555	0.7726	26.1775	0.5597	0.7728	19.2963	0.3864	0.6923	18.9667	0.3795	0.6853
	5	27.8117	0.6595	0.8313	27.7502	0.6456	0.8293	28.6264	0.8460	0.8495	27.9523	0.7962	0.8383
Slice082	2	18.2736	0.2983	0.5831	18.2553	0.2983	0.5838	16.5193	0.2803	0.5887	16.4348	0.2787	0.5872
	3	23.7294	0.4271	0.6962	23.7608	0.4275	0.6967	17.2469	0.3042	0.6424	17.1189	0.3019	0.6381
	4	26.6655	0.5586	0.7696	26.6147	0.5575	0.7684	19.3193	0.3951	0.6895	18.4350	0.3532	0.6730
	5	28.3635	0.6662	0.8329	28.3736	0.6604	0.8327	29.1065	0.8767	0.8352	26.1783	0.7112	0.7941
Slice105	2	19.2864	0.2361	0.7627	19.2990	0.2361	0.7622	17.5308	0.2083	0.7553	17.7539	0.2135	0.7588
	3	24.7390	0.4168	0.8344	24.7296	0.4176	0.8339	19.1347	0.2466	0.7962	19.0119	0.2442	0.7937
	4	27.8289	0.5805	0.8815	27.7838	0.5798	0.8811	26.8449	0.6722	0.8561	25.6322	0.7274	0.8546
	5	29.2080	0.7104	0.9138	29.2879	0.7106	0.9147	30.1982	0.8955	0.9089	30.5853	0.9358	0.9175

effectiveness of the OAVOA algorithm, this section first discusses an experimental study of the proposed algorithm on various types of benchmark functions. As the essence of the proposed method is to multilevel segmentation of Brain MRI and dermoscopic images, a performance evaluation the proposed OAVOA-MGCE based multilevel thresholding is discussed in the second part of the section.

5.1. Experimental verification of OAVOA

In this part, we examine the OAVOA's performance using 23 numbers of well-known benchmark test functions [76]. Eight popular composite functions from CEC 2014 test suite [76] are also examined because they are made up of basic and hybrid functions and ideal for evaluating the potential performance of algorithms. It is noteworthy to mention here that all 31 benchmark functions are divided into four groups: unimodal test functions (F1–F7), scalable multimodal test functions (F8–F13), fixed multimodal test functions (F14–F23), and composition test functions (F24 (CEC14-F23) - F31 (CEC14-F30)). The exploitation ability is demonstrated by unimodal test functions, whereas the exploration ability is demonstrated by multimodal test functions,

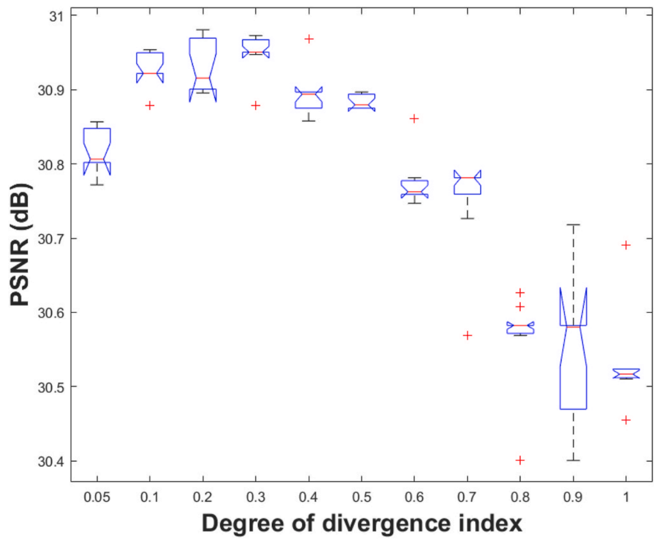

Fig. 16. Effect of degree of divergence on segmentation of Brain MRI image (Slice022).

which avoid several local minima in its path to arrive at the global minimum. Note that the CEC2014 benchmark functions have a lot of local minima and various shapes in different regions of the search space. Interestingly, all unimodal and multimodal functions have been shifted, rotated, hybridized, and enlarged to create these functions. The results of an algorithm, when applied to these composite functions, decide how far it is suitable to handle a real-time complex optimization problem.

The OAVOA's performance is compared to optimization techniques that are well-known and have recently been developed. These include – the African vultures optimization algorithm (AVOA) [29], Equilibrium optimizer (EO) [28], Harris hawks optimization (HHO) [27], Teaching–learning-based optimization (TLBO) [20], Gravitational Search Algorithm (GSA) [36], Differential Evolution (DE) [24]. Time-varying mechanism based African vulture optimization algorithm (TAVOA) [32], Biogeography-based learning particle swarm optimization (BLPSO) [48], Improved grey wolf optimizer (IGWO) [47] and Hybrid particle Swarm and grey wolf optimizer (HGWOP) [55]. The average ('Avg'), best, median and worst results along with standard deviation ('std') are computed for statistical analysis. These metrics are acquired through 25 independent trials. These values are reported below. For validation, the Boxplots, convergence curves, and scalability curves are also presented. These plots are used to compare the OAVOA's performances with the other optimization techniques on a quantitative level. Furthermore, the substantial differences between the other optimization techniques are demonstrated using Friedman's mean-rank test. The profound differences are observed while considering Wilcoxon signed-rank test. We achieved a degree of significance on the order of 5%. The Wilcoxon signed-rank test is utilized for comparing the p-value of OAVOA vs. earlier optimizers. Here, we consider 25 self-governing optimal results, assigning a ' + ' for a *p*-value which is more than 5% degree of significance, a ' − ' for a *p*-value which is quite smaller than 5% degree of significance, and a " for a p-value with zero momentous difference. All test functions are assessed with a population size of 30 with 500 iterations, to get a reasonable comparison. The list of the control parameters is presented in Table 3. These are used for the implementation. The optimization algorithms are run in MATLAB R2018 on an operating system of Windows 10 with an Intel Core i3 processor and RAM capacity of 8 GB.

5.1.1. *Qualitative analysis (search history, trajectory, and convergence curve) of OAVOA*

The qualitative analysis of the proposed OAVOA algorithm is comprised of search history, overall trajectory and convergence curve of various unimodal, multimodal and composite test functions shown in Figs. 2 and 3. Even though that these functions have large dimensions, the 2D representations of the functions reveal information on the topology of the domain. The locations that vultures visited over the course of iterations are shown in the search history map. The trajectory diagram keeps track of changes in the first vulture's in different dimensions as the process progresses. Additionally, the convergence metric shows how the fitness value of the vulture changes throughout the course of optimization.

According to the search history data, the vultures in unimodal functions tend to congregate around the optimal point more successfully than in multimodal and composite functions. This move by OAVOA reveals its capacity for exploitation. However, the proper dispersion of particles in the search space of multimodal and composition functions demonstrates the exploratory potential of OAVOA's algorithm. From the trajectory map, it is clear that during the initial generation, the vulture positions have a wide range that spans the whole search space; however, as optimization moves forward, the vulture positions start to converge to the solution space by adopting an oscillatory behaviour in some cases. It is evident that the fluctuations are associated with the complexity of the domain. More variations happen in a more complicated domain. After several repetitions, there are no fluctuations in unimodal functions. In most of the cases of multimodal and composite functions, variations are more pronounced, occur more frequently, and last for more iterations. This behaviour shows that careful exploitation and exploration are advantageous to OAVOA. It can be seen from the convergence curve that, there is an accelerated decline pattern in all of the curves depicted in the last column of Figs. 2 and 3, especially after the competition of almost half of the iterations for the complex functions. A careful observation can also reveal that when the OAVOA is expected to move from the exploration stage to exploitation stage. It has been noted that the OAVOA can show a trend of faster and desired convergence property.

5.1.2. *OAVOA's performance on unimodal test functions*

Table 4 shows the comparison findings for the test functions (F1–F7). Test functions are assessed for *dim* = 30. It can be observed that the results of OAVOA for unimodal test functions (F1–F4) are much better than those of other optimization algorithms. For the test function F5, the OAVOA performs better than others with a marginal improvement over AVOA and HHO. Though GSA can move close to the optimal solution for the function F_6, but not consistent with it. Whereas the lowest average value of OAVOA for the test function F_6 with minimum standard deviation makes it more reliable than GSA. A close competition between OAVOA and AVOA can be seen in function F_7. Except for the best value, OAVOA dominates the AVOA in all aspects and is again found better. Even though chaotic mapping and the time-varying technique improve TAVOA over AVOA, it can only outperform OAVOA for the test functions F2 and F4. The boxplots are displayed in Fig. 4 to help readers understand the distribution of findings. The Boxplots depict the optimization algorithm's potential. These charts can be used to determine how frequently or consistently the optimal solutions are found. In Fig. 4, boxplots of 4 test functions (F1, F3, F5, and F7) for fitness value utilizing the best solutions obtained during 25 independent runs are shown. Surprisingly, among all optimization techniques, the OAVOA has produced satisfactory results. It's also crucial to maintain track of an algorithm's convergence. Convergence graphs show how an algorithm improves over time, which is useful for determining how well an algorithm is or which algorithm performs better. Based on the iteration count, a comparison of the OAVOA with various optimization methods (for 4 test functions) is provided in Fig. 5. The OAVOA 's performance of unimodal test functions is significantly better than other strategies except F2 and F4, where TAVOA dominates, as shown in figure.

5.1.3. *The OAVOA's performance on scalable multimodal test functions*

The performance related to multimodal functions (F8–F13), which

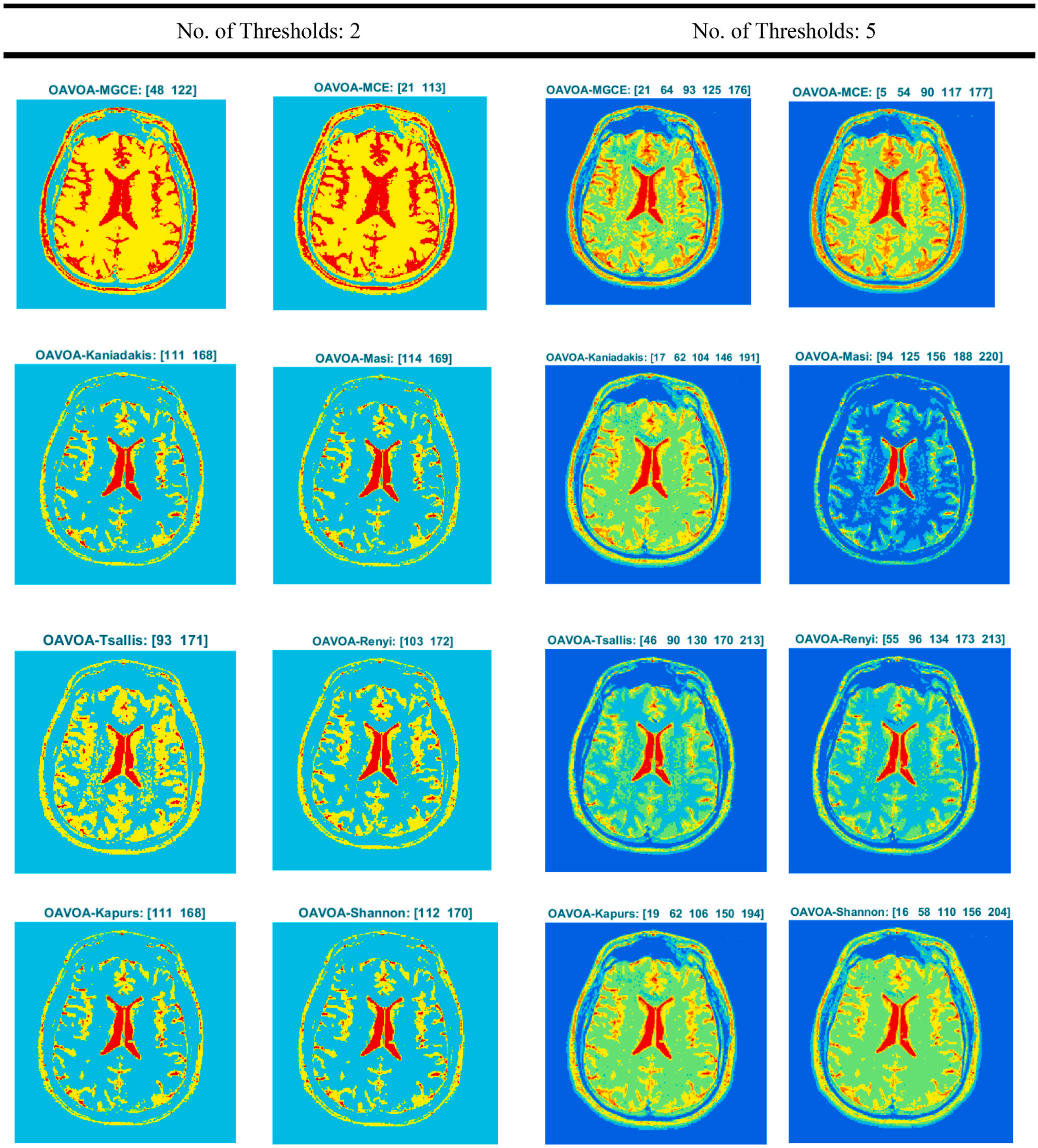

Fig. 17. Thresholded images of Brain MR image (Slice 082) for $k = 2$ *and* 5

have several optimal solutions with scalable dimensions, is discussed in this section. The obtained results of these functions are presented in Table 5. It is observed that the OAVOA dominates once again for all cases except F8. It has a very close completion with HHO concerning the average value, but can achieve the best fitness same as the HHO. The consistency of the OAVOA is also found impressive from the Boxplots (of four test functions) shown in Fig. 6. The remarkable convergence behavior of the OAVOA in the convergence plot presented in Fig. 7 reveals its excellent exploration, skill in reaching the desired solution in a limited time.

5.1.4. The OAVOA's performance on fixed dimension multimodal test functions

The section reveals the proposed optimization algorithm's diversification as well as the local optimal escape potentials after applying to multimodal functions having fixed dimensions. Table 6 displays the obtained results, which show that the proposed method has a satisfactory performance in minimizing these test functions. For the test function F14, though the proposed algorithm can reach the optimal solution, but stands in second place in the comparison table for the average value. For the test function F15, the IGWO algorithm dominates all in most of the performance measures. Whereas, for the remaining test functions,

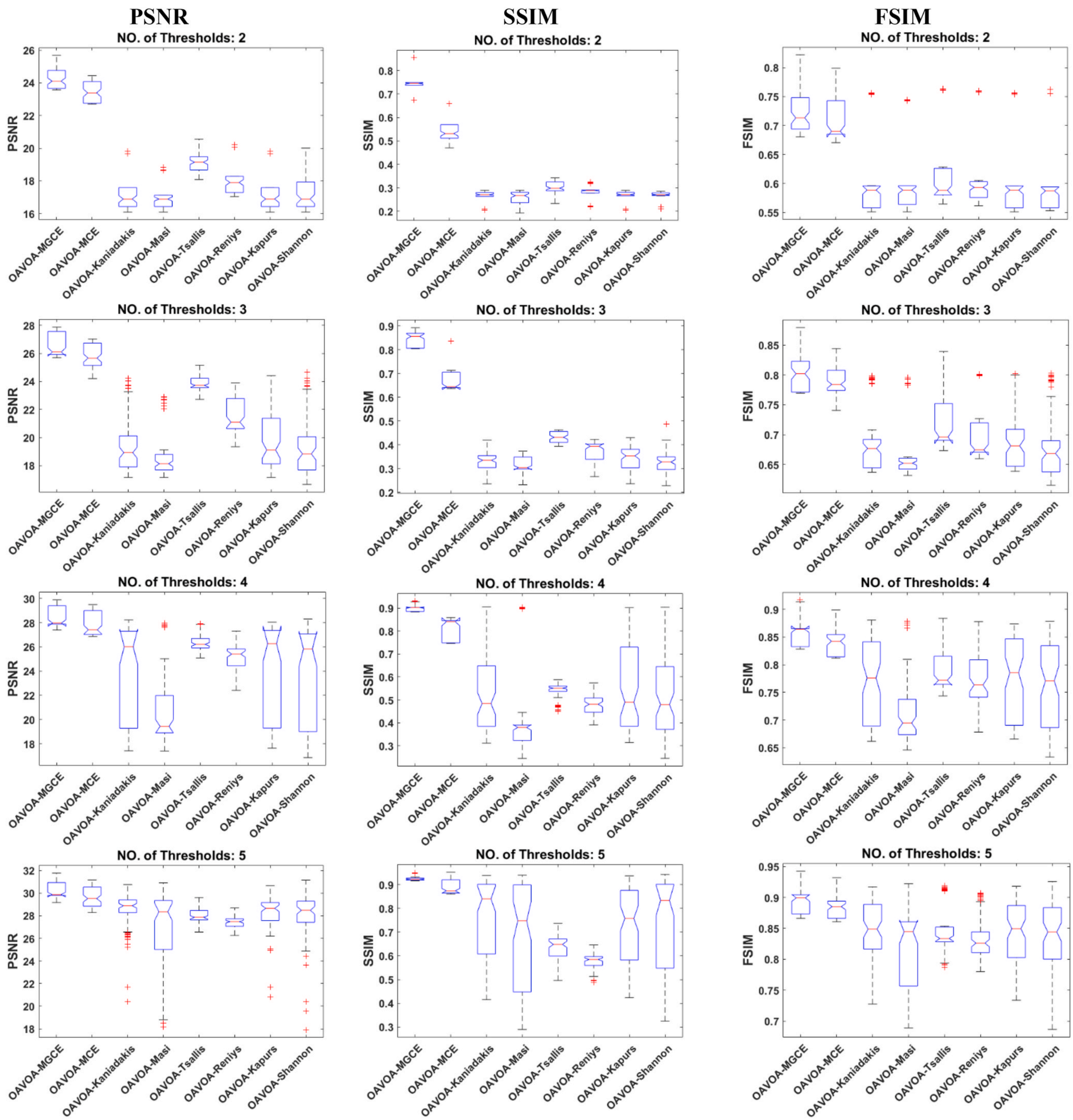

Fig. 18. ANOVA test result of different entropy-based thresholding methods on five test Brain MR images.

Table 11
Wilcoxon's test for comparison of proposed OAVOA-MGCE based multilevel thresholding with other entropy-based thresholding based on PSNR, SSIM, and FSIM on Brain MR images.

		PSNR		SSIM		FSIM	
	k	p-value	win	p-value	win	p-value	win
MGCE vs MCE	2	5.29E-23	(+)	5.29E-23	(−)	5.29E-23	(+)
	3	5.29E-23	(+)	5.29E-23	(+)	0.002444	(+)
	4	5.29E-23	(+)	5.29E-23	(+)	5.29E-23	(+)
	5	5.29E-23	(+)	0.00108	(+)	1.51E-19	(+)
MGCE vs Kaniadakis	2	5.29E-23	(+)	5.29E-23	(+)	5.29E-23	(+)
	3	5.29E-23	(+)	5.29E-23	(+)	5.29E-23	(+)
	4	5.29E-23	(+)	8.40E-09	(+)	5.29E-23	(+)
	5	5.29E-23	(+)	1.16E-14	(+)	5.29E-23	(+)
MGCE vs Masi	2	5.29E-23	(+)	5.29E-23	(+)	5.29E-23	(+)
	3	5.29E-23	(+)	5.29E-23	(+)	5.29E-23	(+)
	4	5.29E-23	(+)	1.16E-14	(+)	5.29E-23	(+)
	5	5.29E-23	(+)	3.73E-18	(+)	5.29E-23	(+)
MGCE Vs Tsallis	2	5.29E-23	(+)	5.29E-23	(+)	5.29E-23	(+)
	3	5.29E-23	(+)	5.29E-23	(+)	5.29E-23	(+)
	4	5.29E-23	(+)	5.29E-23	(+)	5.29E-23	(+)
	5	5.29E-23	(+)	5.29E-23	(+)	5.29E-23	(+)
MGCE vs Reniys	2	5.29E-23	(+)	5.29E-23	(+)	5.29E-23	(+)
	3	5.29E-23	(+)	5.29E-23	(+)	5.29E-23	(+)
	4	5.29E-23	(+)	5.29E-23	(+)	5.29E-23	(+)
	5	5.29E-23	(+)	5.29E-23	(+)	5.29E-23	(+)
MGCE vs Kapurs	2	5.29E-23	(+)	5.29E-23	(+)	5.29E-23	(+)
	3	5.29E-23	(+)	5.29E-23	(+)	5.29E-23	(+)
	4	5.29E-23	(+)	1.69E-09	(+)	5.29E-23	(+)
	5	5.29E-23	(+)	1.16E-14	(+)	5.29E-23	(+)
MGCE vs Shannon	2	5.29E-23	(+)	5.29E-23	(+)	5.29E-23	(+)
	3	5.29E-23	(+)	5.29E-23	(+)	5.29E-23	(+)
	4	5.29E-23	(+)	3.81E-08	(+)	5.29E-23	(+)
	5	5.29E-23	(+)	1.16E-14	(+)	5.29E-23	(+)

OAVOA performance is quite noticeable. It only lags with the nearest competitors by a very little margin for standard deviations. The steadiness is observed in the box plot shown in Fig. 8 for the test functions F15, F20, F21, and F23. The result reveals that there is a remarkable improvement over AVOA for the test function F20 while acceptable performance for the remaining cases. Fig. 9 shows the convergence curves of four test functions. This is a curve of the finest fitness obtained so far vs. iterations count. According to the findings, the OAVOA leads others for F15 and F23. Whereas, for the test functions F20 and F21, the behavior of the OAVOA takes a little more iteration to converge due to the presence of an additional exploration stage.

5.1.5. The OAVOA's performance on composite test functions

The most difficult test cases are composite test cases. These functions are used to assess a method's capacity to avoid local minima including its exploration ability. Table 7 (F24–F31) compares the performance of OAVOA and other approaches to composition functions. As these are associated with various local minima, a pictorial illustration of the distribution of values obtained for four functions using the boxplots (for four composite functions F25, F28, F30, and F31) is provided in Fig. 10. However, the opposition-based strategy along with Gaussian mutation helps OAVOA to reach an optimal solution for all and overall found better than all. The OAVOA is also found superior for its excellent convergence speed shown in Fig. 11 (for the above four composite functions). The above tests prove that the proposed OAVOA performs the exploitation and exploration mechanism excellently while dealing with complex problems.

5.1.6. Statistical significance analysis

As a nonparametric test, the Wilcoxon Signed-Rank Test can effectively examine statistically significant differences between two optimizers. Table 8 shows the statistical findings of the Wilcoxon Signed-Rank Test for 31 benchmark functions in 25 runs with a 5% significant level ($\alpha = 0.05$) and the obtained *p*-values are listed. A count of $' = '$ sign represents that, OAVOA's performance is identical with other optimizers for *p*-values equals unity. The $' + '$ sign, which denotes the proposed algorithm, performs better than compared one with *p*-values less than 0.05. Table 6 reveals that our proposal dominates for most of the functions with a maximum count of $' + '$ sign. The $'-'$ sign indicates that the OAVOA is worse than the one being compared. To further assess the OAVOA's statistical performance, the Friedman test [50] is also conducted. Table 9 summarizes Friedman's mean-rank for all 25 independent runs of 31 test functions (F1–F31) using various optimization techniques. The Friedman statistic is based on the calculation of mean rank values. The critical values are obtained for the significance level $(\alpha = 0.05)$, then compared to Friedman statistics to decide on a rejection of the null hypothesis. From Table 8, it is explicitly clear that the null hypothesis is found rejected and the OAVOA stands at rank one.

5.1.7. Scalability analysis of OAVOA

This section uses a scalability analysis to assess the OAVOA algorithm's performance for high and low-dimensional problems. Because real-world optimization problems frequently have many parameters that need to be optimized, the proposed algorithm along with a set of algorithms for comparison are also tested with dimensions $dim = 10, 20, 50, 100, 200, 400$ as shown in Fig. 12. The number of iterations and population size is fixed at 500 and 30 respectively during the test. This test illustrates how well the method performs as the dimension of the problem grows, while the number of iterations and particles remain constant. To assess the exploration and abilities, the test is done on five test samples of unimodal and multimodal functions. Three test samples of composite test functions are also used for the testing. The following facts are extracted from the analysis:

Table 12
Average PSNR, SSIM, and FSIM values obtained by different entropy-based thresholding for Dermoscopic skin lesion image.

	k	OAVOA-MGCE			OAVOA-MCE			OAVOA-Kaniadakis			OAVOA-Masi		
		PSNR	SSIM	FSIM	PSNR	SSIM	FSIM	PSNR	SSIM	FSIM	PSNR	SSIM	FSIM
ISIC_0000020	2	28.3688	0.8309	0.7511	27.9557	0.8123	0.7552	28.1102	0.8111	0.7170	28.1102	0.8111	0.7170
	3	30.5511	0.8430	0.7936	30.2482	0.8429	0.8012	29.9908	0.8246	0.7630	30.0012	0.8238	0.7643
	4	32.5131	0.8613	0.8330	32.3559	0.8547	0.8282	30.3325	0.8291	0.7717	30.5536	0.8325	0.7794
	5	33.7790	0.8782	0.8488	33.5675	0.8766	0.8598	30.9923	0.8381	0.7930	31.0550	0.8369	0.7947
ISIC_0000071	2	26.4886	0.7876	0.7623	25.6015	0.8107	0.7278	21.9398	0.8133	0.7464	19.2304	0.4721	0.6911
	3	28.3997	0.8349	0.7795	27.3891	0.8231	0.7558	27.9561	0.8402	0.7736	28.1859	0.8427	0.7856
	4	30.7616	0.8615	0.8305	30.1766	0.8639	0.7996	29.3620	0.8527	0.8167	29.4496	0.8551	0.8278
	5	32.1361	0.8911	0.8596	31.5513	0.8699	0.8325	30.9513	0.8660	0.8551	31.0599	0.8669	0.8610
ISIC_0000107	2	27.5769	0.8673	0.7905	26.5505	0.8422	0.7871	27.6247	0.8486	0.7781	27.6247	0.8486	0.7781
	3	29.8910	0.8628	0.8208	29.7413	0.8542	0.8167	29.0469	0.8541	0.8107	29.0542	0.8539	0.8109
	4	31.6451	0.8622	0.8539	31.4163	0.8547	0.8501	29.6512	0.8608	0.8272	29.7174	0.8615	0.8293
	5	32.8765	0.8706	0.8780	32.5855	0.8634	0.8771	30.1727	0.8683	0.8472	30.2320	0.8672	0.8497
ISIC_0000117	2	30.0296	0.9117	0.8200	30.0296	0.9104	0.8099	30.0115	0.8815	0.8082	30.0115	0.8815	0.8082
	3	31.9255	0.8950	0.8428	31.7843	0.8958	0.8433	31.4089	0.8859	0.8366	31.4157	0.8862	0.8368
	4	33.7827	0.9056	0.8862	33.3703	0.8950	0.8717	32.1936	0.8939	0.8603	32.2330	0.8946	0.8614
	5	34.8323	0.9108	0.9016	34.7950	0.9023	0.9002	32.5247	0.8993	0.8701	32.7253	0.9026	0.8760
ISIC_0000149	2	27.1469	0.8084	0.7574	27.0240	0.8146	0.7468	25.6172	0.8056	0.7616	25.6689	0.8033	0.7600
	3	29.2463	0.8411	0.7912	29.0585	0.8200	0.7931	26.6421	0.8066	0.7812	26.7137	0.8049	0.7800
	4	31.0485	0.8308	0.8493	30.8524	0.8249	0.8382	28.7888	0.8133	0.8165	29.0716	0.8125	0.8186
	5	32.4832	0.8511	0.8722	32.3090	0.8297	0.8667	30.0569	0.8206	0.8413	30.3731	0.8237	0.8475
		OAVOA-Tsallis			**OAVOA-Reniys**			**OAVOA-Kapurs**			**OAVOA-Shannon**		
		PSNR	**SSIM**	**FSIM**	**PSNR**	**SSIM**	**FSIM**	**PSNR**	**SSIM**	**FSIM**	**PSNR**	**SSIM**	**FSIM**
ISIC_0000020	2	27.9661	0.8100	0.7171	28.0516	0.8097	0.7179	28.3196	0.8062	0.7372	28.3489	0.8069	0.7368
	3	29.7985	0.8185	0.7644	29.9080	0.8215	0.7652	30.0128	0.8241	0.7643	30.0132	0.8245	0.7636
	4	30.8618	0.8198	0.7868	30.5220	0.8238	0.7785	30.4873	0.8311	0.7772	30.5698	0.8320	0.7800
	5	32.0704	0.8298	0.8124	31.4215	0.8328	0.8021	31.0607	0.8376	0.7952	31.0820	0.8374	0.7958
ISIC_0000071	2	26.0322	0.7302	0.7564	25.5582	0.6962	0.7394	21.9347	0.8129	0.7457	21.9398	0.8133	0.7464
	3	28.3964	0.8159	0.8012	28.4134	0.8158	0.7997	27.9348	0.8397	0.7727	27.9386	0.8395	0.7723
	4	29.8098	0.8221	0.8329	29.6449	0.8337	0.8358	29.3888	0.8524	0.8180	29.4003	0.8527	0.8191
	5	31.5765	0.8457	0.8663	31.1231	0.8680	0.8662	30.8686	0.8656	0.8553	30.9247	0.8647	0.8551
ISIC_0000107	2	27.2783	0.8519	0.7720	27.5069	0.8506	0.7763	27.6396	0.8477	0.7781	27.6204	0.8475	0.7778
	3	28.6958	0.8511	0.8030	28.8697	0.8521	0.8069	29.0735	0.8534	0.8115	29.0890	0.8534	0.8118
	4	29.8041	0.8536	0.8324	29.6812	0.8586	0.8278	29.6774	0.8610	0.8278	29.7350	0.8609	0.8297
	5	30.7160	0.8510	0.8589	30.3810	0.8614	0.8547	30.2286	0.8672	0.8497	30.2371	0.8674	0.8500
ISIC_0000117	2	29.1270	0.8803	0.8041	29.7757	0.8856	0.8079	29.9881	0.8799	0.8078	29.9881	0.8799	0.8078
	3	30.9892	0.8873	0.8326	31.1968	0.8848	0.8333	31.4132	0.8860	0.8368	31.4310	0.8866	0.8371
	4	32.0696	0.8907	0.8570	32.0247	0.8917	0.8553	32.1957	0.8940	0.8606	32.2289	0.8946	0.8613
	5	32.8449	0.8915	0.8772	32.6323	0.8958	0.8733	32.5854	0.9006	0.8717	32.6478	0.9019	0.8737
ISIC_0000149	2	25.0262	0.8007	0.7498	24.7474	0.8060	0.7526	25.6689	0.8033	0.7600	25.6689	0.8033	0.7600
	3	27.0326	0.7936	0.7708	26.9381	0.7986	0.7744	26.6519	0.8056	0.7803	26.6973	0.8054	0.7803
	4	29.0086	0.8085	0.8089	28.9284	0.8088	0.8091	28.8360	0.8118	0.8154	29.1113	0.8127	0.8186
	5	30.3930	0.8132	0.8379	30.3359	0.8146	0.8373	30.0411	0.8208	0.8417	30.2353	0.8210	0.8434

→ For unimodal test functions, the OAVOA can reach near-optimal solutions in most of the case except for the case F5 and F7. It is quite difficult to achieve with restriction in population size and number of iterations. There is a very close completion found between OAVOA and TAVOA for the test functions F2, F3 and F4, where the OAVOA lags TAVOA with very little margin

→ An impressive result is observed from the multimodal test functions. This shows its consistency in reaching optimal solutions irrespective of the dimension size in most of the cases.

5.1.8. *Discussion on results of OAVOA*

According to the qualitative and quantitative analyses covered in the previous part, the OAVOA has demonstrated the supremacy over various contemporary successful optimizers, including EO, HHO, TLBO, GSA, DE, IGWO, BLPSO and HGWOP, as well as an improvement over its predecessors AVOA. As there is a very close fight between the OAVOA and TAVOA, a Friedman's mean rank analysis using average fitness of 25 independent runs for scalable test functions is conducted and the result is presented in Fig. 13. The results show that OAVOA dominated TAVOA

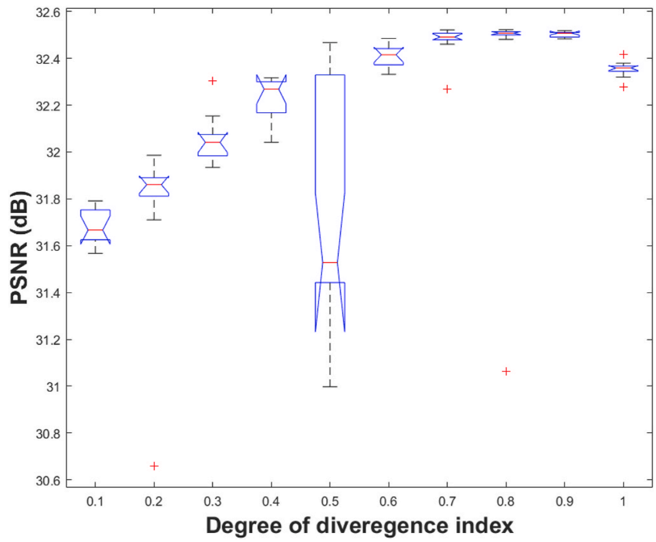

Fig. 19. Effect of degree of divergence on segmentation of Dermoscopic image (ISIC0000149).

and came in first place in the majority of cases. Finally, OAVOA resolve the problems identified in OAVOA by providing required diversity to search agents regulate the exploration and exploitation in the desired manner to reach at the optimum solution.

5.1.9. Analysis of computational complexity

A function that relates the algorithm's execution time to the problem's input size provides information about the computational complexity of an optimization algorithm. Here, Big-O notation is employed as a standard word to describe this situation. Complexity is influenced by factors like the cost of function evaluation (c), the population size (N), the dimension of the problem (dim), and the maximum iteration counts (T). The complexity of initialising the population is become $O(N)$. computation required for updating vulture's position using Eq. (13), Eq. (15), and Eq. (29) is $O(T \times N \times dim)$, computational complexity involved in mutation stage is $O(T \times 0.3N)$, Computation required for generating new solutions using Eq. (25) is $O(T \times N \times dim)$, fitness evaluations of solutions till the end of iterations required a computational complexity of $O(T \times 2N)$. The overall computational complexity of the proposed OAVOA algorithm is $O(T \times 2.3N \times dim) + O(T \times 2N)$.

5.2. Experimental verification of OAVOA-MGCE based multilevel thresholding

The suggested OAVOA-MGCE based multilevel thresholding technique has been evaluated using medical images collected from Harvard Medical school's brain T2-weighted MR image dataset [13] and ISIC 2016 Dermoscopic skin lesion image dataset [77]. Multilevel thresholding is applied to these images to assign a uniform intensity to different objects and the background. Physicians need specific, constrained sections of the test image for clinical analysis, and thresholded images are ideally suited for this purpose. Figs. 14 and 15 shows a sample of five test images and their histogram collected from each dataset. The corresponding thresholded results are depicted in subsequent Figures for the study and analysis. For processing and validating the result, we used MATLAB software R2018 with an Intel Core (TM) i3 Processor running at 1.70 GHz, 8 GB RAM, and a 64-bit operating system. The suggested OAVOA-MGCE based multilevel thresholding approach's primary goal is to choose the optimum thresholding values at various thresholding levels. In this study, for the purposes of reliability assessment and visual perception, the test images are segmented into four different levels of thresholding with $k = 2$, 3, 4, and 5. To show the superiority of proposed algorithm using MGCE as the objective function, we compare it with outputs of its counterparts, the minimum cross-entropy (MCE) and six others broadly used entropy-based techniques, i. e, Kaniadakis entropy, Masi entropy, Tsallis entropy, Renyis entropy, Kapurs entropy and Shannon entropy. The above entropy functions are used as the objective functions. These are optimized by the proposed OAVOA. The reason is its superior performance in reaching the global solution compared to state of art techniques discussed in Section 5.1. The above entropies employing OAVOA for performing multilevel thresholding tasks are now referred as OAVOA-MCE, OAVOA-Kaniadakis, OAVOA-Masi, OAVOA-Tsallis, OAVOA-Renyis, OAVOA-Kapurs and OAVOA-Shannon. Keeping the randomization and stochastic behaviour of optimization algorithm into consideration, each method is run independently 11 times for each test image. The controlling parameter of OAVOA is set as given in Table 3. The maximum iteration count is set to 150. To evaluate the performance of different techniques, we have used the standard performance measures: Peak signal to noise ratio (PSNR) [78], Structural Similarity (SSIM) index [79], Feature Similarity index (FSIM) [80].

5.2.1. Experiments with brain MR images

Diseases related to the brain are very harmful and an early diagnosis can only reduce the fatality rate. The physician uses MR images of the brain in most of the cases to identify any injuries or abnormalities in the brain. This is the reason for the selection of brain MR images for evaluating our proposed method. Table 10 provides a summary of the performance of different entropy-based multilevel thresholding approaches on five test brain MR images utilizing the proposed OAVOA algorithm to optimize the objective functions. The listed values in the tables are average PSNR, average SSIM, and average FSIM over 11 independent runs. The results demonstrated that the OAVOA-MGCE based multilevel thresholding approach enhanced PSNR at various threshold levels. The improvement over MCE based thresholding reveals that the degree of divergence plays a vital role in the thresholding problem.

Due to the non-symmetrical characteristic, the traditional cross entropy, which is also referred as an information divergence measure, sometimes not found an appropriate similarity measure between two different probability distributions. This problem is resolved by the use of minimum generalized cross entropy (MGCE) which uses a degree of convergence for the measurement of the distance between two probability distributions related to original and segmented images. Some of the useful properties that the generalized cross entropy possesses are its flexibility and robustness in similarity measure. The above benefits can be achieved by a single tuning parameter known as the degree of divergence index. To show the effect of degree of divergence index along with the proposed OAVOA algorithm, an ANOVA test is conducted on the test image Slice22 and the obtained PSNR values at $k = 5$ is presented in Fig. 16. It can be seen from the result that a better value of PSNR is obtained when the degree of divergence index is 0.3 with minimal variation.

In our experiment, the degree of divergence index is taken between 0.1 and 0.3. For all entropy-based multilevel thresholding approaches, similarity metrics like SSIM and FSIM are also calculated between the original image and the thresholded image. The structural similarity index (SSIM), which considers factors, including brightness, contrast, and structural similarity, measures how similar the test image and its threshold version. Whereas, feature similarity index (FSIM) is another metric for evaluating the quality of an image by comparing its features to those in the thresholded image. The SSIM and FSIM index values fall between [0, 1]. A higher value of these metrics denotes a higher level of segmented image quality. It is observed from the results that, the proposed OAVOA-MGCE method is able to provide a better segmented result with maximum SSIM and PSNR values. Whenever the number of thresholds increases, the pixel has a greater likelihood of segmenting into the class of objects that are most comparable. This makes the SSIM

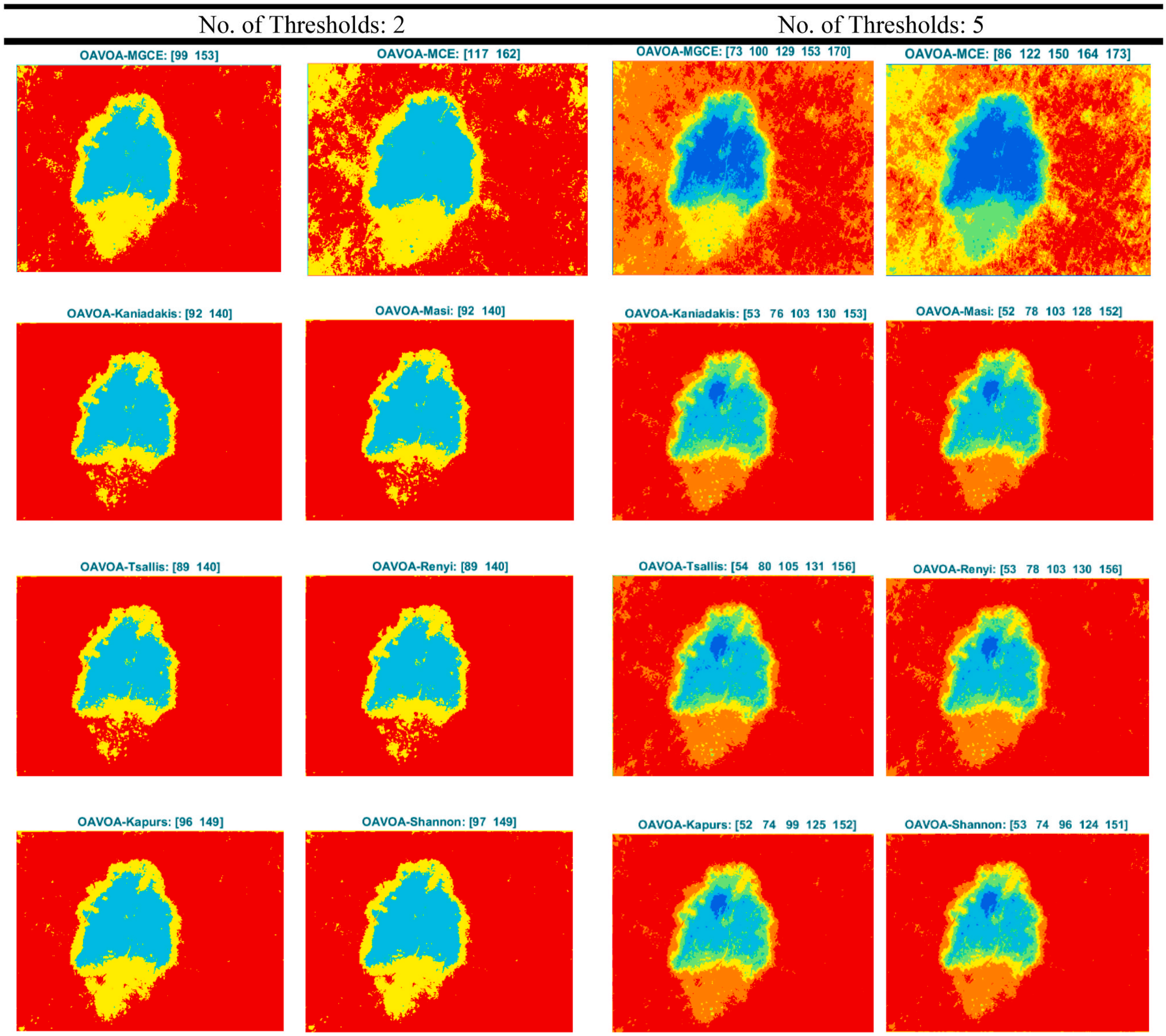

Fig. 20. Thresholded images of Dermoscopic skin lesion images (ISIC 0000020) for $k = 2$ *and* 5

and the FSIM increase with the increase in thresholding level. For visual interpretation of the results, the thresholded images of different entropy-based thresholding for $k = 2$ *and* 5 on slice 082 image are shown in Fig. 17. The optimal threshold values, obtained by maximizing or minimizing the objective function using the OAVOA, are also included on the top of each thresholded output image. To highlight the segmented regions, we have performed Pseudo coloring of the thresholded output. It is observed from the Brain MRI thresholded images that, the soft tissues of the brain as well as other regions are well separated using MGCE and MCE based thresholding compared to other entropy-based methods. To show how consistent and reliable is the proposed thresholding approach, ANOVA test is also conducted. This test is used to deepen our understanding of the different entropy-based thresholding using OAVOA. Here, 55 data samples from each dataset are used for the ANOVA statistical test. The above data samples are collected from five test images and run it independently 11 times. For a better illustration of the ANOVA test results a separate plot for each performance parameter, such as PSNR, SSIM and FSIM plotted in the form of Boxplots for thresholding levels $k = 2$ *to* 5 as shown in Fig. 18. The ANOVA test results for Brain MRI images are completely in favour of the proposed OAVO-MGCE based approach, for its highest median value with comparable less variation from others. In addition to ANOVA test, another statistical analysis of the results using the Wilcoxon signed rank test is also conducted.

The Wilcoxon test p-values are shown in Table 11. These are calculated by comparing the mean PSNR, SSIM, and FSIM values between the MGCE and other entropy-based thresholding methods. There are seven different pairs of algorithms shown: MGCE vs MCE, MGCE vs Kaniadakis, MGCE vs Masi, MGCE vs Tsallis, MGCE vs Renyis, MGCE vs Kapurs and MGCE vs Shannon. When the obtained p-values are less than 0.05, they can be considered statistically significant, because the null hypothesis is rejected. The methods under comparison show substantial differences from one another. To provide a better interpretation of the obtained Wilcoxon test result, the symbols (+) and (−) are assigned to each p-values, which denote the performance of the MGCE based method against the comparative techniques based on superiority and no significant difference, respectively. The table shows that, in most of the cases, each pair of methods typically yields a value less than 0.05 with respect to PSNR, SSIM, and FSIM, demonstrating a considerable difference between the techniques.

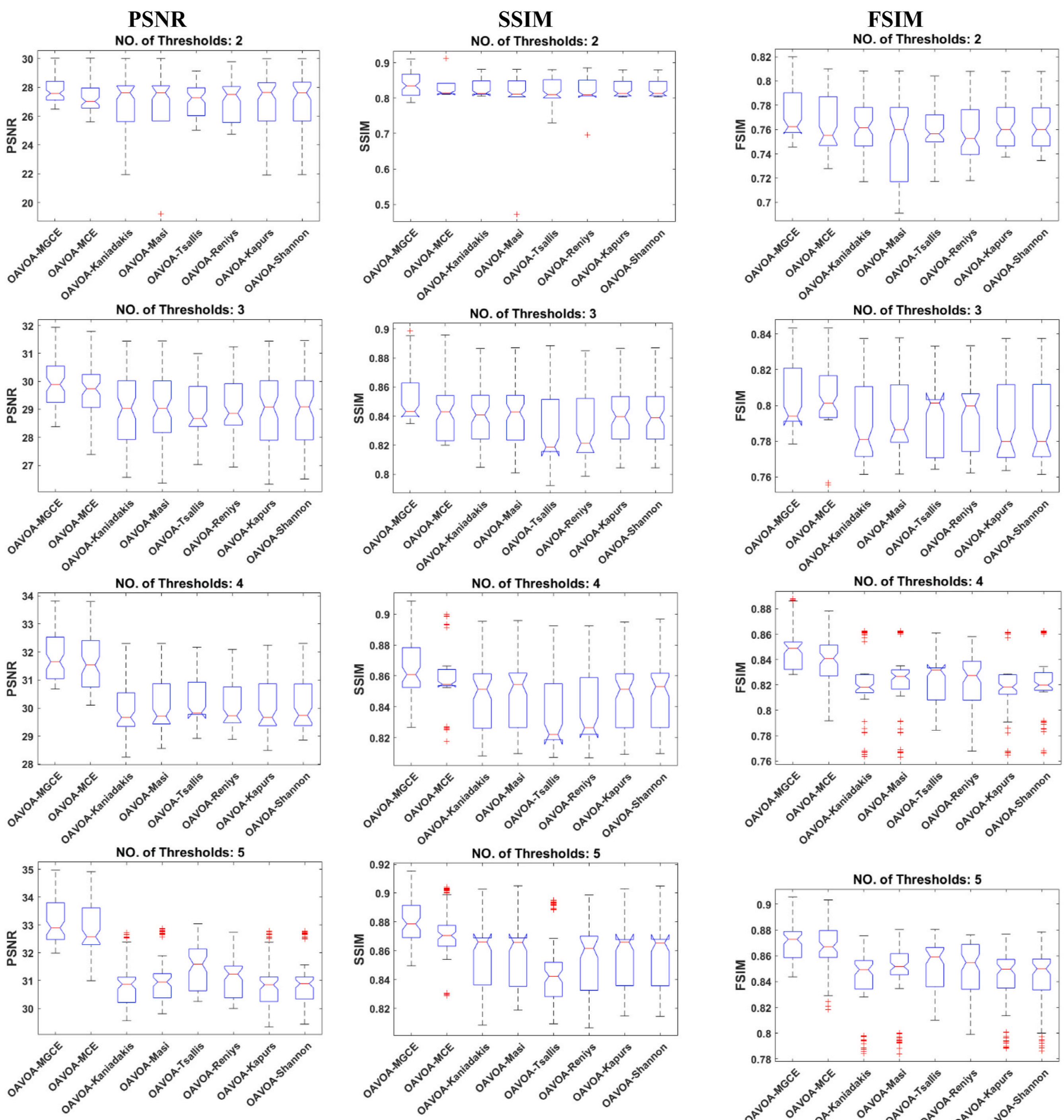

Fig. 21. ANOVA test result of different entropy-based thresholding methods on 50 test Dermoscopic Skin images.

Table 13
Wilcoxon's test for comparison of proposed OAVOA-MGCE based multilevel thresholding with other entropy-based thresholding based on PSNR, SSIM, and FSIM on Dermoscopic skin lesion images.

		PSNR		SSIM		FSIM	
	k	p-value	win	p-value	win	p-value	win
MGCE vs CE	2	1.73E-18	(+)	1.05E-01	(−)	1.01E-12	(+)
	3	5.29E-23	(+)	6.11E-07	(+)	2.48E-01	(−)
	4	1.51E-19	(+)	3.11E-10	(+)	5.29E-23	(+)
	5	1.51E-19	(+)	3.73E-18	(+)	1.08E-03	(+)
MGCE vs Kaniadakis	2	1.59E-07	(+)	1.59E-07	(+)	1.59E-07	(+)
	3	5.29E-23	(+)	1.59E-07	(+)	5.29E-23	(+)
	4	5.29E-23	(+)	1.01E-12	(+)	5.29E-23	(+)
	5	5.29E-23	(+)	1.51E-19	(+)	5.29E-23	(+)
MGCE vs Masi	2	1.59E-07	(+)	5.29E-23	(+)	1.59E-07	(+)
	3	5.29E-23	(+)	1.59E-07	(+)	1.59E-07	(+)
	4	5.29E-23	(+)	6.11E-07	(+)	3.73E-18	(+)
	5	5.29E-23	(+)	6.81E-17	(+)	5.15E-11	(+)
MGCE Vs Tsallis	2	5.29E-23	(+)	5.29E-23	(+)	5.29E-23	(+)
	3	5.15E-11	(+)	5.29E-23	(+)	1.59E-07	(+)
	4	5.29E-23	(+)	5.29E-23	(+)	3.81E-08	(+)
	5	5.29E-23	(+)	5.29E-23	(+)	6.11E-07	(+)
MGCE vs Reniys	2	5.29E-23	(+)	5.29E-23	(+)	5.29E-23	(+)
	3	3.81E-08	(+)	5.29E-23	(+)	1.59E-07	(+)
	4	5.29E-23	(+)	1.51E-19	(+)	1.59E-07	(+)
	5	5.29E-23	(+)	5.29E-23	(+)	1.59E-07	(+)
MGCE vs Kapurs	2	1.76E-04	(+)	1.59E-07	(+)	1.59E-07	(+)
	3	5.29E-23	(+)	1.59E-07	(+)	5.29E-23	(+)
	4	5.29E-23	(+)	1.17E-13	(+)	5.29E-23	(+)
	5	5.29E-23	(+)	1.51E-19	(+)	5.29E-23	(+)
MGCE vs Shannon	2	4.50E-04	(+)	1.59E-07	(+)	1.59E-07	(+)
	3	5.29E-23	(+)	1.59E-07	(+)	5.29E-23	(+)
	4	5.29E-23	(+)	5.15E-11	(+)	5.29E-23	(+)
	5	5.29E-23	(+)	1.51E-19	(+)	4.02E-21	(+)

5.2.2. Experiments with dermoscopic skin lesion images

Another challenging task in medical image analysis is the detection of the lesion in dermoscopic images. Thresholding can be considered one of the convenient methods of detecting the lesion by assigning a certain grey level in the affected region. The grey level distributions of these dermoscopic images are completely different from brain MR images. This is observed from their histogram shown in Fig. 15. Table 12 presents the obtained results of different entropy-based thresholding methods on five different images, selected randomly from the ISIC dataset. An ANOVA test is also conducted to support the claimed range of degree of divergence index and the result is presented in Fig. 19 for $k = 5$. The degree of divergence parameter is taken between 0.7 and 0.9 for achieving the best results. A higher value of PSNR achieved by the proposed OAVOA-MGCE based methodology again proved that its segmentation accuracy is better than others. Although the similarity metric SSIM for MCE-based thresholding is comparable to MGCE-based approach, the MGCE-based method dominates when the number of thresholds rises. A higher FSIM value attained by the proposed method indicates that the consideration of the degree of divergence is helpful for preserving the image features while thresholding. Fig. 20 presented the thresholded images at levels 2 and 5. The lesion in the skin images is also highlighted in the thresholded image in a better way in MGCE and MCE based thresholding. Although MCE based method gives comparable results, failed to differentiate the background completely from the lesion. A close observation of the thresholded results reveals that the proposed OAVOA-MGCE method produces better-thresholded results. It separates different regions in the scenes including backgrounds. The superiority of the proposed method is also reflected in the ANOVA test (in Fig. 21). At low-level thresholding, most of the entropy-based methods behaves likewise. However, a significant difference between the performances is observed, when the thresholding levels are increased. The Wilcoxon's test results are shown in Table 13 (for dermoscopic images). This provides a clear view that the suggested method is statistically different from others, with respect to various performance metrics.

At the end of the discussion, the thresholded images, obtained by the proposed OAVOA-MGCE multilevel thresholding approach to all test images, are presented in Fig. 22. The resultant output reveals that the segmented results are quite impressive and well suited for medical image analysis.

6. Conclusions

This paper proposed an efficient OAVOA-MGCE methodology by minimizing the MGCE fitness functions. The proposed opposition African vulture optimization algorithm (OAVOA) is used to compute the optimal thresholds for the segmentation of medical images. The fitness functions include the degree of divergence between the input and segmented output images, as opposed to the previous studies. As a result, improved accuracy is ascertained by properly optimizing the fitness functions. To evaluate the proposed OAVOA-MGCE multilevel thresholding approach, the segmentation was performed at four different levels on two different types of the medical images. A set of metrics for assessing the efficiency of segmentation at each level is obtained to interpret the segmentation accuracy. Based on the results, it is concluded that the OAVOA-MGCE shows substantial results, because the technique suggested mainly exhibits the best values compared to other entropy-based thresholding schemes. In addition to the performance metrics, ANOVA and Wilcoxon tests were also conducted to show the consistency and superiority of the proposed method over others. Although the proposed OAVOA-MGCE method appears to work well in various test images, the primary drawbacks associated with the method is that it is not automatic. It may be noted that the number of thresholds and degree of divergence must be provided at the beginning manually. However, it is anticipated to be used by the machine learning or reinforcement learning, to automatically find the appropriate number of thresholds as well as the degree of divergence for a particular image, in

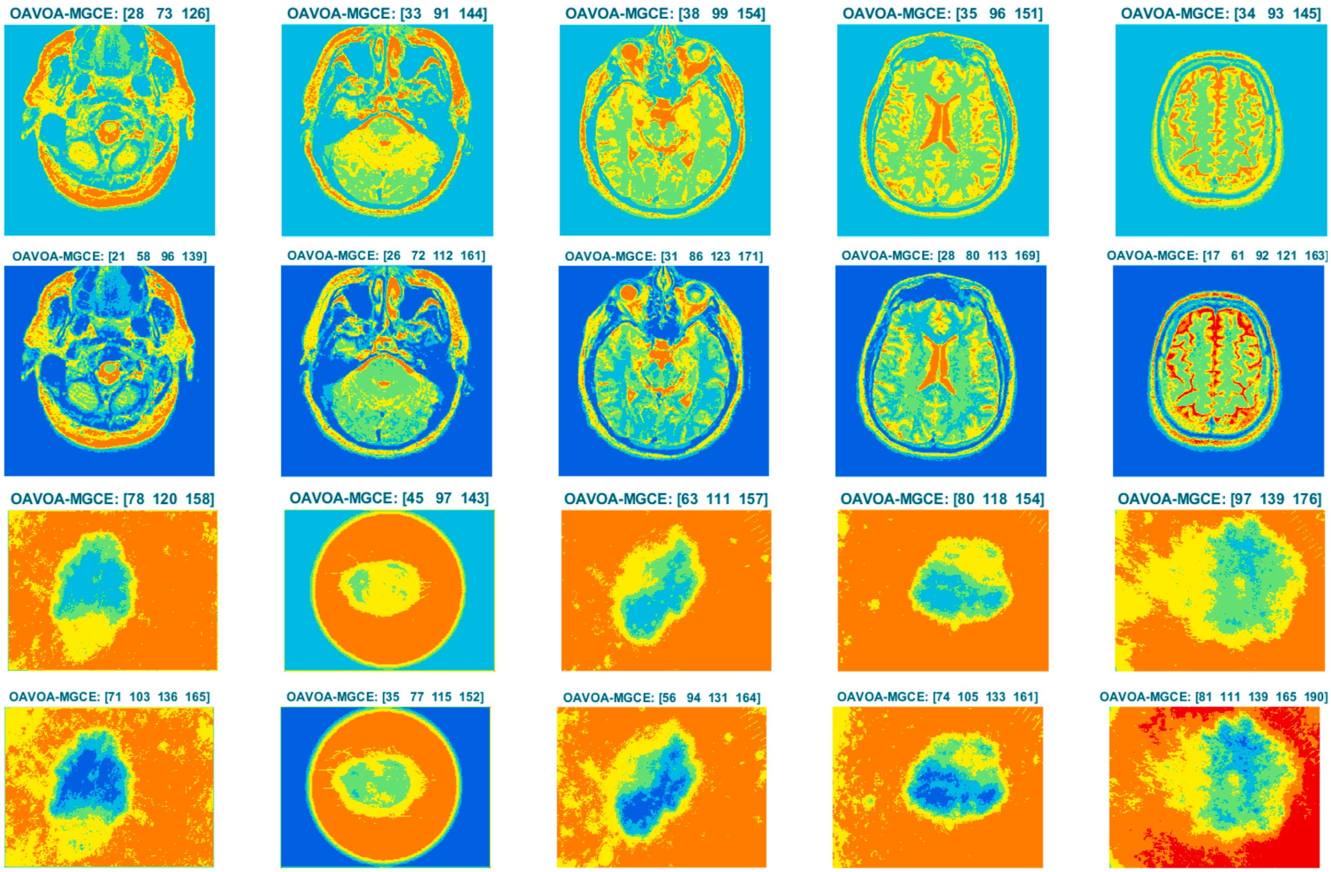

Fig. 22. Thresholded output of OAVOA-MGCE based thresholding for $k = 3$ *and* 4

future applications. In addition, the proposed approach can be extended to noisy images with a selection of appropriate objective function derived from 2D or 3D histogram. The segmented method may be applied to remote sensing images for improving the result of change detection.

Declaration of competing interest

The authors declare that they have no known competing financial interests or personal relationships that could have appeared to influence the work reported in this paper.

References

[1] R. Huang, A. Nedanoski, D.F. Fletcher, N. Singh, J. Schmid, P.M. Young, N. Stow, L. Bi, D. Traini, E. Wong, C.L. Phillips, R.R. Grunstein, J. Kim, An automated segmentation framework for nasal computational fluid dynamics analysis in computed tomography, Comput. Biol. Med. 115 (2019), 103505, https://doi.org/10.1016/j.compbiomed.2019.103505.

[2] A. Clèrigues, S. Valverde, J. Bernal, J. Freixenet, A. Oliver, X. Lladó, Acute ischemic stroke lesion core segmentation in CT perfusion images using fully convolutional neural networks, Comput. Biol. Med. 115 (2019), 103487, https://doi.org/10.1016/j.compbiomed.2019.103487.

[3] B. He, W. Hu, K. Zhang, S. Yuan, X. Han, C. Su, J. Zhao, G. Wang, G. Wang, L. Zhang, Image segmentation algorithm of lung cancer based on neural network model, Expet Syst. 39 (2022), e12822, https://doi.org/10.1111/exsy.12822.

[4] S. Tang, F. Yu, Construction and verification of retinal vessel segmentation algorithm for color fundus image under BP neural network model, J. Supercomput. 77 (2021) 3870–3884, https://doi.org/10.1007/s11227-020-03422-8.

[5] Y. Dai, J. Wu, Y. Fan, J. Wang, J. Niu, F. Gu, S. Shen, MSEva: a musculoskeletal rehabilitation evaluation system based on emg signals, ACM Trans. Sens. Netw. (2022), https://doi.org/10.1145/3522739.

[6] Z. Wu, G. Li, S. Shen, X. Lian, E. Chen, G. Xu, Constructing dummy query sequences to protect location privacy and query privacy in location-based services, World Wide Web 24 (2021) 25–49, https://doi.org/10.1007/s11280-020-00830-x.

[7] J. Zhou, X. Zhang, Z. Jiang, Recognition of imbalanced epileptic EEG signals by a graph-based extreme learning machine, Wireless Commun. Mobile Comput. (2021), 5871684, https://doi.org/10.1155/2021/5871684, 2021.

[8] W. Yan, G. Li, Z. Wu, S. Wang, P.S. Yu, Extracting diverse-shapelets for early classification on time series, World Wide Web 23 (2020) 3055–3081, https://doi.org/10.1007/s11280-020-00820-z.

[9] Z. Wu, S. Xuan, J. Xie, C. Lin, C. Lu, How to ensure the confidentiality of electronic medical records on the cloud: a technical perspective, Comput. Biol. Med. 147 (2022), 105726, https://doi.org/10.1016/j.compbiomed.2022.105726.

[10] K. Hu, L. Zhao, S. Feng, S. Zhang, Q. Zhou, X. Gao, Y. Guo, Colorectal polyp region extraction using saliency detection network with neutrosophic enhancement, Comput. Biol. Med. 147 (2022), 105760, https://doi.org/10.1016/j.compbiomed.2022.105760.

[11] A. Aly A. Farag, Mohamed N. Ahmed, Ayman El-Baz, H. Hassan, Advanced segmentation techniques, in: D.L. HIn Wilson, S. Laxminarayan (Eds.), Suri JS Handb. Biomed. Image Anal. 26 A. Elnakib Al., Kluwer Acad. Publ., New York, 2005, pp. 479–534, https://doi.org/10.1007/978-3-642-88304-0_5. I Segmentationmodels.

[12] M. Prastawa, E. Bullitt, G. Gerig, Simulation of brain tumors in MR images for evaluation of segmentation efficacy, Med. Image Anal. 13 (2009) 297–311, https://doi.org/10.1016/j.media.2008.11.002.

[13] The Whole Brain Atlas, 2015. http://www.med.harvard.edu/AANLIB/.

[14] R. Sumithra, M. Suhil, D.S. Guru, Segmentation and classification of skin lesions for disease diagnosis, Procedia Comput. Sci. 45 (2015) 76–85, https://doi.org/10.1016/j.procs.2015.03.090.

[15] P. Upadhyay, J.K. Chhabra, Kapur's entropy based optimal multilevel image segmentation using Crow Search Algorithm, Appl. Soft Comput. 97 (2020), 105522, https://doi.org/10.1016/j.asoc.2019.105522.

[16] W. Liu, Y. Huang, Z. Ye, W. Cai, S. Yang, X. Cheng, I. Frank, Renyi's entropy based multilevel thresholding using a novel meta-heuristics algorithm, Appl. Sci. 10 (2020) 1–18, https://doi.org/10.3390/app10093225.

[17] S. Agrawal, R. Panda, S. Bhuyan, B.K. Panigrahi, Tsallis entropy based optimal multilevel thresholding using cuckoo search algorithm, Swarm Evol. Comput. 11 (2013) 16–30, https://doi.org/10.1016/j.swevo.2013.02.001.

[18] K.L.N. Sri Madhava Raja, V. Rajinikanth, Otsu based optimal multilevel image thresholding using firefly algorithm, in: Model. Simul. Eng., Hindawi Publ. Corp., 2014, https://doi.org/10.1155/2014/794574, 2014.

[19] A.K.M. Khairuzzaman, S. Chaudhury, Masi entropy based multilevel thresholding for image segmentation, Multimed. Tool. Appl. 78 (2019) 33573–33591, https://doi.org/10.1007/s11042-019-08117-8.

[20] H. Singh Gill, B. Singh Khehra, A. Singh, L. Kaur, Teaching-learning-based optimization algorithm to minimize cross entropy for Selecting multilevel threshold values, Egypt, Informatics J 20 (2019) 11–25, https://doi.org/10.1016/j.eij.2018.03.006.
[21] A. Carolina Sparavigna, Shannon, tsallis and Kaniadakis entropies in Bi-level image thresholding, Intermt. J. Sci. 1 (2015) 35–43, https://doi.org/10.18483/ijsci.626.
[22] J.N. Kapur, H.K. Kesavan, Entropy optimization principles and their applications, in: V.P. Singh, M. Fiorentino (Eds.), Entropy Energy Dissipation Water Resour., Springer Netherlands, Dordrecht, 1992, pp. 3–20, https://doi.org/10.1007/978-94-011-2430-0_1.
[23] A.K.M. Khairuzzaman, S. Chaudhury, Brain MR image multilevel thresholding by using particle swarm optimization, Otsu method and anisotropic diffusion, Int. J. Appl. Metaheuristic Comput. (IJAMC) 10 (2019) 91–106, https://doi.org/10.4018/IJAMC.2019070105.
[24] S. Sarkar, S. Das, S.S. Chaudhuri, A multilevel color image thresholding scheme based on minimum cross entropy and differential evolution, Pattern Recogn. Lett. 54 (2015) 27–35, https://doi.org/10.1016/j.patrec.2014.11.009.
[25] H.S. Gill, B.S. Khehra, Apple image segmentation using teacher learner based optimization based minimum cross entropy thresholding, Multimed. Tool. Appl. 81 (2022) 11005–11026, https://doi.org/10.1007/s11042-022-12093-x.
[26] M.A. El Aziz, A.A. Ewees, A.E. Hassanien, M. Mudhsh, S. Xiong, Multi-objective whale optimization algorithm for multilevel thresholding segmentation, Stud. Comput. Intell. 730 (2018) 23–39, https://doi.org/10.1007/978-3-319-63754-9_2.
[27] A.A. Heidari, S. Mirjalili, H. Faris, I. Aljarah, M. Mafarja, H. Chen, Harris hawks optimization: algorithm and applications, Futur, Gener. Comput. Syst. 97 (2019) 849–872, https://doi.org/10.1016/j.future.2019.02.028.
[28] M. Abdel-Basset, V. Chang, R. Mohamed, A Novel Equilibrium Optimization Algorithm for Multi-Thresholding Image Segmentation Problems, Springer London, 2021, https://doi.org/10.1007/s00521-020-04820-y.
[29] B. Abdollahzadeh, F.S. Gharehchopogh, S. Mirjalili, African vultures optimization algorithm: a new nature-inspired metaheuristic algorithm for global optimization problems, Comput. Ind. Eng. 158 (2021), 107408, https://doi.org/10.1016/j.cie.2021.107408.
[30] D. Gürses, P. Mehta, S.M. Sait, A.R. Yildiz, African vultures optimization algorithm for optimization of shell and tube heat exchangers 64 (2022) 1234–1241, https://doi.org/doi:10.1515/mt-2022-0050.
[31] M. Manickam, R. Siva, S. Prabakeran, K. Geetha, V. Indumathi, T. Sethukarasi, Pulmonary disease diagnosis using African vulture optimized weighted support vector machine approach, Int. J. Imag. Syst. Technol. 32 (2022) 843–856, https://doi.org/10.1002/ima.22669.
[32] J. Fan, Y. Li, T. Wang, An Improved African Vultures Optimization Algorithm Based on Tent Chaotic Mapping and Time-Varying Mechanism, 2021, https://doi.org/10.1371/journal.pone.0260725.
[33] H.R. Tizhoosh, Opposition-based learning: a new scheme for machine intelligence, Int. Conf. Comput. Intell. Model. Control Autom. Int. Conf. Intell. Agents, Web Technol. Internet Commer. 1 (2005) 695–701.
[34] F. Huo, X. Sun, W. Ren, Multilevel image threshold segmentation using an improved Bloch quantum artificial bee colony algorithm, Multimed. Tool. Appl. 79 (2020) 2447–2471, https://doi.org/10.1007/s11042-019-08231-7.
[35] A.H. Gandomi, A.H. Alavi, Krill herd, A new bio-inspired optimization algorithm, Commun. Nonlinear Sci. Numer. Simulat. 17 (2012) 4831–4845, https://doi.org/10.1016/j.cnsns.2012.05.010.
[36] E. Rashedi, H. Nezamabadi-pour, S. Saryazdi, GSA: a gravitational search algorithm, Inf. Sci. 179 (2009) 2232–2248, https://doi.org/10.1016/j.ins.2009.03.004.
[37] G.-G. Wang, S. Deb, L. dos S. Coelho, Elephant herding optimization, in: 2015 3rd Int. Symp. Comput. Bus. Intell., 2015, pp. 1–5, https://doi.org/10.1109/ISCBI.2015.8.
[38] G.G. Wang, S. Deb, L. Dos Santos Coelho, Earthworm optimisation algorithm: a bio-inspired metaheuristic algorithm for global optimisation problems, Int. J. Bio-Inspired Comput. 12 (2018) 1–22, https://doi.org/10.1504/ijbic.2018.093328.
[39] G.G. Wang, S. Deb, Z. Cui, Monarch butterfly optimization, neural, Comput. Appl 31 (2019) 1995–2014, https://doi.org/10.1007/s00521-015-1923-y.
[40] S. Li, H. Chen, M. Wang, A.A. Heidari, S. Mirjalili, Slime mould algorithm: a new method for stochastic optimization, Future Generat. Comput. Syst. 111 (2020) 300–323, https://doi.org/10.1016/j.future.2020.03.055.
[41] G.G. Wang, Moth search algorithm: a bio-inspired metaheuristic algorithm for global optimization problems, Memetic Comput 10 (2018) 151–164, https://doi.org/10.1007/s12293-016-0212-3.
[42] Y. Yang, H. Chen, A.A. Heidari, A.H. Gandomi, Hunger games search: visions, conception, implementation, deep analysis, perspectives, and towards performance shifts, Expert Syst. Appl. 177 (2021), 114864, https://doi.org/10.1016/j.eswa.2021.114864.
[43] I. Ahmadianfar, A.A. Heidari, A.H. Gandomi, X. Chu, H. Chen, RUN beyond the metaphor: an efficient optimization algorithm based on Runge Kutta method, Expert Syst. Appl. 181 (2021), 115079, https://doi.org/10.1016/j.eswa.2021.115079.
[44] J. Tu, H. Chen, M. Wang, A.H. Gandomi, The colony predation algorithm, J. Bionic Eng. 18 (2021) 674–710, https://doi.org/10.1007/s42235-021-0050-y.
[45] I. Ahmadianfar, A.A. Heidari, S. Noshadian, H. Chen, A.H. Gandomi, INFO: an efficient optimization algorithm based on weighted mean of vectors, Expert Syst. Appl. 195 (2022), 116516, https://doi.org/10.1016/j.eswa.2022.116516.
[46] Hsma_Woa, A hybrid novel Slime mould algorithm with whale optimization algorithm for tackling the image segmentation problem of chest X-ray images, Appl. Soft Comput. J. (2020) 293.
[47] M.H. Nadimi-Shahraki, S. Taghian, S. Mirjalili, An improved grey wolf optimizer for solving engineering problems, Expert Syst. Appl. 166 (2021), 113917, https://doi.org/10.1016/j.eswa.2020.113917.
[48] X. Chen, H. Tianfield, C. Mei, W. Du, G. Liu, Biogeography-based learning particle swarm optimization, Soft Comput. 21 (2017) 7519–7541, https://doi.org/10.1007/s00500-016-2307-7.
[49] G. Dhiman, ESA: a hybrid bio-inspired metaheuristic optimization approach for engineering problems, Eng. Comput. 37 (2021) 323–353, https://doi.org/10.1007/s00366-019-00826-w.
[50] J. Luo, H. Chen, Q. zhang, Y. Xu, H. Huang, X. Zhao, An improved grasshopper optimization algorithm with application to financial stress prediction, Appl. Math. Model. 64 (2018) 654–668, https://doi.org/10.1016/j.apm.2018.07.044.
[51] Y. Xu, H. Chen, A.A. Heidari, J. Luo, Q. Zhang, X. Zhao, C. Li, An efficient chaotic mutative moth-flame-inspired optimizer for global optimization tasks, Expert Syst. Appl. 129 (2019) 135–155, https://doi.org/10.1016/j.eswa.2019.03.043.
[52] G. Li, G.-G. Wang, J. Dong, W.-C. Yeh, K. Li, DLEA: a dynamic learning evolution algorithm for many-objective optimization, Inf. Sci. 574 (2021) 567–589, https://doi.org/10.1016/j.ins.2021.05.064.
[53] W. Li, G.-G. Wang, A.H. Gandomi, A survey of learning-based intelligent optimization algorithms, Arch. Comput. Methods Eng. 28 (2021) 3781–3799, https://doi.org/10.1007/s11831-021-09562-1.
[54] W. Li, G.-G. Wang, A.H. Alavi, Learning-based elephant herding optimization algorithm for solving numerical optimization problems, Knowl. Base Syst. 195 (2020), 105675, https://doi.org/10.1016/j.knosys.2020.105675.
[55] X. Zhang, Q. Lin, W. Mao, S. Liu, Z. Dou, G. Liu, Hybrid particle swarm and grey wolf optimizer and its application to clustering optimization, Appl. Soft Comput. 101 (2021), 107061, https://doi.org/10.1016/j.asoc.2020.107061.
[56] H. Su, D. Zhao, F. Yu, A.A. Heidari, Y. Zhang, H. Chen, C. Li, J. Pan, S. Quan, Horizontal and vertical search artificial bee colony for image segmentation of COVID-19 X-ray images, Comput. Biol. Med. 142 (2022), 105181, https://doi.org/10.1016/j.compbiomed.2021.105181.
[57] M. Maitra, A. Chatterjee, A novel technique for multilevel optimal magnetic resonance brain image thresholding using bacterial foraging, Meas. J. Int. Meas. Confed. 41 (2008) 1124–1134, https://doi.org/10.1016/j.measurement.2008.03.002.
[58] P.D. Sathya, R. Kayalvizhi, Optimal segmentation of brain MRI based on adaptive bacterial foraging algorithm, Neurocomputing 74 (2011) 2299–2313, https://doi.org/10.1016/j.neucom.2011.03.010.
[59] K. Selva Bhuvaneswari, P. Geetha, Segmentation and classification of brain images using firefly and hybrid kernel-based support vector machine, J. Exp. Theor. Artif. Intell. 29 (2017) 663–678, https://doi.org/10.1080/0952813X.2016.1212106.
[60] P. Priyedarsni, B. Nandhini, A.R. Catherine, K. Sahana, K. Sundaravadivu, Soft-computing assisted tool to extract tumor section from brain MR images, IEEE Int. Conf. Power, Control. Signals Instrum. Eng. ICPCSI (2017) 2776–2780, https://doi.org/10.1109/ICPCSI.2017.8392224, 2018.
[61] M. Ganesh, M. Naresh, C. Arvind, MRI brain image segmentation using enhanced adaptive fuzzy K-means algorithm, Intell. Autom. Soft Comput. 23 (2017) 325–330, https://doi.org/10.1080/10798587.2016.1231472.
[62] S. Sarkar, S. Das, Multilevel image thresholding based on 2D histogram and maximum tsallis entropy - a differential evolution approach, IEEE Trans. Image Process. 22 (2013) 4788–4797, https://doi.org/10.1109/TIP.2013.2277832.
[63] A. Knowles, A database, Datamation. 43 (1997) 62–68.
[64] Y. Feng, H. Zhao, X. Li, X. Zhang, H. Li, A multi-scale 3D Otsu thresholding algorithm for medical image segmentation, Digit. Signal Process. A Rev. J. 60 (2017) 186–199, https://doi.org/10.1016/j.dsp.2016.08.003.
[65] M. Attia, M. Hossny, H. Zhou, S. Nahavandi, H. Asadi, A. Yazdabadi, Digital hair segmentation using hybrid convolutional and recurrent neural networks architecture, Comput. Methods Progr. Biomed. 177 (2019) 17–30, https://doi.org/10.1016/j.cmpb.2019.05.010.
[66] A.R. Hawas, Y. Guo, C. Du, K. Polat, A.S. Ashour, OCE-NGC: a neutrosophic graph cut algorithm using optimized clustering estimation algorithm for dermoscopic skin lesion segmentation, Appl. Soft Comput. J. 86 (2020), 105931, https://doi.org/10.1016/j.asoc.2019.105931.
[67] C. Barata, M. Ruela, M. Francisco, T. Mendonca, J.S. Marques, Two systems for the detection of melanomas in dermoscopy images using texture and color features, IEEE Syst. J. 8 (2014) 965–979, https://doi.org/10.1109/JSYST.2013.2271540.
[68] S. Chatterjee, D. Dey, S. Munshi, S. Gorai, Extraction of features from cross correlation in space and frequency domains for classification of skin lesions, Biomed. Signal Process Control 53 (2019), 101581, https://doi.org/10.1016/j.bspc.2019.101581.
[69] M.A. Khan, T. Akram, M. Sharif, A. Shahzad, K. Aurangzeb, M. Alhussein, S. I. Haider, A. Altamrah, An implementation of normal distribution based segmentation and entropy controlled features selection for skin lesion detection and classification, BMC Cancer 18 (2018) 1–20, https://doi.org/10.1186/s12885-018-4465-8.
[70] X. Gao, L. Jia, S. Kar, A new definition of cross-entropy for uncertain variables, Soft Comput. 22 (2018) 5617–5623, https://doi.org/10.1007/s00500-017-2534-6.
[71] S. Mahdavi, S. Rahnamayan, K. Deb, Opposition based learning: a literature review, Swarm Evol. Comput. 39 (2018) 1–23, https://doi.org/10.1016/j.swevo.2017.09.010.
[72] D.H. Wolpert, W.G. Macready, No free lunch theorems for optimization, IEEE Trans. Evol. Comput. 1 (1997) 67–82, https://doi.org/10.1109/4235.585893.
[73] S. Kullback, Information Theory and Statistics, 1959, https://doi.org/10.1137/1002033.
[74] X.U.E. Jinghao, Z. Yujin, L.I.N. Xinggang, Threshold Selection Using Cross-Entropy and Fuzzy Divergence, vol. 3561 (n.d.) 152–162.

[75] C.H. Li, C.K. Lee, Minimum cross entropy thresholding, Pattern Recogn. 26 (1993) 617–625, https://doi.org/10.1016/0031-3203(93)90115-D.
[76] M.K. Naik, R. Panda, A. Abraham, Normalized square difference based multilevel thresholding technique for multispectral images using leader slime mould algorithm, J. King Saud Univ. - Comput. Inf. Sci. (2020), https://doi.org/10.1016/j.jksuci.2020.10.030.
[77] D. Gutman, N.C.F. Codella, E. Celebi, B. Helba, M. Marchetti, N. Mishra, A. Halpern, Skin Lesion Analysis toward Melanoma Detection: A Challenge at the International Symposium on Biomedical Imaging (ISBI) 2016, Hosted by the International Skin Imaging Collaboration (ISIC), 2016, pp. 3–7. http://arxiv.org/abs/1605.01397.
[78] H. Jia, J. Ma, W. Song, Multilevel thresholding segmentation for color image using modified moth-flame optimization, IEEE Access 7 (2019) 44097–44134, https://doi.org/10.1109/ACCESS.2019.2908718.
[79] E.P.S. Zhou Wang, Alan conrad bovik, hamid rahim sheikh, image quality assessment: from error visibility to structural similarity, Can. J. Civ. Eng. 44 (2017) 253–263, https://doi.org/10.1139/cjce-2016-0381.
[80] L.Z. Lin Zhang, FSIM: a feature similarity index for image quality assessment, IEEE Trans. Image Process. 20 (2011) 2378, https://doi.org/10.1109/TIP.2011.2109730.